The Electrophoretic Mobility of Bare and Soft Spherical Colloids: a Molecular Dynamics Study

Von der Fakultät Mathematik und Physik der Universität Stuttgart
zur Erlangung der Würde eines Doktors der
Naturwissenschaften (Dr. rer. nat.) genehmigte Abhandlung

Vorgelegt von
Shervin Raafatnia
aus Gorgan, Iran

Hauptberichter: Prof. Dr. Christian Holm
Mitberichter: Prof. Dr. Hans-Rainer Trebin

Tag der mündlichen Prüfung: 17.12.2014

Institut für Computerphysik der Universität Stuttgart

2014

Contents

List of Figures

List of Tables

List of Publications

1. I. Semenov, S. Raafatnia, M. Sega, V. Lobaskin, C. Holm, and F. Kremer, "‘Electrophoretic mobility and charge inversion of a colloidal particle studied by single-colloid electrophoresis and molecular dynamics simulations"’, *Physical Review E* **87**, 022302 (2013).
2. S. Raafatnia, O. A. Hickey, M. Sega, and C. Holm, "‘Computing the Electrophoretic Mobility of Large Spherical Colloids by Combining Explicit Ion Simulations with the Standard Electrokinetic Model"’, *Langmuir* **30 (7)**, 1758 – 1767 (2014).
3. S. Raafatnia, O. A. Hickey, and C. Holm, "‘Mobility reversal of polyelectrolyte-grafted colloids in monovalent salt solution."’, *Physical Review Letters* **113**, 238301 (2014).
4. S. Raafatnia, O. A. Hickey, and C. Holm, "‘Electrophoresis of a Spherical Polyelectrolyte-Grafted Colloid in Monovalent Salt Solutions: Comparison of Molecular Dynamics Simulations with Theory and Numerical Calculations"’, *Macromolecules*, **DOI:**10.1021/ma502238z, (2015), in print.

To My Beloved Parents

Acknowledgements

A new era of my life began upon coming to Stuttgart about five years ago, where I learned a lot about Physics, as well as life in general. Many helped me on my way during this period to make it a nice and memorable time in spite of the difficulties of being so far away from home.

Above all, I would like to express my most heartfelt thanks to Dr. Florian Dommert, my significant other and former colleague, who always inspired me with his brilliant personality, encouraging me to continue and follow my ideas, even during the personal and professional hard times. Over the years of my work here, I also benefited from having many good colleagues, who not only helped me professionally, but some of them even became good friends. In particular, I would like to thank Dr. Owen Hickey, who supervised most of my work, for his invaluable help and support, and for expanding my understanding of physics. I am also indebted to Dr. Marcello Sega for his kindness and for providing me with a great start in the early stages of my work. I appreciate many fruitful discussions with Prof. Dr. Christain Holm, my supervisor, Dr. Vladimir Lobaskin, with whom I collaborated in the early part of my work, JP. Dr. Axel Arnold, one of the core developers of the software package ESPResSo, Dr. Joost de Graaf, who kindly took the time and effort to review my publications, and Georg Rempfer, a good friend and colleague who impressed me with his deep understanding of physics. I am grateful to the institute's secretary, dear Ms. Henriette Patzelt, for her kindness and great support with all the administrative work, and to Mr. Frank Huber, the institute's system administrator, for his readiness to help whenever needed. I also thank my colleagues Dr. Oliver Hönig and Dr. Rudolf Weeber for their valuable friendship.

I would also like to use the opportunity here to express my deep gratitude towards Prof. Dr. Farshid Mohammad-Rafiee, my former supervisor, from whom I learned a lot and without whose support I would not have been able to continue my studies abroad.

Besides the professional aspects during my studies here, I had the privilege of being in the extremely kind and warmhearted family of Dr. Florian Dommert, who always gave me the feeling of being home. I am very thankful for everything they did for me.

At the end, I would like to thank all my other colleagues, my dear friends and family, who supported me during and beyond this period of my life. Last but not least, I especially thank my beloved parents whose kindness is beyond what words can say, who always encouraged me with their love and support, providing me with more than I needed, and who patiently bore the hardships of separation so that I can pursue my dreams. I am eternally thankful for everything they did and will do for me.

1 Zusammenfassung

Die vorliegende Doktorarbeit beschäftigt sich mit Computersimulationen der Elektrophorese kolloidaler Teilchen in Salzlösungen. Kolloide, Teilchen mit Durchmessern zwischen Nano- und Mikrometer, sind ein wichtiger Bestandteil der sogenannten "Weichen Materie". Diese befinden sich in vielen unterschiedlichen Systemen, wie z.B. Blut, Milch und Farbe, und haben verschiedene Anwendungen in der Biologie und Industrie. Da diese meist in einer polaren Flüssigkeit gelöst sind, ist ihre Oberfläche oft geladen, was deren Verhalten stark beeinflusst. Hier wird die Elektrophorese kolloidaler Teilchen mit Hilfe vergröbter Molekulardynamik (MD) Simulationen untersucht. Zwei unterschiedliche Typen von Kolloiden werden betrachtet; nackte Kolliode (bare colloids) und Polyelektrolyt-beschichtete (polyelectrolyte-grafted) Kolloide, die auch als weiche Kolloide (soft colloids) bezeichnet werden. Ein neues Modell wird entwickelt, das Simulationen von großen nackten Kolloiden in Gegenwart von expliziten Ionen ermöglicht. Dabei helfen Vergleiche mit unabhängigen Experimenten, die Simulationen mancher Phänomene besser zu verstehen. Außerdem, wird ein neues, bisher unbekanntes, elekrophoretisches Verhalten von Polyelektrolyt-beschichteten Kolloiden, durch Computersimulationen entdeckt, die eine vollständige Beschreibung der hydrodynamischen Wechselwirkungen einschließen. Dabei werden die Simulationsergebnisse mit bestehenden Theorien verglichen, deren Gültigkeit und Grenzen dadurch überprüft werden.

Die für den Simulationen nötigen Konzepte und Algorithmen werden zunächst kurz vorgestellt, worauf eine kurze Zusammenfassung der wichtigsten Ergebnisse folgt.

1.1 Die Prinzipien der Molekulardynamik

Molekulardynamik (MD) Simulationen sind Algorithmen, mit deren Hilfe die Bahnen von Teilchen nach den Newton'schen Bewegungsgesetzen berechnet werden können, indem der Ort und die Geschwindigkeit aller Teilchen in diskreten Zeitschritten berechnet wird. Dafür müssen die Kräfte, die auf jedes Teilchen wirken, von Wechselwirkungspotentialen abgeleitet und durch Integration der Ort und die Geschwindigkeit des Teilchens kalkuliert werden. Dabei ist das Kraftberechnungsverfahren der zeitaufwendigste Teil der Simulation und wird in jedem Zeitschritt für jedes einzelne Teilchen im System durchgeführt. Die berechneten Positionen und Geschwindigkeiten jedes Zeitschritts werden als Anfangswerte in dem nächsten verwendet. So wird im Laufe der Zeit die Dynamik eines Systems simuliert. Schließlich erlaubt uns die statistische Mechanik, aus diesen mikroskopischen Informationen makroskopische Mittelwerte zu gewinnen.

Erstens benötigt eine MD Simulation eine gute, möglichst einfache, mathematische Beschreibung der Wechselwirkungen im System, und zweitens ein effizientes Kraftberechnungsverfahren, womit große Systeme mit vielen Teilchen behandelt werden können. Es gibt unterschiedliche Methoden dafür, verschiedene Kräfte schnell auszurechnen. Ein Beispiel für kurzreichweitige Kräfte ist die Verwendung eines “cutoffs”, der über eine Verlet- oder eine Zellenliste realisiert werden kann. Langreichweitige Kräfte sind schwieriger zu behandeln, da sich durch die Anwendung der periodische Randbedingungen unendliche Summen ergeben. Dafür sind spezielle Verfahren für verschiedene Fälle vorhanden. In dieser Arbeit gibt es als Beispiel die elektrostatischen Wechselwirkungen, die durch sogenannte Ewald-Methoden oder die darauf basierenden und schnelleren Particle-Mesh-Methoden berechnet werden.

Der Integrationsschritt selbst ist nicht zeitaufwendig, aber jedoch sehr wichtig, da viele Haupteigenschaften des Systems, wie z.B. die Zeitreversibilität oder die Energieerhaltung, dadurch bestimmt sind. Die häufigsten Verfahren sind der Velocity-Verlet und der Leap-Frog Algorithmus.

1.2 Grobkörnige Modelle

Eine Simulation eines Systems mit vielen Teilchen, die alle Freiheitsgrade in Betracht zieht, ist für die meisten interessanten Systeme, wenn überhaupt möglich, sehr zeitaufwendig. In vielen Fällen sind nicht alle Details relevant für eine Studie, so dass manche Effekte durch ein effektives Potential beschrieben werden können. So kann man die Anzahl der Freiheitsgrade stark reduzieren und damit die Simulation beschleunigen oder erst ermöglichen. Zum Beispiel, wenn die chemische Zusammensetzung oder die genaue Struktur eines Teilchens keine wichtige Rolle spielt, kann das Teilchen durch das Lennard-Jones Potential (LJ) dargestellt werden. Das LJ modelliert die Wechselwirkungen zwischen zwei ungeladenen ungebundenen Teilchen durch ein Kombination der anziehenden Van-der-Waals-Kräfte und des abstoßenden Effekts des Paulisches Ausschließungsprinzips, und nähert damit die finite Größe des Teilchens an.

1.3 Elektrophorese großer nackter Kolloide

Elektrophorese ist die Bewegung geladener Teilchen durch eine Flüssigkeit unter Einwirkung eines angelegten elektrischen Feldes. Diese hat zahlreiche Anwendungen als Trenntechnik für Moleküle oder bei der Charakterisierung der Oberflächeneigenschaften geladener Teilchen. Ein solches Teilchen beschleunigt unter den Einwirkung des angelegten Feldes bis alle beteiligten Kräfte ins Gleichgewicht geraten und sich eine konstante Driftgeschwindigkeit einstellt. Die interessante Größe eines Elektrophoreseexperiments ist die elektrophoretische Mobilität, d.h. der Quotient von Driftgeschwindigkeit und elektrischer Feldstärke. Dabei ist für schwache Felder die Mobilität unabhängig von der Feldstärke.

Die überschüssigen Gegenionen, die sich um eine geladene Oberfläche in einer Lösung sammeln, bewegen sich auch unter der Einwirkung das angelegten Feldes und setzen dadurch auch die Flüssigkeit in Bewegung. Diese Strömung ist als der elektro-osmotische Fluß bekannt und weit weg von der Oberfläche ist seine Größe äquivalent zur negativen elektrophoretischen Mobilität eines stationären Teilchens.

Im Fokus dieser Arbeit liegt die Elektrophorese von Kolloiden. Die kolloidalen Teilchen, die in Experimenten benutzt werden, haben meist einen Durchmesser von etwa einem Mikrometer, womit sie mehrere Ordnungen größer als Ionen sind. Dieser Unterschied der auftretenden Längenskalen macht eine explizite Simulation, in der sowohl die Kolloide als auch die Ionen als Teilchen dargestellt werden, praktisch unmöglich. Wenn die Ionen-Korrelationen schwach sind, kann man Molekularfeldtheorie (mean-field theory) benutzen, wobei die Ionen in der Simulation nur als Ladungsdichte in die Berechnung der elektrostatischen Wechselwirkungen eingehen. In manchen Fällen wie denjenigen, die in dieser Arbeit untersucht wurden, spielen die Ionen-Korrelationen eine große Rolle und können nicht ignoriert werden. Dafür wurde ein neues Model entwickelt, das die Größe des Kolloids ausnutzt und es erlaubt, Ionen explizit zu simulieren. Ist die Debye Länge des Systems viel kleiner als alle seine anderen charakteristischen Längen, sind die meisten Gegenionen so nah an der Oberfläche, dass die lokale Krümmung ignoriert werden kann. Die Geometrie ist planar und das kugelförmige Teilchen kann als eine flache Ebene dargestellt werden. Mit Hilfe dieses Modells können Simulationen ohne die Anwesenheit eines elektrischen Feldes durchgeführt werden, wobei das sogenannte Zeta-Potential bestimmt wird. Das Zeta-Potential ist das elektrische Potential am Rand der Abscherschicht, an der die Scherung von der Flüssigkeit in Bezug auf das Teilchen anfängt. Die elektrophoretische Mobilität steht in Zusammenhang mit dem Zeta-Potential und kann davon abgeleitet werden. Die Umrechnung kann in manchen Grenzfällen durch analytische Näherungen geschehen oder numerisch berechnet werden, wofür häufig das sogenannte standard Electrokinetic Model (SEM) benutzt wird. Es basiert auf einer molekularfeldtheoretischen Beschreibung der elektrostatischen Wechselwirkungen, die mit der Nernst-Planck-Gleichung für die Beschreibung des Ionen Transports, einschließlich Advektion, kombiniert wird. Schließlich wird die Mobilität aus dem Zeta-Potential berechnet, das hier durch Simulationen bestimmt wurde. So werden die wichtigen Ionen Korrelationen, trotz der Molekularfeldnäherung des SEM berücksichtigt.

Dieses Modell wird mit experimentell bestimmten Mobilitäten kolloidarer Teilchen in Salzlösungen verschiedener Valenzen und Konzentrationen verglichen. Dabei wurde das Phänomen der Mobilitätumkehr (mobility reversal) in Relation zur Salzkonzentration genauer untersucht, die in Experimenten mit trivalenten Gegenionen beobachtet wurde. Mobilitätumkehr wird durch Landungsumkehr (charge inversion) verursacht, die durch Anziehung zusätzlicher Gegenionen passiert. Ionen Korrelationen spielen dabei eine entscheidende Rolle und werden von vielen als Hauptursache vermutet. Die durchgeführten Simulationen zeigen, dass dies für die hieruntersuchten Systeme nicht der Fall ist und ein zusätzlicher Einfluss nötig ist, die Landungsumkehr hervorzurufen. Es stellt sich heraus, dass dieser mit der spezifische Adsorption (specific adsorption) zwischen den trivalente Gegenionen und Kolloidarfläche erklärt werden kann und es wird vermutet, dass diese in den untersuchten Fälle durch Hydrolyse der Ionen verursacht wird. Leider erlaubt das verwendete Modell keine genauere Aussage darüber.

1.4 Elektrophorese weicher Kolloide

Polyelektrolyt-gepfropfte Kolloide, die man auch als weiche Kolloide bezeichnet, haben wichtige Anwendungen in biologischen, wie auch in industriellen Systemen. Die gepfropften Polymere beeinflussen manche Eigenschaften des Teilchens oder der Oberfläche, unter anderem die elektrokinetischen. Da die Polymere gepfropft sind und sich nicht frei bewegen können, üben sie eine zusätzliche Reibungskraft auf die Flüssigkeit aus und schirmen damit den elektroosmotischen Fluss ab, der durch die Ionenbewegung innerhalb der Polyelektrolytschicht entsteht. Dabei nimmt die Abschirmung mit der Dicke der Schicht zu. Falls geladen, ändern die Polymere auch die Ladungsverteilung, was auch auf das elektrokinetische Verhalten des

Systems Einfluss nimmt. Für eine korrekte Beschreibung derartiger Teilchen, z.B. biologischer Zellen, die oft natürlich behaart sind, ist es dann wichtig, dass die Theorie diese Effekte in Betracht zieht. Die Darcy-Brinkman-Gleichung, die ursprünglich für poröse Medien entwickelt wurde, beschreibt die zusätzliche Reibung der gepfropften Polymere durch eine dissipative Volumenkraft in der Stokes'sche Gleichung. Diese hängt von der Permeabilität der Polymerschicht ab, die hingegen selbst vom Ort abhängt. Je größer die Permeabilität ist desto kleiner ist die Reibung. Im Falle von geladenen Polymeren ist die fixierte Ladung in der elektrostatischen Volumenkraft inbegriffen. Zusammen mit einer Nernst-Planck-Gleichung für den Ionentransport einschlißlich Advektion bietet die Darcy-Brinkman Gleichung eine gute Basis für die Beschreibung des elektrokinetischen Verhaltens weicher Teilchen.

Im zweiten Teil dieser Arbeit wurde die Elektrophorese weicher Kolloide durch Teilchenbasierte MD Simulation studiert. Zu diesem Zweck wurden die hydrodynamischen Wechselwirkungen, die eine wichtige Rolle spielen, mit Hilfe des Lattice-Boltzmann (LB) Algorithmus simuliert. Das Kolloid wird wie eine sphärische Brombeere dargestellt, die aus einem zentralen Teilchen besteht, dessen Oberfläche von mehreren Teilchen im Abstand der gewünschten Radiuses gebildet wird. Dieses Model heißt Brombeer-Modell (the raspberry model) und ermöglicht die Beschreibung der hydrodynamischen Wechselwirkung des Kolloids als eine Sphäre mit bestimmtem Radius. Die Oberflächenteilchen werden dabei durch eine punktuelle Reibungskraft an eine LB-Gitter-Flüssigkeit gekoppelt. Falls nötig, wird dem zentralen Teilchen eine negative Ladung gegeben. Für die Polymere wird das Massenpunkt-Feder-Modell benutzt, wobei die Monomere sphärische Kugeln sind, die durch elastische Bindungen verbunden werden. Hier wird die Bindung mit dem "Finitely Extensible Nonlinear Elastic" Potential (FENE) modelliert. M Polymere mit je N Monomeren sind gleichmäßig an die Brombeerenoberflächenmassenpunkte durch FENE Bindungen aufgepfropft. Einem Teil der Monomere wird zufällig eine positive Einheitsladung gegeben. Die Gegenionen und die Salzionen sind geladene Kugeln, und alle Teilchen sind durch ein Reibungspotential mit der Flüssigkeit gekoppelt.
Um die elektrophoretische Mobilität zu messen, wird ein externes elektrisches Feld angelegt, so dass eine elektrostatische Kraft auf alle geladenen Teilchen wirkt. Nach einer Weile erreicht das Kolloid einen stationären Zustand, in dem die Massenschwerpunktsgeschwindigkeit des Kolloids sich mit der Zeit nicht mehr ändert. Diese Driftgeschwindigkeit wird schließlich durch die Feldstärke geteilt, woraus sich die Mobilität ergibt.

Der Einfluss von Salzkonzentration und Ladungen wurde an zwei Typen weicher Kolloide untersucht; ein insgesamt ungeladener und ein insgesamt geladener. Im ersten Fall balanzieren sich die Ladungen auf den Polyelektrolyten und dem Kolloid aus, wohingegen im zweiten Fall die eine größer ist als die andere, wodurch der weiche Kolloid eine Nettoladung erhält. Bei der Elektrophorese weicher Kolloide spielt die Relation zwischen der Höhe der gepfropften Polymerschicht und der Debye-Länge des Systems eine entscheidende Rolle. Beide Gegenionenarten, die des zentralen Kolloids und die der Polyelektrolyte, erzeugen eine elektro-osmotische Strömung. Da sie entgegengesetzte Ladungen haben, fließen die zwei Strömungen in entgegengesetzte Richtungen und arbeiten gegeneinander. Wenn die Debye-Länge viel kürzer ist als die Höhe der Schicht, befinden sich die Gegenionen innerhalb der Schicht und deren Strömung wird abgeschirmt. Da die Gegenionen des Kernkolloids weiter nach innen dringen als die der Polyelektrolyte, wird der Fluss den sie erzeugen stärker abgeschirmt und die elektroosmotische Strömung der Polyelektrolyte dominiert. Dieser einfache Mechanismus bewirkt interessante und überaschende Phänomene, die hier teilweise zum ersten Mal beschrieben und untersucht werden. Eines dieser Phänomene ist die Elektrophorese eines insgesamt ungeladenen weichen Kolloids in positiver Richtung bei moderaten und hohen Salzkonzentrationen. Die positive Mobilität ist ein Hinweis auf die Dominanz der positiv geladenen Polyelektrolyte und der Wert steht im Einklang mit theoretische Vorhersagen. Genaue Untersuchungen an den Monomer- und Ladungsverteilungen zeigen, dass die obengenanten Mechanismus dafür verantwortlich ist.

Das wichtigste Ergebnis dieses Teils meiner Arbeit ist die Beobachtung, dass ein insgesamt negativ geladener weicher Kolloid eine Mobilitätumkehr durchgeht, wenn die Konzentration des monovalenten Salzes geändert wird. Bei niedrigen Salzkonzentrationen befinden sich Gegenionen außerhalb der Polyelektrolyteschicht und ihre elektro-osmotische Strömung ist nicht abgeschirmt. In diesem Regime verhält sich das weiche Kolloid wie ein nacktes und die Gesamtladung bestimmt die Mobilität. In dem Regime hoher Salzkonzentration dominiert die durch den Polyelektrolyten erzeugte Strömung und der negative weiche Kolloid hat eine positive Mobilität. Dieses Phänomen wird in dieser Form zum ersten Mal hier beschrieben, ist aber in Übereinstimmung mit Kontinuumstheorien. Dabei ist es wichtig zu beachten, dass diese Mobilitäts-umkehrung von ganz anderer Natur ist als die jenige, die durch Ladungskorrelationen von multivalent Salzen hervorgerufen wird.

Zu Vergleichszwecken ist ein numerisches Modell benutzt worden, wobei die gepfropften Polyelektrolyte als gleichmäßig verteilte Stokes Teilchen dargestellt wurden, die durch die obengenannten Darcy-Brinkman-Gleichung eine zusätzliche Reibungskraft ausüben. Alle Mobilitätsergebnisse wurden mit numerisch erhaltenen Resultaten verglichen und bestätigen die Gültigkeit der Darcy-Brinkman Gleichung und ihre Brauchbarkeit für die Beschreibung des elektrokinetischen Verhaltens weicher Teilchen. Nur in Fällen, in denen Simulationen mit extrem hoher Ladung benutzt wurden, bricht die Molekularfeldbeschreibung der elektrostatischen Wechselwirkungen zusammen und somit auch die Theorie. Solche Fälle sind zwar unrealistisch, zeigen jedoch die beteiligten Mechanismen der Elektrophorese weicher Kolloide sehr gut.

Durch die numerische Methode wurde gezeigt, dass die in den Simulationen beobachtete Mobilitätsumkehr in Bezug auf monovalente Salzkonzentration auch für Kolloide mit experimentell relevanten Durchmessern auftritt. Dieses Phänomen könnte wichtige Anwendungen finden, wie z.B. bei der Messung lokaler Salzkonzentrationen.

2 Introduction

Soft condensed matter, or simply soft matter, is a branch of condensed matter in which the materials are neither simple liquids nor crystallised solids. Soft matter is an important part of everyday life and also has many applications in industry. Familiar materials such as cosmetics, paints, glues, most foods, soaps, as well as less familiar ones like complex fluids and polymer melts fall within the soft matter category. Most significantly, biological systems share many properties with soft matter and the physical mechanisms involved in living beings can be understood using the concepts of this branch of physics.

The important properties which characterize soft matter are the length scale (between atomic size and macroscopic scales) and the energy scale (of the order of the thermal energy). The relatively large length scales allow one to use coarse-grained models and theories where not every atomistic detail needs to be taken into account. A direct consequence of this is the universality of many aspects of soft matter. The comparability of the typical enthalpies in such systems to the thermal energy makes the role of fluctuations and Brownian motion crucial. The propensity of soft matter to self-assemble is related to this fact; the balance between entropy and energy drives the system towards complex equilibrium states, making the phase diagram of soft matter systems richer and more interesting.

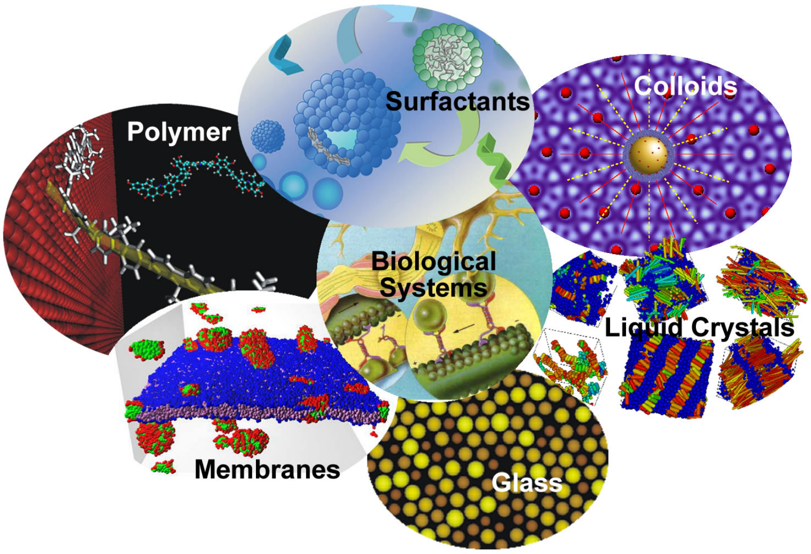

Figure 2.1: A schematic diagram of the typical soft matter systems. Figure taken from the website of the Center for Soft Condensed Matter Physics and Interdisciplinary Research.

Fig. 2.1 shows some of the typical systems of soft condensed matter. Colloids and polymers, ubiquitous in biological and technological systems, are two of the most important ones. Polymers are large molecules comprised of many small subunits called monomers connected together via bonds as shown schematically in Fig. 3.11. Biological polymers such as DNA and proteins are an essential and inseparable part of biological systems. Synthesized artificially for the first time in the early 1900s [8], artificial polymers (e.g. plastics) have become omnipresent in everyday life such that modern living without them is unimaginable. Colloidal suspensions consist of nm $-$ μm-sized particles, usually referred to as colloids, dispersed in a liquid. They include many substances, such as milk, paints, and blood, and are encountered frequently in various fields, from industry to medicine and pharmacology. They also serve as simple models for a variety of systems like atoms, proteins, and bacteria. As such, colloids can be used to study many different physical phenomena, for example crystallization [9, 10] and crystal melting [11–13], phase behavior [14–16], and the effect of electrostatic interactions on biological processes [17].

When suspended in a polar liquid like water, most particles become electrically charged because they possess surface groups which can dissociate. This plays an important role in their behaviour, for example stabilizes colloidal suspensions against coagulation. The magnitude and distribution of the surface charge is, however, usually not *a priori* known and needs to be inferred from related quantities and experimental observations. One of the key techniques used for this purpose is electrophoresis, in which an electric field is externally applied on a system comprised of charged particles. Electrophoresis is also often used to separate particles according to their length and/or charge. For example, without it the sequencing of the entire human genome would have not been possible [18, 19].

As a result of the electric force exerted on a charged particle in electrophoresis, it starts moving. The fluid opposes this movement by exerting a hydrodynamic drag force. In addition, in an electrolytic solution the salt ions form an ionic could around the charged particle usually referred to as the electric double layer. It consists of a layer of counterions co-moving with the particle, the so-called Stern layer, and a diffuse layer of both counterions and coions. The part close to the interface mainly consists of counterions, i.e. ions with a charge opposite to that of the particle. These ions also respond to the applied electric field and exert direct and indirect forces on the particle, retarding its motion. In the steady state, the net force on the particle is zero and it acquires a constant drift velocity, the ratio of whose magnitude to the applied field strength defines the central quantity in electrophoresis, the electrophoretic mobility. The counterpart of the electrophoretic mobility for stationary surfaces is the electro-osmotic mobility. When brought to move by the applied field, the excess charge in the electric double layer drags the fluid along with it, creating a far-field disturbance in the fluid called the electro-osmotic flow (EOF). The velocity of the fluid far from the surface is equal to the negative of the electrophoretic velocity and the ratio of its magnitude to the field strength yields the electro-osmotic mobility.

Theoretically, a set of coupled second-order differential equations, referred to as the electrokinetic equations, needs to be solved in order to calculate the electrophoretic mobility. One of the boundary conditions used to solve the electrokinetic equations, is the so-called ζ-potential, i.e. the potential drop at the slip plane, where the fluid starts shearing with respect to the particle. The mobility is thus related to particle properties, such as its shape and surface charge density, and can be used to extract useful and important information about charged particles, such as colloids and polyelectrolytes. This is, however, not always a straight forward task and requires an appropriate theory which takes all the important properties of the system into account. Most theories use mean-field approaches, such as Poisson-Boltzmann, to calculate the ion distribution in the electric double layer. Mean-field theories neglect the ion correlations, crucial to many behaviors of charged systems, and thus fail to explain some of the important phenomena. An example of this is the reversal of the electrophoretic mobility in the presence of multivalent salt observed in many experiments [4, 5, 20–23]. It is closely related to charge inversion, where the surface charge is overcompensated by the counterions, which is in turn mainly caused by ion correlations. Computer simulations can help understanding these important and interesting phenomena and give more insight into the mechanisms involved. Therefore, this thesis is devoted to a molecular dynamics study of colloidal electrophoresis. Below, the main aspects of the methods developed here for this purpose and the most important results are summarized.

2.1 Electrophoresis of Large Bare Colloids

Ch. 4 of this thesis deals with molecular dynamics simulations of the electrophoresis of bare colloids, with the focus on the mobility reversal in the presence of trivalent ions. The colloids considered are a few orders of magnitude larger than the ions, rendering efficient simulations with explicit colloids and ions even at the coarse-grained level. On the other hand, the ion correlations need to be present for the charge inversion, and consequently the mobility reversal, to occur. In order to resolve this problem, a model is developed here which makes use of the length scale separation in the system and considers the colloid as a uniformly charged flat surface. The validity of the planar assumption is checked by comparing the $\zeta-$potentials obtained from numerical solutions to the spherical and planar nonlinear Poisson-Boltzmann equation. The restricted primitive model is employed, where the solvent is modeled implicitly as a dielectric continuum medium and the ions explicitly as charged spherical particles. Periodic boundary conditions are applied parallel to the charged plate, and the system is confined in the perpendicular direction.

Since most experiments are performed using weak applied fields for which the linear response regime is valid, it is safe to assume that the electric double layer is not deformed significantly. Thus, the $\zeta-$potential can be obtained from equilibrium simulations in the absence of an applied electric field. The so-called standard electrokinetic model (SEM) [24, 25] is then used to convert this quantity to the electrophoretic mobility. It uses the Poisson-Nernst-Planck equation, with an additional advection term, coupled to the Stokes equation and applies a first-order perturbation with respect to the electric field to linearize and eventually uncouple the electrokinetic equations. It needs to be emphasized that even though the SEM is based on a mean-field theory for the electrostatic interactions, the ζ-potentials are obtained from simulations with explicit ions and thus, the crucial ion correlations are incorporated.

This novel simulation method is applied to two distinct experimental data sets of the electrophoretic mobility of large bare colloids (few hundred nm to few μm in radius) in mono-, di-, and trivalent salt solutions of varying ionic strengths. The results agree very good with the experiments for the mono- and divalent cases. Most importantly, they reproduce the mobility maximums at roughly the same ionic strengths as in the experiments. In both data sets, a mobility reversal is reported in the presence of trivalent ions. Simulations reveal that the correlations are not strong enough in the systems investigated and an *additional* short-ranged attraction is needed for the mobility reversal to occur at the experimentally observed salt concentrations. This attraction mimics specific adsorption between the trivalent ions and the colloid, the existence of which has been suggested by many authors. The simulation results also show that charge inversion is a necessary but not sufficient condition for mobility reversal.

2.2 Electrophoresis of Soft Colloids

In Ch. 5 of the work in hand, the electrophoretic behaviour of polyelectrolyte-grafted colloids, also referred to as soft colloids, is investigated. Soft particles are often encountered in biological and artificial systems; they exist in most vascular boundaries and tissues [26], many cells and bacteria are coated with polymers [27, 28]. The coating affects the adhesion of microbes and bacteria [29], and as such the infection rate [30], as well as the rheological properties of electrorheological fluids [31, 32] and the stability of colloidal suspensions [33]. In tissue engineering, thermoresponsive polymer-grafted surfaces are used to duplicate natural tissue functions more effectively and control cell adhesion/detachment dynamics [34, 35]. Evidence from electrophoresis experiments suggests that humic substances, involved in many processes in soils and natural waters, have a permeable layer and can be modeled as polymer-grafted colloids [36]. Soft particles have also proven to be useful as drugs and gene delivery vehicles [37–39] in the body. They also have many applications in industry and are used to control the electrokinetic properties of surfaces in micro- or nanofluidic devices [40–42]. It is therefore of great importance to investigate such surfaces and electrophoresis provides a good means for studying and understanding their electrical and surface properties.

Since the polymers are grafted and cannot move with respect to the substrate, they screen the electro-osmotic flow generated by the penetrated ions in an electrophoresis procedure. The extent of the screening is larger for larger monomer concentrations, and is therefore distant-dependent in e.g. spherical geometry. When the grafted chains are charged, the EOF produced by their counterions competes with that of the underlying surface, which leads to complex electrokinetic behaviors. The simulations discussed in Ch. 5 reveal some counterintuitive phenomena in electrophoresis of soft colloids and help understanding them by careful investigation of the ions and monomers distributions. The colloidal core is simulated using the raspberry model consisting of a central particle wrapped around by many surface beads. The central particle is given a negative charge and the surface beads are used as grafting points for the chains. The number of the polymers is chosen such that the layer is in the brush regime, i.e. the chains stretch out due to steric interactions in order to avoid overlapping each other. Only in this regime is the EOF effectively screened. A fraction of the monomers are charged positively and the ions are also modeled explicitly as charged spheres. Hydrodynamic interactions are taken into account via a lattice-Boltzmann (LB) solvent in which all the particles are treated as point particles dissipatively coupled via a Stokes' force scheme. The use of the raspberry model for the core is therefore necessary in order to take into account its finite hydrodynamic size. The coupling also acts as a thermostat and keeps the temperature at room temperature. An electric field is applied as a constant force on the charged particles and the drift velocity of the center of mass of the colloid is measured after equilibrating the system in order to calculate directly the electrophoretic mobility.

Investigations of the effect of monovalent salt concentration on the mobility of a net-neutral soft colloid, where the negative charge of the core is compensated by the total positive charge on the polyelectrolytes, show that it moves in the direction of the applied field at moderate and high salt concentrations. At low salt concentrations, there are hardly any ions in the system and even less enter the brush. The soft colloid behaves similar to a neutral bare sphere and has a negligible mobility. As the salt concentration increases, the Debye length becomes comparable to the brush height and more and more ions penetrate the polymer layer where their EOF is screened. Since the counterions of the polyelectrolytes are further from the surface, the EOF they generate is less strongly screened and partly reaches the bulk, driving the soft colloid in the positive direction.

The most important result of this part of the thesis is the mobility reversal of a negatively net-charged soft colloid with respect to *monovalent* salt concentration. Again at low salt concentrations, one could compare the composite to a solid sphere which moves in the opposite direction of the applied field due to its negative charge. Upon adding more salt, more ions penetrate the polymer layer, where the two competing EOFs, namely that of the core and that of the polyelectrolytes, are unequally screened. The EOF produced by the negative counterions partially reaches the bulk and the negative soft colloid moves in the positive direction. It is important to note that this mobility reversal is completely different from the one reported for bare surfaces in the presence of multivalent salt mentioned in the previous section. While the latter results from overcharging due to ion correlations and/or specific attractions, the former is a consequence of the screening effect of the grafted layer and the interplay between the two characteristic length scales of the system, i.e. the Debye length and the brush height.

Further, the effect of other parameters, such as core and polyelectrolyte charges, on the mobility of net-neutral and net-charged soft colloids are investigated. All the results are compared to both approximate analytic expressions derived by Ohshima *et al.* [43, 44] and numerical solutions based on a Darcy-Brinkman formulation of the standard electrokinetic model for polymer-grafted spherical colloids developed by Hill *et al.* [7]. The agreement between simulation and numerical results is very good except at extremely large charge densities, where the excluded volume of the ions, which are ignored in the underlying mean-field theory used in the numerical approach, start to play an important role. The good agreement at reasonable charge densities, confirms the validity of the coupled differential equations used in the literature to describe the electrokinetic behavior of soft interfaces. The agreement with Ohshima's approximate expressions, on the other hand, is restricted to regions where the underlying assumptions of the theory are met and the effect of the ionic finite size can be ignored. This effect is only considerable at very large charges which are unlikely to occur in experiments, and both the theoretical and numerical approaches can be safely used to describe the electrokinetic behaviour of soft colloids given that other criteria for their validity are fulfilled.

3 Theory

This chapter deals with theoretical principles used in this thesis. In Sec. 3.1 the classical molecular dynamics is introduced. The concept of coarse graining, and the coarse-grained potentials employed in the simulations in this thesis are discussed in Sec. 3.2. Hydrodynamic and electrostatic interactions, and the corresponding algorithms used here to include them in the simulations, are explained in sections 3.3 and 3.4, respectively. Electrophoresis, the main topic of this thesis, is discussed in Sec. 3.5 where the electrokinetic equations, and theoretical and numerical methods to solve them are presented for both bare and polymer-coated colloids. The basics of polymer statics are introduced in Sec. 3.6.

3.1 Classical Molecular Dynamics

Computer simulations provide a powerful tool for studying diverse systems, especially those not directly accessible by experiment. They also serve as a means of validating theories or deriving additional information that is not extractable from experiments. It is easier to control different parameters in a simulation, interactions can be tuned or even completely turned off to investigate their effect on the behavior of the system at hand; something which is extremely helpful for finding the cause of an observed phenomenon. With todays ever-improving computational resources, computer simulations have become an important part of modern physics and are now considered on par with theory and experiment. In what follows the principles of classical Molecular Dynamics (MD), one of the main simulation methods, is described. Most of the content in this section has been taken from Allen and Tildesley's book "Computer Simulation of Liquids" [45] and Frenkel and Smit's book "Understanding Molecular Simulations" [1]. Also some parts have been taken from the statistical mechanics textbook of Pathria [46].

MD is a computer simulation method in which the time evolution of particle trajectories is calculated based on Newton's equations of motion. It can be used to simulate systems of hundreds of thousands to millions of atoms as well as molecules. The fact that in many cases the classical equations of motion can be used to describe the trajectories of atoms is a consequence of the two basic assumptions made in all classical MD simulations, namely the Born-Oppenheimer (BO) approximation and the treatment of the nuclei as point particles following classical dynamics. The BO approximation makes use of the high ratio between nuclear and electron masses and allows for the separation of the wavefunction of a molecule into an electronic and a nuclear part. The electrons are much faster than the nuclei and can adjust themselves almost instantaneously to the movements of the latter so that their effect can be considered as a potential energy surface. The energy of the system is then only a function of the nuclei's coordinates. Without the BO approximation, the electrons would need to be considered explicitly, which would limit the applicability of MD simulations to very simple systems. The validity of the second basic assumption in MD simulations can be determined by the thermal de Broglie wavelength, $\Lambda_{\mathrm{th}} = h/\sqrt{2\pi m k_{\mathrm{B}} T}$ where h is the Planck constant, m the mass, and $k_{\mathrm{B}}T$ the thermal energy. Quantum effects are significant only when Λ_{th} is of the order of or larger than the interparticle distances, d. Except for the lightest atoms, the condition $\Lambda_{\mathrm{th}} \ll d$ applies at sufficiently high temperatures and the atoms can be safely considered as classical particles. For example, the thermal de Broglie wavelength of gold atoms (Au) at room temperature is $\Lambda_{\mathrm{th}} = 0.07$ Å whereas the typical interatomic distance in solids is $d \sim 1 - 3$ Å.

MD simulations are used to measure macroscopic equilibrium and transport properties of the system from microscopic information using the laws of classical thermodynamics and statistical mechanics. A short review of the important laws, without proofs, is presented below.

The most important assumption in thermodynamics is that a system consisting of a fixed number of particles N in a fixed volume V having a fixed energy E is *equally* likely to be in any of its $\Omega(N, V, E)$ microstates. Consider two weakly interacting systems, exchanging *only* energy with the total energy of the composite system $E = E_1 + E_2$ being fixed. Each subsystem n is equally likely to be found in any of its $\Omega_n(E_n)$ microstates, thus the composite system has $\Omega(E_1, E_2)$ equally likely microstates which can be written as:

$$\Omega(E_1, E_2) = \Omega_1(E_1)\Omega_2(E_2) = \Omega_1(E_1)\Omega_2(E - E_1) = \Omega(E, E_1) \tag{3.1}$$

Equilibrium is the state in which the number of possible microstates of a system is maximized. Maximizing $\Omega(E, E_1)$ with respect to E_1 and making use of the fact that $\partial E_2/\partial E_1 = -1$, one obtains that in equilibrium the following condition holds:

$$\left(\frac{\partial \ln \Omega_1(E_1)}{\partial E_1}\right)_{E_1=\bar{E}_1} = \left(\frac{\partial \ln \Omega_1(E_2)}{\partial E_2}\right)_{E_2=\bar{E}_2}, \tag{3.2}$$

where $\bar{E_n}$ denotes the equilibrium value of E_n. Defining $\beta(E, V, N)$ as:

$$\beta(E, V, N) \equiv \left(\frac{\partial \ln \Omega(E, N, V)}{\partial E}\right)_{N,V}, \tag{3.3}$$

the two systems are said to be in equilibrium with each other when $\beta(E_1, V_1, N_1) = \beta(E_2, V_2, N_2)$. Comparing Eq. 3.3 with the thermodynamic definition of absolute temperature T as $1/T = (\partial S/\partial E)_{N,V}$, where $S(N, V, E) \equiv k_{\mathrm{B}} \ln \Omega(N, V, E)$ is the entropy, one finds that $\beta^{-1} = k_{\mathrm{B}}T$. k_{B} is the Boltzmann constant and $k_{\mathrm{B}}T$ the thermal energy ($k_{\mathrm{B}}T = 4.11 \times 10^{-21}$ J at room temperature $T = 298$ K).

As mentioned above, the energy states of the composite system, for which the energy is fixed, are all equally likely; but the distribution of energies over the two subsystems has different probabilities. The probability to find system 1 in state i with $E_i = E - E_2$, is

$$P_i = \frac{\Omega_2(E - E_i)}{\sum_j \Omega_2(E - E_j)}. \tag{3.4}$$

If one system, say system 2, is much larger than the other, it can be considered as an energy reservoir with $E_i \ll E_2 \approx E$. In this case, to find $\Omega_2(E - E_i)$, $\ln \Omega_2(E - E_i)$ is Taylor expanded to the second degree in $E_i(\ll E)$ and the definition of β is used. One then obtains

$$P_i = \frac{\exp(-\beta E_i)}{\sum_j \exp(-\beta E_j)}, \tag{3.5}$$

which can be used to calculate the average of a system's property such as its energy

$$\langle E \rangle = \sum_i E_i P_i = \frac{\sum_i E_i \exp(-\beta E_i)}{\sum_j \exp(-\beta E_j)} = -\frac{\partial \ln \sum_i \exp(-\beta E_i)}{\partial \beta} = -\frac{\partial \ln Q}{\partial 1/k_{\mathrm{B}}T}, \tag{3.6}$$

where $Q \equiv \sum_i \exp(-\beta E_i)$ is the partition function. The Helmholtz free energy F_{H} with the thermodynamical definition $E = \frac{\partial F_{\mathrm{H}}/T}{\partial 1/T}$, can be written as

$$F_{\mathrm{H}} = -k_{\mathrm{B}}T \ln Q = -k_{\mathrm{B}}T \ln \left(\sum_i \exp(-E_i/k_{\mathrm{B}}T) \right). \tag{3.7}$$

Since the number of possible microstates is maximum in equilibrium, the Helmholtz free energy of a system with constant temperature and volume is minimised.

The averaging process introduced in Eq. 3.6 is called ensemble averaging and is static, *i.e.* it considers the instantaneous state of the system. On the other hand, an MD program is, as the name suggests, dynamic and its goal is to simulate the evolution of the system and the average properties over *time*. In general these two are not equivalent. In addition, in practice as well as in simulations, the requirement $t_{\mathrm{obs}} \to \infty$ for finding the observable value from a time average, is not satisfied. Instead many measurements are performed at different times for a finite time length t_{obs}. The question is then if the average of these measurements is equal to the desired time average. The microstate of a system at any time t is specified by the (generalized) positions $\vec{q}_i$ and momenta $\vec{p}_i$ of *all* the particles constituting it. For a system with N particles these form a $6N$-dimensional space, called *phase space*. Each possible microstate can be viewed as a member of an ensemble of systems all having the same *macrostate*. Different ensembles exist, denoted by the corresponding fixed properties such as the microcanonical ensemble NVE, the canonical NVT ensemble, and the isothermal–isobaric NPT ensemble where P is the pressure. The microstates, or equivalently the members of the ensemble, are distributed according to a density function $\rho(q, p; t)$. Therefore, the ensemble average of a physical quantity f reads

$$\langle f \rangle = \frac{\int f(q,p)\rho(q,p;t)\mathrm{d}^{3N}q\mathrm{d}^{3N}p}{\int \rho(q,p;t)\mathrm{d}^{3N}q\mathrm{d}^{3N}p}. \tag{3.8}$$

In equilibrium, $\partial\rho/\partial t = 0$ and therefore, $\langle f \rangle$ does not change with time and taking its time average does not change the result. Consequently,

the ensemble average of f=the time average of the ensemble average of f.

These two averaging processes are independent and the order in which they are taken can be switched. Therefore,

$\langle f \rangle$ =the ensemble average of the time average of f.

Taken over a sufficiently long time, the time average of f must be the same for all members of the ensemble and thus the ensemble average should not change it and $\langle f \rangle$ can be written as

$$\langle f \rangle = \text{the long-time average of } f.$$

The ultimate result of this long line of argument is that for an ergodic system (see below) in equilibrium, the time average can be replaced by the ensemble average.

It is important to emphasize that the assertion made in the last step of the arguments above is not true when the time average is taken only over a short time. In that case, only a subset of microstates (or equivalently a small region of the phase space) will be spanned and some states will be *favored* over others. Employing a long time interval, however, one can expect the system to pass through almost all possible states, i.e. almost the whole allowed region of the phase space is explored. Such a system for which a representative point ultimately traverses *every* possible phase point when evolved over a long time, is called an *ergodic* system. In this case, the averages depend only on the *macrostate* and not the microstates of the system. Ergodicity is only a hypothesis and there exist systems which are not ergodic, e.g. glasses, metastable phases, or systems for which the phase space is disconnected.

As the phase points evolve in time, $\rho(\vec{q}, \vec{p}; t)$ changes as well. According to Liouville's theorem the total time derivative of the probability density is conserved. In other words, no system is created or destroyed in the ensemble. Mathematically, this means

$$\frac{\mathrm{d}\rho}{\mathrm{d}t} = \frac{\partial \rho}{\partial t} + \sum_i \dot{\vec{q}}_i \cdot \vec{\nabla}_{\vec{q}_i} \rho + \sum_i \dot{\vec{p}}_i \cdot \vec{\nabla}_{\vec{p}_i} \rho = \frac{\partial \rho}{\partial t} + \dot{\vec{q}} \cdot \vec{\nabla}_{\vec{q}} \rho + \dot{\vec{p}} \cdot \vec{\nabla}_{\vec{p}} \rho = 0. \tag{3.9}$$

where $\dot{x}$ represents the time derivative of x. Defining the Liouville operator $\mathcal{L}$ as $i\mathcal{L} = \dot{\vec{q}} \cdot \vec{\nabla}_{\vec{q}} + \dot{\vec{p}} \cdot \vec{\nabla}_{\vec{p}}$, Eq. 3.9 can be written as

$$\frac{\partial \rho}{\partial t} = -i\mathcal{L}\rho, \tag{3.10}$$

with the formal solution $\rho(\vec{q}, \vec{p}; t) = \rho(\vec{q}, \vec{p}; 0) \exp(-i\mathcal{L}t)$.

The equilibrium condition $\partial\rho/\partial t = 0$ mentioned above is a balance equation and means that whenever a representative phase point (or a member of the ensemble) evolves from $\{\vec{q}(t), \vec{p}(t)\}$ to $\{\vec{q}(t + \delta t), \vec{p}(t + \delta t)\}$, another will evolve from $\{\vec{q}(t - \delta t), \vec{p}(t - \delta t)\}$ to $\{\vec{q}(t)\vec{p}(t)\}$.

We now have the necessary background knowledge to understand how an MD simulation works. An MD simulation is nothing but a computer program that integrates Newton's equations of motion (EOM) to obtain the trajectories of all the particles in the system and allows for computing averages according to the laws of statistical mechanics. This is done in mainly four steps, as shown in the diagram in Fig. 3.1.

First the positions and the velocities of all the particles are initialized, from which the potentials Φ acting between the particles are calculated. Conservative forces are derived from potentials via the relation $\vec{F} = -\vec{\nabla}\Phi$. In case of pairwise "non-bonded" interactions, this reads $\vec{F}_i = -\vec{\nabla}\Phi(r_{ij})$, where $r_{ij} = |\vec{r}_i - \vec{r}_j|$ is the distance between the two interacting particles. The so-called "bonded" potentials depend specifically on the coordinates of more than two particles and the angles between them. Other forces, such as frictional forces, thermostats, or externally applied forces, as well as constraints are added separately. Usually the forces considered

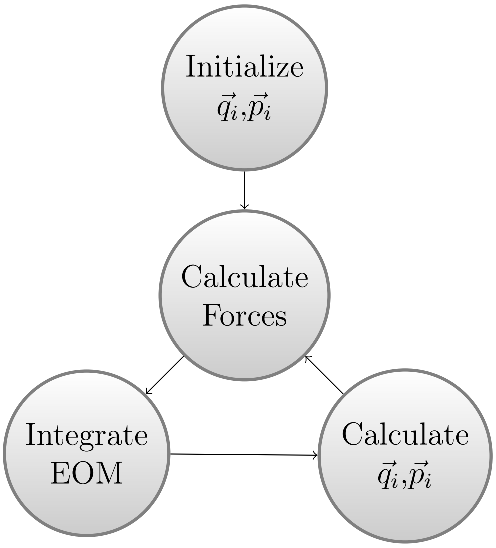

Figure 3.1: A diagram showing the steps taken in an MD simulation.

are pairwise additive and to calculate the force acting on a particle, all the forces acting between that particle and all other particles are summed. The force calculation is therefore the most time-consuming step in an MD simulation and without any special treatment scales as $N(N-1)/2$. Some of the methods for saving computational time and making the simulation more efficient are introduced in subsection 3.1.1. The integration step is not time-consuming, but it is important because many of the principal properties of the simulation, such as time-reversibility or conservation of energy, are determined by the method used. The most common method for the integration is the Verlet algorithm which uses a truncated Taylor expansion of the positions to calculate the new and old coordinates:

$$\begin{aligned} \vec{r}(t+\Delta t) &= \vec{r}(t) + \vec{v}(t)\Delta t + \frac{\vec{f}(t)}{2m}\Delta t^2 + \frac{\Delta t^3}{3!}\dddot{\vec{r}}(t) + \mathcal{O}(\Delta t^4), \\ \vec{r}(t-\Delta t) &= \vec{r}(t) - \vec{v}(t)\Delta t + \frac{\vec{f}(t)}{2m}\Delta t^2 - \frac{\Delta t^3}{3!}\dddot{\vec{r}}(t) + \mathcal{O}(\Delta t^4), \end{aligned} \tag{3.11}$$

where $\vec{r}(t)$ is the position at time t, Δt is the time step, $\vec{v}$ is the velocity, $\vec{f}$ is the force, and $\dddot{\vec{r}}(t)$ denotes the third derivative of the position with respect to time. Summing these two equations yields:

$$\vec{r}(t+\Delta t) \approx 2\vec{r}(t) - \vec{r}(t-\Delta t) + \frac{\vec{f}(t)}{m}\Delta t^2. \tag{3.12}$$

Using $\vec{r}(t+\Delta t) - \vec{r}(t-\Delta t) = 2\vec{v}(t)\Delta t + \mathcal{O}(\Delta t^3)$, the velocity is obtained as:

$$\vec{v}(t) = \frac{\vec{r}(t+\Delta t) - \vec{r}(t-\Delta t)}{2\Delta t} + \mathcal{O}(\Delta t)^2. \tag{3.13}$$

The Verlet algorithm is time-reversible and symplectic (i.e. phase space area preserving) and has the advantage of being fast and using very little computer memory. It has a moderate energy conservation at short times and a small long-term energy drift.

Another commonly used integration method in MD simulations is the leap frog algorithm which has the same properties as the Verlet algorithm. It uses the velocities at half-integer time steps to compute the positions

$$
\begin{aligned}
\vec{v}(t-\Delta t/2) &\equiv \frac{\vec{r}(t)-\vec{r}(t-\Delta t)}{\Delta t}, \\
\vec{v}(t+\Delta t/2) &\equiv \frac{\vec{r}(t+\Delta t)-\vec{r}(t)}{\Delta t}.
\end{aligned}
\tag{3.14}
$$

From the second equation in Eq. 3.14, one directly finds the positions at the next time step as $\vec{r}(t+\Delta t)=\vec{r}(t)+\vec{v}(t+\Delta t/2)\Delta t$. Replacing $\vec{r}(t+\Delta t)$ from Eq. 3.12 in this expression, the relation between the two velocities is obtained as

$$
\vec{v}(t+\Delta t/2)=\vec{v}(t-\Delta t/2)+\frac{\vec{f}(t)}{m}\Delta t. \tag{3.15}
$$

With the leap frog method, the velocities are not calculated at the same time as the positions. This is possible with the similar method of velocity Verlet in which:

$$
\begin{aligned}
\vec{r}(t+\Delta t) &= \vec{r}(t)+\vec{v}(t)\Delta t+\frac{\vec{f}(t)}{2m}\Delta t^2, \\
\vec{v}(t+\Delta t) &= \vec{v}(t)+\frac{\vec{f}(t)+\vec{f}(t+\Delta t)}{2m}\Delta t.
\end{aligned}
\tag{3.16}
$$

Once the equations of motion are integrated and the new positions of all the particles are computed, the whole procedure of calculating the forces and consequently the new positions and velocities is repeated as often as needed and thus the system evolves in time. The properties of interest can then be time-averaged after the system is equilibrated. As explained above, in the limit of very long simulation times, this is equivalent to the ensemble average. However, often one does not simulate the system so long and the phase space is not sampled thoroughly. In practice, to resolve this problem in an efficient manner, one can run many simulations of the same system with different initial parameters and take the average of the time-averages obtained from each.

One is usually interested in the bulk properties of a macroscopic sample and the number of particles even in a very large simulation is by far not enough for the thermodynamic limit ($N \sim 10^{23}$). This changes the surface to volume ratio of the system which in turn affects its behaviour significantly. To avoid this shortcoming, periodic boundary conditions (PBC) are employed where the volume containing the N particles is only considered as the primitive cell in an infinite periodic lattice of identical cells, as depicted in Fig. 3.2. Each particle interacts with all the images of all particles in this lattice. For example, in the case of pairwise additive interactions the total potential acting on a particle i is an infinite sum over the potential between i and all the other particles, including their periodic images:

$$
\Phi_i = \sum_{i,j,\hat{n}}{}' \Phi(|\vec{r}_{ij}+\hat{n}L|), \tag{3.17}
$$

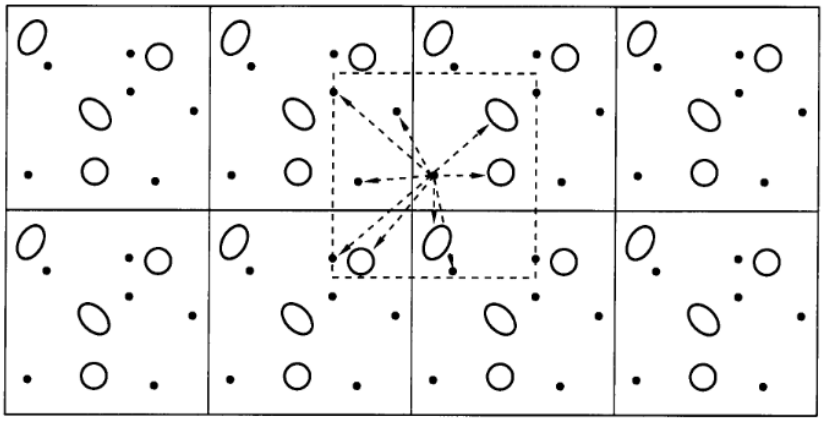

Figure 3.2: A sketch of the periodic boundary conditions. Figure taken from [1].

where $\hat{n}$ is an arbitrary unitary vector, and L is the box length. The prime on the sum indicates that $i \neq j$ for $\hat{n} = \vec{0}$. In this general form PBCs render the simulation impossible since the summation is over an infinite number of image boxes. But many potentials are short-ranged and are truncated beyond a cutoff, so the sum is in practice not to infinity. In the case of long-ranged interactions, such as electrostatic or gravitational interactions, cutting off introduces large errors and hence, there are special methods to deal with them, as discussed in the following sections. Below, I first introduce some commonly-used tricks to minimize the time needed for the force calculation step.

3.1.1 CPU-Time Optimizing Algorithms

As mentioned above, the most time-consuming part of every MD simulation is the force calculation step, which being computed between each pair of particles, will scale as N^2 if naively implemented. Here, three such treatments commonly used to minimize the time consumption of this step are introduced.

1. Verlet list:
   Many potentials are short-ranged in nature or are truncated at a cutoff radius r_c for convenience. Particles whose distance to another particle (say, i) is larger than the cutoff do not contribute to the forces acting on particle i and it is then useful to limit the force calculation to those particle pairs which are actually interacting. Verlet [47] introduced such a method by considering a second cutoff radius r_v larger than r_c. Each particle i has a neighbour list or Verlet list consisting of the particles in a radius r_v from it, as shown in Fig. 3.3. Only these particles are considered in the force calculations, which makes this step scale as N instead of N^2. When a particle in a list moves more than $(r_\mathrm{v} - r_\mathrm{c})/2$ and thus comes in interacting distance with particle i, the lists are updated in order to take the new interaction into account. The update is an order N^2 process, and will dominate the time consumption for very large systems, which makes the overall scaling of the Verlet list algorithm of order N^2.
2. Cell list:
   A force-calculation algorithm which scales as N is the cell list [48], in which the simu-

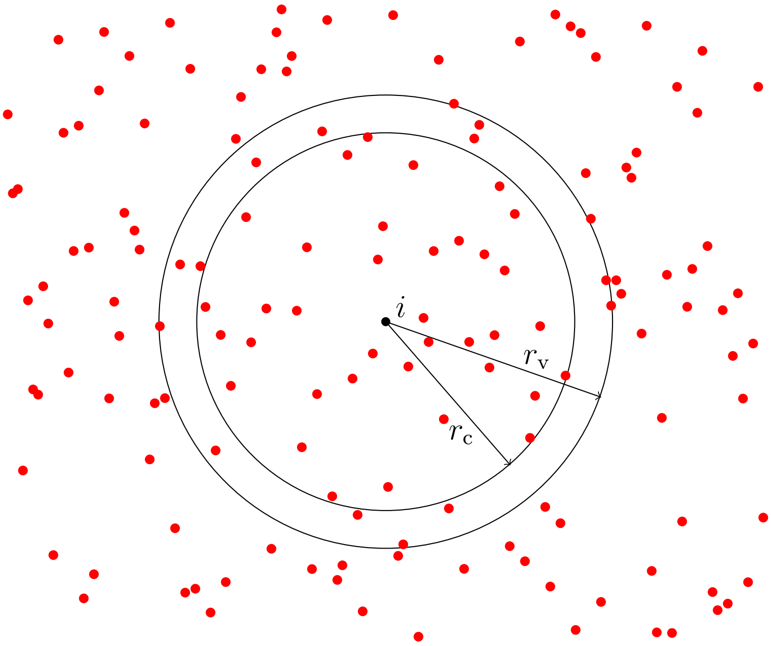

Figure 3.3: A 2D schematic representation of the Verlet list method.

lation box is decomposed into cells of size r_c (or slightly larger) as shown in Fig. 3.4. Instead of storing the particle data particle-wise in one long array, it is done cell-wise, i.e. the information about all the particles in each cell is stored in one array. Each particle interacts only with particles in the same or the nearest neighboring cells. It is only assigning each particle to a cell, which scales as N, that consumes time, making the cell list algorithm an order N algorithm.

3. Combined Verlet-Cell list:
   Besides having many advantages, both of these two methods introduced above also have their disadvantages. The Verlet lists are not efficient enough for today's multi-core, parallel computing architecture. By storing the particle data cell-wise instead of particle-wise, the cell list algorithm is more local and therefore easier to parallelize, yet the neighbourhood of each particle is not restricted to those with which it interacts. Combining these two algorithms puts their advantages together to make a parallelizable force-calculation method with significantly improved efficiency [49]. In the combined Verlet-Cell list algorithm, also called pairwise Verlet list, the domain is again divided into cells of edge length $\geq r_\mathrm{c}$ and the particle data is stored cell-wise. Similar to the cell list method, only the nearest-neighbour cell pairs interact with each other. A local Verlet list is then assigned to each of these pairs; e.g. for the two interacting cells C_α and C_β, the ith row of this local array stores the indices of all the particles in C_β within r_v of the ith particle in C_α.

4. Long-range interactions:
   Long-range interactions, e.g. electrostatics and hydrodynamics, are more difficult to

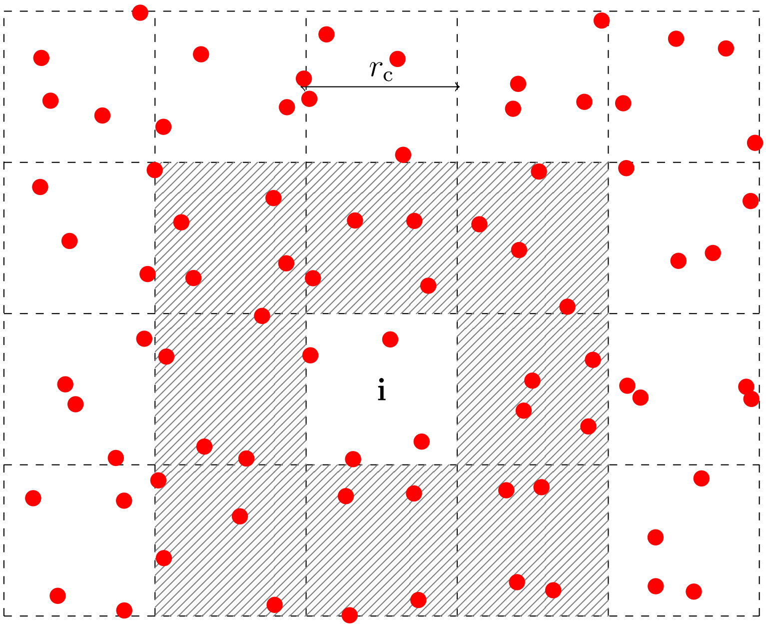

Figure 3.4: Cell list schematic. The simulation domain is decomposed into cells of length $\geq r_c$ and the pair interactions are only calculated for particles in the same (say i) or nearest-neighboring (hatched area) cells.

optimize since they cannot be truncated. There are different methods to deal with such interactions in PBC. Electrostatics and hydrodynamics, the two long-ranged interactions occurring in this thesis, and their respective simulation methods are introduced in sections 3.4 and 3.3.

3.2 Coarse-grained potentials

A thermodynamic system consists of $N \sim 10^{23}$ particles, each having 3 translational degrees of freedom when free to move in 3D. If the particles have complex structures there will be extra rotational and vibrational degrees of freedom as well. The total number of degrees of freedom in a typical macroscopic system is therefore of the order of 10^{24} and considering them all in a computer simulation is rarely feasible. In many cases, experimentally relevant time scales cannot be reached for the experimentally relevant length scales. One should then either be content with much smaller scales or reduce the number of degrees of freedom. In the latter case, referred to as coarse-graining, the “unimportant” details of the system are neglected and their effect is *coarse-grained* into an averaged potential called a force field. On the other hand, the “important” degrees of freedom needed to describe the system accurately are taken into account explicitly. Distinguishing between the important and unimportant details of a system is not always a straightforward task and demands a lot of care.

The systems studied in this thesis are macroscopic ones for which efficient *all-atom* simulations would require unreasonably long computing time even with today’s computational resources. Thus simpler physical models are considered and coarse-grained (CG) simulations are performed. In the following, the force fields used for this purpose are introduced.

3.2.1 Lennard-Jones Potential

In nature particles, no matter how small, have a finite size and do not occupy the same position in space. In order to introduce this steric nature of particles in simulations, a potential needs to act between them to prevent them from overlapping. Neutral particles repel each other at very small distances due to the Pauli exclusion principle and attract each other at larger distances as a result of London dispersion forces. These are included in a very simple mathematical model called the Lennard-Jones (LJ) potential shown in Fig. 3.5:

$$U_{\mathrm{LJ}}(r) = \begin{cases} 4\epsilon_{\mathrm{lj}}\left(\left(\frac{\sigma_{\mathrm{lj}}}{r-r_{\mathrm{off}}}\right)^{12} - \left(\frac{\sigma_{\mathrm{lj}}}{r-r_{\mathrm{off}}}\right)^{6} + c_{\mathrm{shift}}\right), & r_{\mathrm{off}} < r < r_{\mathrm{cut}} + r_{\mathrm{off}} \\ 0, & \text{elsewhere,} \end{cases} \tag{3.18}$$

Here ϵ_{lj} defines the potential strength and the sum of the radii of the interacting particles is determined by $r_{\mathrm{off}} + \sigma_{\mathrm{lj}}$. The potential has a minimum at $r_{\mathrm{min}} = r_{\mathrm{off}} + 2^{1/6}\sigma_{\mathrm{lj}}$ for which $U_{\mathrm{LJ}}(r_{\mathrm{min}}) = -\epsilon_{\mathrm{lj}} + 4\epsilon_{\mathrm{lj}}c_{\mathrm{shift}}$. In order to optimize the force calculation in simulations with PBC as discussed in subsection 3.1.1, the potential can be truncated at r_{cut}. It then needs to be shifted by an appropriate amount c_{shift} in order to maintain potential and force continuity. The special case of $r_{\mathrm{cut}} = 2^{1/6}\sigma_{\mathrm{lj}}$ and $c_{\mathrm{shift}} = 0.25$ corresponds to a purely repulsive interaction called the Weeks-Chandler-Anderson (WCA) potential [50] depicted by the dashed line in Fig. 3.5.

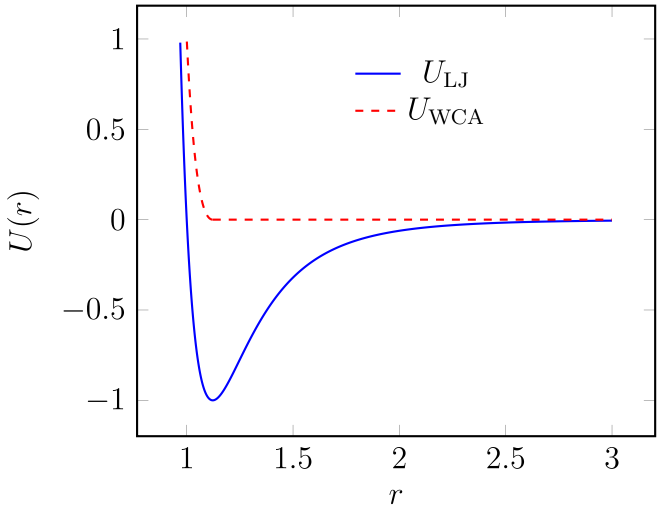

Figure 3.5: (blue line) Lennard-Jones potential U_{LJ}, Eq. 3.18, for $\epsilon_{\mathrm{lj}} = 1$, $\sigma_{\mathrm{lj}} = 1$, $r_{\mathrm{off}} = 0$, and $c_{\mathrm{shift}} = 0$. The WCA potential U_{WCA} with $\epsilon_{\mathrm{lj}} = 1$, $\sigma_{\mathrm{lj}} = 1$ is depicted by the dashed red line for comparison.

3.2.2 Finitely-extensible nonlinear elastic bonds

Some of the simulations in this thesis involve polymers. The commonly used potential to model the bonds between the monomers is the finitely-extensible nonlinear elastic (FENE) bonds [51, 52] (see Fig. 3.6):

$$U_{\mathrm{FENE}}(r) = -\frac{kR_0^2}{2} \ln \left(1 - \left(\frac{r}{R_0}\right)^2\right), \tag{3.19}$$

where k is the stiffness of the bond, R_0 is its maximum extension, and r the distance between the centers of the two interacting monomers. The advantage of the FENE potential to other bonded potentials, such as a harmonic potential $U_{\mathrm{H}}(r) = k_{\mathrm{H}}r^2$, is that it is *finitely extensible*, hence the name. This prevents the polymer from stretching infinitely, as a harmonic bond would do. The FENE potential is shown and compared to the harmonic potential in Fig. 3.6. It is seen that FENE diverges as the distance between the connected beads approaches its maximum value R_0. k and R_0 are typically chosen such that bond-crossing does not occur in CG simulations.

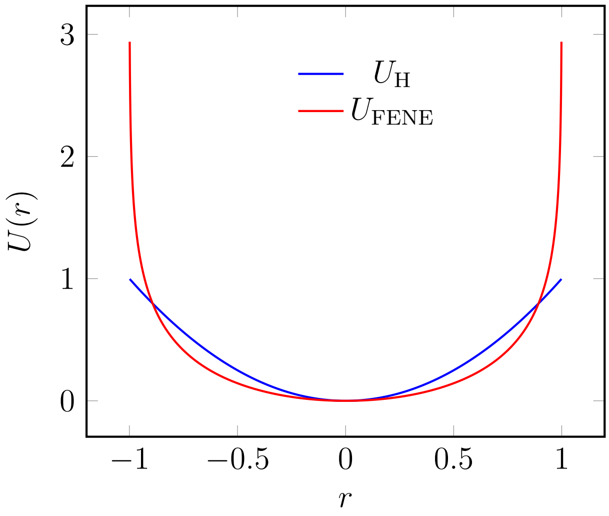

Figure 3.6: (red line) FENE potential U_{FENE} for $k = 1$ and $R_0 = 1$. The blue line shows the harmonic potential $U_{\mathrm{H}} = k_{\mathrm{H}}r^2$ with $k_{\mathrm{H}} = 1$ for comparison.

3.3 Hydrodynamic Interactions and Solvent Models

Fluids are a crucial part of many physical systems ranging from microscopic biological environments all the way up to large scale systems encountered e.g. in meteorology. Most of the processes in the field of soft matter happen in solution, which makes modeling the liquid as solvent crucial. The long-ranged hydrodynamic interactions occurring when a fluid is set to move also have a significant impact on many processes. It is therefore important to understand these effects and to model them in a computer simulation as well. This section introduces the concept of these hydrodynamic interactions, followed by a discussion of the CG solvent models used in this thesis in subsection 3.3.1.

Hydrodynamics is the physics of fluids in motion as well as the forces they exert on relatively moving immersed particles. When a fluid is set to motion locally by a moving particle or

pressure gradient, etc., the local distribution of its constituents is disturbed. This disturbance is then transmitted by the medium, creating a *flow* which propagates through the fluid. Hydrodynamic interactions (HIs) are long-ranged interactions caused by a flow which affect and can be affected by the movement of submerged particles.
Consider a dense Newtonian fluid[1], to which the continuum hypothesis can be applied, i.e. its Knudsen number[2] is small. When such a fluid moves with a speed much smaller than the speed of light, the equations of motion can be described by the Navier-Stokes equation (NS):

$$\rho\left(\frac{\partial\vec{u}}{\partial t}+(\vec{u}\cdot\nabla)\vec{u}\right)=-\vec{\nabla}p+\vec{\nabla}\cdot\mathbb{T}+\vec{f}. \tag{3.20}$$

Here, ρ and $\vec{u}$ are respectively the mass density and the velocity of the fluid, t is the time, p is the hydrostatic pressure, $\mathbb{T}$ is the trace-free stress tensor, and $\vec{f}$ represents body forces per unit volume acting on the fluid (e.g. electrostatic or gravitational forces). The left-hand side of Eq. 3.20 represents the inertia per volume where $(\vec{u}\cdot\vec{\nabla})\vec{u}$ describes the convective acceleration of the fluid. The first two terms on the right-hand side take into account the divergence of stress due to pressure gradient and shear stress, respectively. In the case of incompressible Newtonian flows, which can even be assumed in *compressible* fluids as long as the Mach number[3] is smaller than 0.3 [54], the NS equation reduces to:

$$\rho\left(\frac{\partial\vec{u}}{\partial t}+(\vec{u}\cdot\vec{\nabla})\vec{u}\right)=-\vec{\nabla}p+\eta\nabla^2\vec{u}+\vec{f}, \tag{3.21}$$

where η is the dynamic viscosity.

In many systems, HIs play a significant role and their effect cannot be ignored, and therefore need to be included in MD simulations efficiently. There are many different methods to do so which can be categorized into two main groups. One is the group of particle-based methods where fluid atoms (or molecules) are either considered individually or clustered together such that each particle represents a few constituents. Examples of this category include Dissipative Particle Dynamics (DPD) [55] and Multi-Particle Collision Dynamics (MPCD) [56]. The other category is based on the solution of the discretized NS on a lattice, known as the lattice-Boltzmann (LB) method [57–59].

For systems including mesoscopic particles, there is a separation of length and time scales due to the large difference between the size and relaxation time of the solvent and the solute. As a result, the details of the small and fast solvent particles can be ignored and the fluid can be considered as a hydrodynamic continuum on the scale of the mesoscopic particles. This significantly reduces the number of degrees of freedom and makes it possible to simulate such systems more efficiently. This coarse graining might appear to be a very severe simplification

---

[1] A Newtonian fluid is a liquid for which the strain rate due to an applied shear stress is independent of the shear rate and proportional to the stress, with the constant of proportionality being the viscosity [53].

[2] The Knudsen number is a dimensionless quantity defined as the ratio of the molecular mean free path length to a characteristic length of the system, e.g. radius of a particle in a fluid. The Knudsen number is essentially a measure of how many of its own size will a particle move before colliding with others. The continuum description is improper for systems with Knudsen number equal to or larger than one

[3] Mach number is the ratio of the speed of an object moving in a fluid to the local speed of sound. This dimensionless quantity is a measure of the incompressibility of a flow. For low Mach numbers, the compressibility effects are small and can be ignored.

but it has been shown by MD simulations that the validity of a continuum description of the solvent holds up to very small scales, of the order of a few molecular collisions [59, 60].

Here, I focus on such cases that allow the solvent to be treated as a continuum and discuss in the next subsection only the MD simulation methods used in this thesis. The discussions are kept short for the sake of brevity, the reader is referred to [57, 59] for detailed explanations and derivations on LB and [61, 62] for the implicit solvent model.

3.3.1 Solvent Models

To include the different effects liquids have on a system as solvents, various models with different levels of detail exist. Depending on the system properties and the scope of the problem under study, the solvent constituents may be simulated directly or the fluid can be considered as a continuum with or without long-ranged HIs. Here, two coarse-grained methods employed in this thesis, lattice-Boltzmann and implicit solvent without HIs, are introduced.

The lattice-Boltzmann Method

The lattice-Boltzmann (LB) method can be viewed as a solver for the discretized Navier-Stokes equations (NS), suitable for simulating hydrodynamics on a grid. It is based on the discrete formulation of the Boltzmann equation which, using the Chapman-Enskog expansion, leads to the NS in the limit of low Mach number [58, 63, 64]. The state of the fluid is characterized by the number of particles $n_i(\vec{r}, t)$ $(i = 1, \cdots, b)$ in a volume a^3 at the lattice point r at time t, where a is the grid spacing. A velocity of $\vec{c}_i(a/\tau)$ is associated with n_i, τ being the time step. The vector $\vec{c}_i$ connects each grid point to its ith neighbor. In other words, n_i is the fraction of particles that will move to grid node i towards which $\vec{c}_i$ points. In this work, the D3Q19 implementation of the LB [59] is used which considers 19 velocities in 3 dimensions. In this model the velocity vector can be either $(0, 0, 0)$ or pointing to one of the 18 grid points of the nearest and next-nearest neighboring cells as shown in Fig. 3.7. There are two steps involved in the algorithm; the collision step and the streaming step. In the first one, the populations on the lattice sites, i.e. n_i, are updated locally, according to the scheme discussed below, and in the second step these propagate to the neighboring sites according to their associated velocities $\vec{c}_i$. The mesoscopic hydrodynamic modes are derived from n_i as:

$$\begin{aligned} &\rho(\vec{r}, t) = \textstyle\sum_i n_i(\vec{r}, t) \quad (\textit{mass density}), \\ &\vec{j}(\vec{r}, t) = \textstyle\sum_i n_i(\vec{r}, t)\vec{c}_i \quad (\textit{momentum density}), \\ &\vec{u}(\vec{r}, t) = \vec{j}(\vec{r}, t)/\rho(\vec{r}, t) \quad (\textit{fluid velocity}). \end{aligned} \tag{3.22}$$

The update of the populations in the collision step occurs according to the thermalized lattice-Boltzmann equation:

$$n_i(\vec{r} + \vec{c}_i t, t + \tau) = n_i(\vec{r}, t) + \Delta n_i^{\text{coll}}(\vec{r}, t) + n_i'(\vec{r}, t). \tag{3.23}$$

The collision term can be written as $\Delta n_i^{\text{coll}}(\vec{r}, t) = \sum_{j=1}^{b} \mathcal{L}_{ij}(n_j(\vec{r}, t) - n_j^{\text{eq}}(\rho, \vec{u}))$, where $\mathcal{L}$ is the

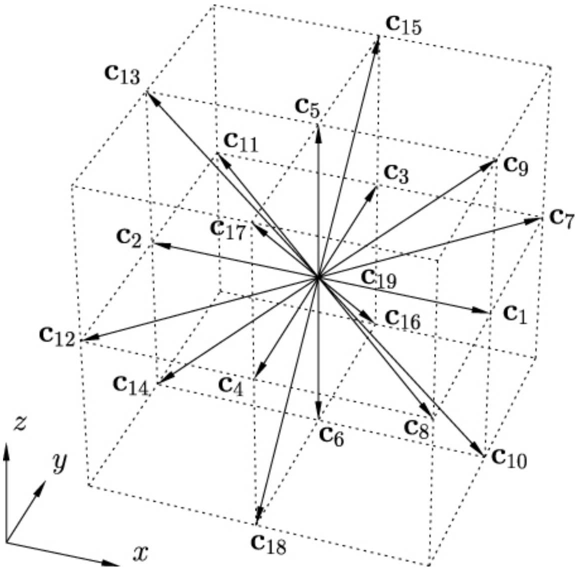

Figure 3.7: A sketch of the D3Q19 lattice geometry showing the 19 discrete LB velocity vectors $\vec{c}_i$. Image taken from [2].

collision operator and drives the velocity distributions towards the local Maxwell-Boltzmann equilibrium distribution $n_j^{\mathrm{eq}}(\rho, \vec{u})$. In general, the choice of the form of the collision operator is free as long as it fulfills the mass and momentum conservation constraint. A simple choice is the well-known Bhatnagar-Gross-Krook collision operator [58, 65], which is a diagonal matrix with $\mathcal{L}_{ii} = \tau/\tau_{\mathrm{r}}$, where τ_{r} is the relaxation time related to the viscosity. A better and more commonly used choice for the collision operator is the multiple-relaxation-time scheme [66] which considers different relaxation times for each velocity mode. In Eq. 3.23, $n_i'(\vec{r}, t)$ is a stochastic term included to model the thermal fluctuations consistent with the fluctuation-dissipation theorem. It is chosen such that the random stress fluctuations are uncorrelated both in time and in space [57, 67]:

$$\langle \sigma'_{\alpha\beta}(\vec{r}, t)\sigma'_{\gamma\delta}(\vec{r'}, t')\rangle = A\delta_{\vec{r}\vec{r'}}\delta_{tt'}(\delta_{\alpha\gamma}\delta_{\beta\delta} + \delta_{\alpha\delta}\delta_{\beta\gamma} - \frac{2}{3}\delta_{\alpha\beta}\delta_{\gamma\delta}). \tag{3.24}$$

Here, $\alpha, \beta, \gamma, \delta = x, y, z$ and the variance A defines the effective temperature of the fluid through $A = 2\eta k_{\mathrm{B}}T\lambda^2/(a^3\tau)$ [58], where λ is the eigenvalue of $\mathcal{L}_{ij}$ belonging to the eigenvector $c_{i\alpha}c_{i\beta}$ $(\alpha \neq \beta)$. The i in say $c_{i\alpha}$ is the number of the velocity mode. For example for D3Q19, $i = 1, .., 19$ as shown in Fig. 3.7.

When there are MD particles in the system, they are coupled dissipatively to the fluid. For that purpose the particles are treated as point particles subject to a Stokes-like dissipative force:

$$\vec{F}_{\mathrm{fl}} = -\zeta_{\mathrm{bare}}[\vec{V} - \vec{u}(\vec{R}, t)] + \vec{f}, \tag{3.25}$$

where $\vec{V}$ is the velocity of the particle and ζ_{bare} is the “bare” friction coefficient. $\vec{f}$ is a random force with zero mean added due to the dissipative nature of the coupling for which the following relation must be satisfied:

$$\langle f_\alpha(t) f_\beta(t')\rangle = \delta(t-t') 2\delta_{\alpha\beta} k_{\mathrm{B}} T \zeta_{\mathrm{bare}}. \tag{3.26}$$

Note that the temperature appearing in Eq. 3.26 is the same as used to thermalize the fluid and hence the coupling also functions as a thermostat. Since the fluid is treated discretely, its velocity $\vec{u}(\vec{R}, t)$ at the position of the MD particle is not known. To calculate it, the velocities $\vec{u}(\vec{r}, t)$ at the grid sites of the primary cell within which the particle is positioned are linearly interpolated (see Fig. 3.8):

$$\vec{u}(\vec{R}, t) = \sum_{\vec{r} \in \mathrm{ng}} \delta_{\vec{r}} \vec{u}(\vec{r}, t), \tag{3.27}$$

where ng in the sum limit denotes the nearest grid points, i.e. those of the considered cell, and (see Fig. 3.8).

$$\begin{aligned} \delta_{(0,0,0)} &= (1-\tfrac{\Delta x}{a})(1-\tfrac{\Delta y}{a})(1-\tfrac{\Delta z}{a}), \\ \delta_{(1,0,0)} &= \tfrac{\Delta x}{a}(1-\tfrac{\Delta y}{a})(1-\tfrac{\Delta z}{a}), \\ &\vdots \end{aligned} \tag{3.28}$$

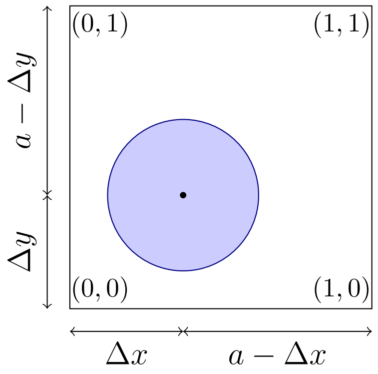

Figure 3.8: 2D schematic of a particle within an LB cell. The fluid velocity at the position of the particle is obtained by interpolating the velocities at the grid points, see equations 3.27 and 3.28.

In order to get the correct hydrodynamic behavior, the total momentum needs to be conserved, i.e. the opposite force has to be applied to the fluid in the cell where the MD particle resides. This is done via a momentum density transfer per MD time step Δt:

$$-\frac{\vec{F}_{\mathrm{fl}}}{a^3} = \frac{\Delta \vec{j}}{\Delta t} = \sum_{i, \vec{r} \in ng} \Delta n_i(\vec{r}, t) \vec{c}_i \frac{\mu}{a^2 \tau \Delta t}. \tag{3.29}$$

Here, μ is the mass of the fluid particles and $\Delta n_i(\vec{r}, t)$ is the population change at grid point $\vec{r}$ due to the existence of the particle. The other quantity which needs to be conserved is mass:

$$\sum_{i, \vec{r} \in ng} \Delta n_i(\vec{r}, t) = 0. \tag{3.30}$$

This leads to the fact that ρ would not change by this local momentum transfer while $\vec{j} \to \vec{j} + \delta_{\vec{r}}\Delta\vec{j}$.

It needs to be emphasized that the proportionality constant used in Eq. 3.25 is the *bare* friction coefficient. According to Stokes law, for a sphere this would be $\zeta_{\text{bare}} = 6\pi\eta R$ with R being the radius of the particle. In the LB algorithm, MD particles are considered as point particles and the velocity of the fluid at the position of each is an interpolation of the fluid velocities at the nearest grid points. As shown below, this discretization introduces an *effective* Stokes radius to the particle. Consider a particle being dragged at constant velocity by a constant force. Then according to Eq. 3.25 (ignoring the random force $\vec{f}$ which averages to zero) its velocity is given by:

$$\vec{V} = \frac{1}{\zeta_{\text{bare}}}\vec{F} + \vec{u} \tag{3.31}$$

On the other hand, $\vec{u}$ can be approximated by $\vec{u}(\vec{r}) = \vec{F} \cdot \mathbb{J}(\vec{r})$ where the Oseen tensor $\mathbb{J}$ is given by:

$$\mathbb{J}(\vec{r}) = \frac{1}{8\pi\eta r}\left(\mathbb{I} + \frac{\vec{r}\vec{r}}{r^2}\right). \tag{3.32}$$

Taking the center of the spherical particle to be roughly a distance a from the considered grid points, this results in $\vec{u} = \vec{F}/(g\eta a)$. g is a numerical constant and reflects the geometry of the lattice and the interpolation procedure. Together with Eq. 3.31, this results in:

$$\vec{V} = \left(\frac{1}{\zeta_{\text{bare}}} + \frac{1}{g\eta a}\right)\vec{F} \equiv \frac{1}{\zeta_{\text{eff}}}\vec{F}. \tag{3.33}$$

For the cubic lattice used in the LB implementation employed here, g has been found to be $g \approx 25$ [58]. Eq. 3.33 reveals the fact that ζ_{bare} actually has no physical meaning, it is merely a coupling constant. It is the effective friction coefficient ζ_{eff} which determines the mobility of the MD particles. Since this quantity contains the grid spacing, it is clear that besides determining the accuracy with which the NS is solved, a also influences the effective hydrodynamic radius of the solute particles.

Implicit Solvent Excluding HI

When the hydrodynamic effects of the solvent are not relevant for the description of the system's behavior, the solvent can be simulated implicitly [68, 69] without taking into account the HI. Implicit solvent models also disregard effects such as liquid layering or the conformation of solvent molecule around an object. In this approach, the solvent is considered as a continuum manifesting itself through its impact on the forces acting between (charged) particles via a relative dielectric constant ε_{r} and viscosity η. The electrostatic interaction between two charges q_1 and q_2 is then given by $U(r) = l_{\text{B}} k_{\text{B}} T q_1 q_2 / r$ where $l_{\text{B}} = e^2/(4\pi\varepsilon_0\varepsilon_{\text{r}} k_{\text{B}} T)$ is the Bjerrum length with e being the elementary charge and ε_0 is the vacuum permittivity ($\varepsilon_0 \simeq 8.85 \times 10^{-12}$ F/m). The drag force exerted by the fluid on the particle enters the simulation through a thermostat used to keep the temperature constant. One of the commonly used thermostats is the Langevin thermostat, which works by adding two extra forces $\vec{F}_{\text{d}}$ and $\vec{F}_{\text{r}}$ to the total force acting on the particles. Instead of the Newtonian equation of motion, the Langevin equation

$m\vec{a}(t) = -\vec{\nabla}\Phi - \Gamma\vec{V}(t) + \vec{F}_{\mathrm{r}}(t)$ is then solved, where m is the mass of the particle and $\vec{a}$ its acceleration. The first term in this equation is the force due to interactions with other particles or externally applied forces. $\vec{F}_{\mathrm{d}} = -\Gamma\vec{V}$ is the viscous drag force resulting from the resistance of the fluid to particle's motion, with Γ being the friction coefficient. Γ depends on the shape of the particle and some properties of the solvent such as its viscosity. For a spherical particle with radius R in a Newtonian fluid with dynamic viscosity η, $\Gamma = 6\pi\eta R$. Using the hydrodynamic radius R_{h}, defined as the radius of an equivalent sphere having the same drag coefficient, the drag force can be written as $F_{\mathrm{d}} = -6\pi\eta R_{\mathrm{h}}$ for any particle.

In order to get the correct average velocity and average temperature, a source of energy needs to be considered in addition to the drag force, which dissipates energy. This energy is maintained by the collisions between the particle and the molecules of the heat bath, i.e. the solvent. Due to the random nature of these collisions, the energy source term is taken to be a random force. Einstein [70, 71] explained that these random collisions, which lead to the Brownian motion of the particle, are also the cause of the drag exerted on the particle when pulled through a fluid. This is a manifestation of the fluctuation-dissipation theorem. Therefore, $\vec{F}_{\mathrm{d}}$ and $\vec{F}_{\mathrm{r}}$ are related to each other. Writing the random force as $\vec{F}_{\mathrm{r}} = \vec{\zeta}_i(t)$, thus it can be shown that

$$\langle\vec{\zeta}_i(t)\rangle = \vec{0} \quad \text{and} \quad \langle\vec{\zeta}_i(t).\vec{\zeta}_j(t')\rangle = 6\Gamma k_{\mathrm{B}}T\delta_{ij}\delta(t-t'). \tag{3.34}$$

Similar to the LB random force 3.26, $\vec{\zeta}_i(t)$ is a random distribution, usually chosen to be Gaussian, leading to the correct Maxwell-Boltzmann velocity distribution.

Note that the Langevin thermostat does not conserve momentum and energy. The implicit solvent model is suitable for analyzing static thermodynamic properties such as ions distribution [61, 62], structural changes induced by an external field, or energy of solvation.

3.4 Electrostatics

Since this thesis deals with charged particles in aqueous solutions, it is necessary to introduce the electrostatic methods employed in the simulations, and the theories used to compare their results to. In this section, I first outline the basic concepts of calculating long-ranged electrostatic interactions in a simulation. Subsections 3.4.1 and 3.4.2 deal with the two computational algorithms used in the simulations and subsection 3.4.3 gives a review on the theoretical background of charged surfaces in contact with an electrolyte solution. All the discussions are very brief and without explicit proofs. The reader is referred to [48, 72–77] for detailed discussions.

The electrostatic potential at position $\vec{r}$ due to a system consisting of N point charges q_i $(i = 1 \cdots N)$ respectively at positions $\vec{r}_i$ is given by Coulomb's law:

$$\phi(\vec{r}) = \frac{1}{4\pi\varepsilon_0\varepsilon_{\mathrm{r}}} \sum_{i=1}^{N} \frac{q_i}{|\vec{r} - \vec{r}_i|}. \tag{3.35}$$

The potential decays as $1/r$ and therefore, electrostatic interactions are long-ranged. For a system with PBC, the total electrostatic energy is an infinite sum:

$$E = \frac{1}{2} \sum_{\hat{m}\in\mathbb{Z}^3}^{\infty} {\sum_{i,j=1}^{N}}' \frac{q_i q_j}{|\vec{r}_i - \vec{r}_j + \hat{m}L|}, \tag{3.36}$$

with $\hat{m}$ counting the periodic images and L being the box length. The prime on the second sum indicates that only particles i and j with $\vec{r}_i \neq \vec{r}_j$ for $\hat{m} = 0$ are taken into account in order to avoid self-energies. The $1/r$ nature of this potential and the fact that it is only conditionally convergent (i.e. the result depends on the order of the terms in the sum), make it impossible to calculate Eq. 3.36 exactly in PBC. Applying a cutoff to a long-ranged interaction has its own draw backs, too short a cutoff would create a large error whereas a long enough cutoff would be computationally very demanding. Besides, the value of the potential would depend on the cutoff radius. Another intrinsic difficulty with this potential is that it varies strongly at small distances and decays slowly at large distances. Treated separately, each of these parts would be much easier to deal with. The fast varying short-ranged part could be cut off and the slowly varying periodic long-ranged part could be represented by its first few Fourier series accurately enough. It is the combination of these two behaviours at short and large distances which causes severe problems. Working on ionic crystals (the Madelung problem), Ewald [73, 78] developed a method based on a simple and ingenious trick to solve the problem of long-ranged interactions in periodic systems and improve the efficiency of the computation; he split the potential into two parts using a trivial identity:

$$\frac{1}{r} = \frac{f(r)}{r} + \frac{1 - f(r)}{r}. \tag{3.37}$$

$f(r)$ should be chosen such that the two parts of Eq. 3.37 can be solved separately:

- $\frac{f(r)}{r}$ should have a very small value, if not zero, beyond a cutoff $r_{\max}$. This allows the summation to be safely terminated after the cutoff.
- $\frac{1-f(r)}{r}$ should vary slowly over the whole range. Its Fourier transformation can then be represented by only a few $\vec{k}$-vectors where $|\vec{k}| \leq k_{\max}$.

The traditional choice for $f(r)$ is $f(r) = \operatorname{erfc}(\alpha r)$ [73, 79–81] where $\operatorname{erfc}(r)$ is the complimentary error function. The Ewald splitting parameter α is an inverse length which tunes the relative weights between the real and reciprocal spaces. Decomposed in this manner, the sum converges much faster and the complexity of the computation reduces to $\mathcal{O}(N^2)$ or even $\mathcal{O}(N^{3/2})$ when the parameters are optimized [73, 82]. Ewald summation works very well for small systems with hundreds of particles, but it is still computationally too expensive for most of the physical systems of interest, which include thousands to millions of charged particles. The most time-consuming part of it is the Fourier transformations; i.e. replacing it by a faster method increases the calculation speed appreciably. This idea is exploited by the more advanced family of the so-called mesh-based techniques such as the Particle-Mesh Ewald [83, 84] (PME) method, the Smooth Particle-Mesh Ewald (SPME) method [74, 85], or Particle-Particle Particle-Mesh (P^{3}M) method [48, 74], which reduce the computation time to scale with $N \log N$ by replacing the Fourier transform by a fast Fourier transform (FFT). This requires the space and charge to be discretized which is done by mapping the charges onto a mesh. In doing so, these methods gain speed at the cost of losing resolution as the mapping smears out the (point) charges onto the grid points. The representation of a point charge is not accurate anymore, but it can be interpreted as the accurate representation of a "cloud" of charge of the size of the grid spacing a [72]. P^{3}M is the most convenient mesh-based method [76, 86] and is widely used to compute electrostatic interactions in periodic systems. It is also used in this work and is introduced briefly below.

3.4.1 Particle-Particle Particle-Mesh (P^{3}M) method

In mesh-based methods charges are mapped onto a mesh via a *charge assigning function* W:

$$\rho_{\mathrm{M}}(\vec{r}_p) = \frac{1}{a^3}\sum_{i=1}^{N} q_i W(\vec{r}_p - \vec{r}_i), \tag{3.38}$$

with $\vec{r}_p$ being the mesh point position. In the case of P^{3}M algorithm, a cardinal B-spline of order P is chosen for W [73, 87], where P determines the number of grid points per dimension over which a point charge is distributed. Taking advantage of the FFT, solving the Poisson equation for this discrete charge distribution is a relatively straightforward task. The Laplace operator reduces to a simple multiplication by the wavenumber k in Fourier space and the Green's function takes on the simple form $4\pi/k^2$. The Green's function is further adjusted to minimize the deviation of the discrete solution from the continuous one. The forces are next calculated from the mesh-based potential via either of the following differentiation methods [74, 76]: *i*) using finite differences in real space, *ii*) using the exact gradient of the assignment function in real space, or *iii*) multiplying the potential by $i\vec{k}$ in Fourier space. In the last method, known as the $i\vec{k}$-differentiation or force-interpolation scheme [74], the field $\vec{E}(\vec{r}_p)$ is calculated at each mesh point and then interpolated back to the particle position:

$$\vec{F}_i = q_i \sum_{\vec{r}_p \in \mathbb{M}} \vec{E}(\vec{r}_p) W(\vec{r}_i - \vec{r}_p). \tag{3.39}$$

In this equation, the summation is over the complete mesh $\mathbb{M}$. P^{3}M is relatively easy to implement and can be efficiently parallelized. Analytical estimates exist for the error arising from the discretization [77] allowing one to quickly choose parameters for a desired level of accuracy.

3.4.2 Electrostatic Layer Correction (ELC) Method

The method introduced in the previous part relies on the periodicity of the system in all three dimensions. This is not applicable when the system under study is finite in one or two directions, e.g. in micro- and nanofluidic devices, or thin films. Methods based on the MMM algorithm [73, 88, 89], called MMM1D [90] and MMM2D [75, 91], exist for systems with partial periodicity, but they are only efficient for small systems with a few hundred particles [73]. The common way to handle the electrostatic interactions in a large system which is not fully periodic is to use a 3D method and place a large gap between the images in the non-periodic directions where there are no particles. Until recently the error due to this approach was not estimated and had to be found out by trial and error. Arnold *et al.*

derived exact calculations of the error due to the unwanted periodicities [75, 92] which can be subtracted from the energy. This method is called the electrostatic layer correction (ELC) and allows for significant reduction of the gap size. Calculating this correction term scales linearly with the number of particles and it is therefore the 3D method used in combination with ELC which determines the overall scaling, e.g. $N \log N$ in case of P^{3}M. Also the precision of ELC can be tuned to the same value used in the 3D method. Since partially periodic systems are encountered in the first part of this thesis, below I give a very brief explanation of this method. A full discussion can be found in [75, 91, 93].

To understand the idea behind ELC, assume we have a system of charges in a box of size $\lambda_x \times \lambda_y \times h$, which is confined in the z direction, where h is the maximum distance between two charges in the confined direction. This partially periodic system is placed in a fully periodic box with edge lengths $\lambda_x, \lambda_y, \lambda_z$ where $\lambda_z \gg h$, i.e. large gaps of size $\delta_\mathrm{g} = \lambda_z - h$ separate the system replicas in the z direction. Now consider a charge q_j in the original cell together with its periodic images in the $x - y$ plane. The nth *undesired* replica of these charges at a distance $n\lambda_z$ far away can be viewed as a homogeneously charged sheet with charge density $\sigma_j = q_j/(\lambda_x\lambda_y)$ which has a potential $\phi_j = 2\pi\sigma_j|z|$. Due to the overall charge neutrality of the system (a prerequisite for a finite potential), the energy of interaction between an original charge q_i and all symmetric pairs of such image layers at $\pm n\lambda_z$ sums up to zero. This fact can be exploited to calculate the exact electrostatic energy of a slab-like system. In theory, the only error due to this method arises from approximating the discrete charge distributions as continuous charge slab. The accuracy of this assumption becomes better with increasing distance from q_i. In practice, however, there are other sources of error [73, 94]. Eq. 3.36 is a conditionally convergent sum and its value is well-defined only when the precise order in which the terms, i.e. the simulation boxes, are added is specified. Conventionally, an approximately spherical summation is considered (see [95–97] and Fig. 8 in [73]). A “slab-wise” summation, however, serves the purpose of ELC better [94] (also see Fig. 8 in [73]) and can be obtained from the spherical result as shown by Smith [98]. The total energy of a fully periodic system can then be written as [73]:

$$E = E_\mathrm{s} + E_\mathrm{c} + E_\mathrm{lc}, \tag{3.40}$$

where E_s is the spherical standard 3D Coulomb summation, E_c is the slab-wise summation correction, and E_lc is the contribution of the image layers. The sum of the two first terms corresponds to the 3D method mentioned above which uses a large gap between the images in the non-periodic direction. By adding the third term, Arnold *et al.* [75, 92] created the much more efficient ELC method where a much smaller gap can be used. They derived an exact expression for E_lc with a linear computation time with respect to N. Still, like any other method, ELC has also some disadvantages; namely, the associated error of considering homogeneously charged layers is position-dependent and can only be estimated numerically. Due to symmetry arguments, for a system with uniform charge distribution no error is incorporated in the energy of the particles in the middle of a slab whereas that of the surface particles is subject to the highest error. The appropriate gap size for the system under investigation can be found by using successively larger gaps and choosing a reasonable one for which the forces do not change much when enlarging it further.

3.4.3 Theoretical Background: Poisson-Boltzmann Equation

In this subsection I give a short survey of the existing theories for the electrostatics of charged particles and surfaces in an electrolyte solution used in this thesis for comparison with simulation results.

When a charged solid surface is put into contact with an ionic solution, it changes the equilibrium distribution of the ions. A so-called electric double layer (EDL) forms at the surface: the first layer, known as the Stern layer, consists of counterions, i.e. ions having a charge of opposite sign to that of the surface. The ions in this layer are considered to be strongly attached to the surface, due to either electrostatic attraction or specific chemical adsorption, and not free to move. This layer partially screens the electrostatic field of the surface, causing the ions further away from it to interact less strongly with the object. The ions in the next layer therefore move more freely under the influence of thermal motion and distribute more or less diffusively. Hence the second layer is usually referred to as the diffuse layer. This is a simplified picture of the EDL and a more detailed description is sometimes necessary to describe the structure of the ionic cloud surrounding a charged surface [99–101], but it suffices for the purposes of this thesis.

Like any other charged system, to find the distribution of the ions in the EDL the Poisson equation needs to be solved:

$$\nabla^2\phi(\vec{r}) = -\rho(\vec{r})/\varepsilon, \tag{3.41}$$

in which $\rho(\vec{r})$ is the charge density and the permittivity of the medium $\varepsilon = \varepsilon_0\varepsilon_{\mathrm{r}}$ is considered to be constant. The mutual dependency of the potential and charge distribution renders this nonlinear second-order differential equation far from straight forward to solve. In many systems this can be simplified by considering a Boltzmann distribution for the ions:

$$c_i(\vec{r}) = c_i^0 \exp\left(\frac{-z_i e\phi(\vec{r})}{k_{\mathrm{B}}T}\right), \tag{3.42}$$

where $c_i(\vec{r})$ is the local molar concentration of ion species i with valency z_i. c_i^0 is the ith ion molar concentration where $\phi(\vec{r}) \equiv 0$, which is usually the bulk. This is a mean-field approximation which disregards the correlations between the ions and treats them as point charges. The charge density in Eq. 3.41 can then be written as:

$$\rho(\vec{r}) = F\sum_{i=1}^{N} z_i c_i(\vec{r}) = F\sum_{i=1}^{N} z_i c_i^0 \exp\left(\frac{-z_i e\phi(\vec{r})}{k_{\mathrm{B}}T}\right), \tag{3.43}$$

where $F = eN_{\mathrm{A}} \simeq 9.65\times10^4$ C/mol is the Faraday constant. Inserting Eq. 3.43 into Eq. 3.41 yields the well-known Poisson-Boltzmann equation (PBE):

$$\nabla^2\phi(\vec{r}) = -\frac{F}{\varepsilon}\sum_i z_i c_i^0 \exp\left(-\frac{z_i e\phi(\vec{r})}{k_{\mathrm{B}}T}\right) \tag{3.44}$$

For a symmetric $z - z$ electrolyte, consisting of two ion species with $z_1 = -z_2 \equiv z$, PBE reduces to:

$$\nabla^2\phi(\vec{r}) = \frac{k_{\mathrm{B}}T}{ze}\kappa^2 \sinh\left(\frac{ze\phi}{k_{\mathrm{B}}T}\right). \tag{3.45}$$

where $\kappa = \lambda_{\mathrm{D}}^{-1}$, the inverse Debye length λ_{D}, is defined as:

$$\kappa = \left(\frac{N_{\mathrm{A}} \sum_i (z_i e)^2 c_i^0}{\varepsilon k_{\mathrm{B}} T}\right)^{1/2} = \sqrt{4\pi l_{\mathrm{B}} N_{\mathrm{A}} \sum_i z_i^2 c_i^0}. \tag{3.46}$$

Defining the dimensionless potential $\psi \equiv e\phi/(k_{\mathrm{B}}T)$, Eq. 3.45 reduces to:

$$\nabla^2 \psi(\vec{r}) = \frac{\kappa^2}{z} \sinh(z\psi(\vec{r})). \tag{3.47}$$

Eq. 3.45 (or equivalently Eq. 3.47) is known as the Debye-Hückel (DH) theory in case of $z = 1$ [102]. When $ze\phi \ll k_{\mathrm{B}}T$, i.e. high temperatures or low surface potentials, Eq. 3.47 (or equivalently Eq. 3.45) can be linearized using the Taylor expansion $\sinh(x) \approx x$:

$$\nabla^2 \psi(\vec{r}) \approx \kappa^2 \psi(\vec{r}). \tag{3.48}$$

An example can help make the physical meaning of the Debye length more clear; in case of a plane (e.g. an electrode) with reduced surface potential ψ_0, the solution to Eq. 3.48 is $\psi(y) = \psi_0 \exp(-y/\lambda_{\mathrm{D}})$ where y is the vertical distance from the surface. It is seen that the potential decays exponentially with distance, where λ_{D} is the characteristic length scale. The general solution to Eq. 3.48 for a spherical particle has the form:

$$\psi(r) = A\frac{\exp(-\kappa r)}{r} + B\frac{\exp(\kappa r)}{r}. \tag{3.49}$$

$B = 0$ since otherwise the potential becomes infinite as $r \to \infty$, so only A remains to be determined. When the size of the particle can be ignored, the potential is that of a point charge Q at small distances where there are no other ions, i.e. $\psi(r \to 0) = l_{\mathrm{B}}Q/r$. At such small distances $\exp(-\kappa r) \cong 1$ and $A = l_{\mathrm{B}}Q$, so the potential is:

$$\psi(r) = l_{\mathrm{B}}Q\frac{e^{-\kappa r}}{r} = l_{\mathrm{B}}\frac{Q}{r} - l_{\mathrm{B}}\frac{Q\left(1 - e^{-\kappa r}\right)}{r}. \tag{3.50}$$

The first term on the right-hand side of this equation is the contribution of a point charge, and the second term that of the surrounding ions. When the considered ion has a finite size R, the potential outside the sphere is again $\psi_{\mathrm{out}}(r) = A\exp(-\kappa r)/r$, while the potential inside is like that of a point charge $\psi_{\mathrm{in}}(r) = l_{\mathrm{B}}^{\mathrm{in}}Q/r + C$. The constants A and C can be found from continuity conditions at $r = R$ to be $A = l_{\mathrm{B}}Q\exp(\kappa R)/(1+\kappa R)$ and $B = -l_{\mathrm{B}}^{\mathrm{in}}Q\kappa/(1+\kappa R)$. Thus, the linear approximation of the potential outside a spherical particle in an electrolyte is:

$$\psi(r > R) = l_{\mathrm{B}}Q\frac{e^{\kappa R}}{1+\kappa R}\frac{e^{-\kappa r}}{r}. \tag{3.51}$$

Analytical solutions of the *nonlinear* PBE, Eq. 3.44 (or Eq. 3.47), exist only for a few limited cases, for example, a flat charged surface with uniform charge density σ_{s}. Using the Cartesian coordinates system and assuming that the charged plate is located at the $y = 0$ plane, Eq. 3.47 reads:

$$\frac{\mathrm{d}^2\psi}{\mathrm{d}y^2} = \frac{\kappa^2}{z}\sinh\left(z\psi(y)\right). \tag{3.52}$$

Using Neumann boundary condition $\psi'(\infty) = 0$, the Dirichlet boundary condition $\psi(\infty) = 0$, and the identities:

$$\frac{\mathrm{d}}{\mathrm{d}y}\left(\frac{\mathrm{d}f}{\mathrm{d}y}\right)^2 = 2\frac{\mathrm{d}^2 f}{\mathrm{d}y^2}\frac{\mathrm{d}f}{\mathrm{d}y}, \quad \text{and} \quad \cosh(x) - 1 = 2\sinh^2(x/2), \tag{3.53}$$

it follows from Eq. 3.52 that:

$$\left(\frac{\mathrm{d}\psi}{\mathrm{d}y}\right)^2 = \frac{4\kappa^2}{z}\sinh\left(\frac{z\psi}{2}\right), \tag{3.54}$$

for a $z - z$ electrolyte. Taking the Dirichlet boundary condition for ψ at the surface to be $\psi(0) = \psi_0$, the solution of Eq. 3.54, known as the Gouy-Chapman equation (GC) [103, 104], is obtained after some algebraic calculations as:

$$\psi(y) = \frac{2}{z}\ln\left[\frac{1 + \tanh(z\psi_0/4)\exp(-\kappa y)}{1 - \tanh(z\psi_0/4)\exp(-\kappa y)}\right], \tag{3.55}$$

The total charge neutrality of the system demands that the charges on the surface and in the EDL sum up to zero, therefore:

$$\sigma_\mathrm{s} = -\int_0^\infty \rho(y)\mathrm{d}y = \frac{\varepsilon k_\mathrm{B}T}{e}\int_0^\infty \frac{\mathrm{d}^2\psi}{\mathrm{d}y^2}\mathrm{d}y = -\varepsilon\frac{\mathrm{d}\psi}{\mathrm{d}y}\Big|_{y=0}. \tag{3.56}$$

Replacing Eq. 3.54 in the last term on the right-hand side, the surface charge density can be related to the surface potential via the Grahame equation [105]:

$$\sigma_\mathrm{s} = \frac{2\kappa\varepsilon k_\mathrm{B}T}{ze}\sinh\left(\frac{z\psi_0}{2}\right). \tag{3.57}$$

This relation is useful in cases where only σ_s is known (e.g. from titration experiments) for the surface.

In Fig. 3.9, the solution to the linearized PB, Eq. 3.48, in planar geometry is compared to Eq. 3.55 for two surfaces having different surface potentials in the presence of monovalent salt with $\kappa = 1$. For $\psi_0 = 1$ (blue curves) the two results are almost identical, whereas for $\psi_0 = 10$ (red curves) the difference is significant.

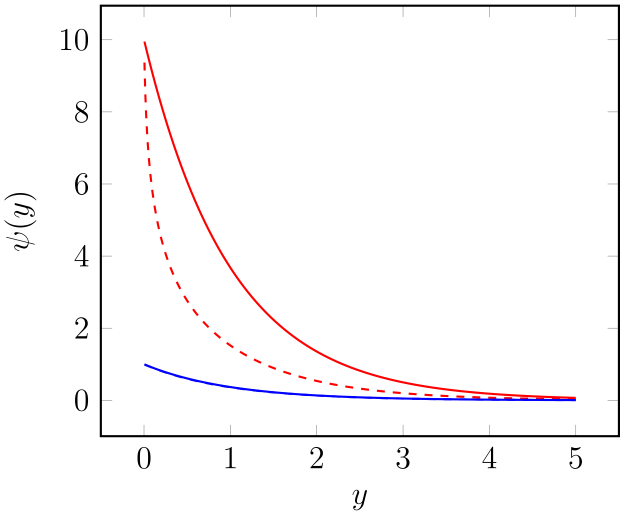

Figure 3.9: The reduced electric potential as a function of the perpendicular distance to the surface. The dashed lines are the solutions to the linearized PB, Eq. 3.48 in planar geometry, and the solid lines show the results of Eq. 3.55. The red lines are for $\psi_0 = 10$ whereas the blue lines are for $\psi_0 = 1$. In both cases $z = 1$ and $\kappa = 1$. The effects of the nonlinearity in the Poisson-Boltzmann is more significant when the surface potential is large.

3.5 Electrophoresis

As the name suggests, electrophoresis, *electro+phoresis* (Greek for being carried), is the motion of a charged particle in a medium (usually a fluid) as a result of an applied electric field. The dependence of the electric force on the charge, and the friction force on the particle size, makes electrophoresis a very useful tool for characterizing particles and one of the main separation techniques. Different types of electrophoresis (e.g. capillary, gel, free-flow, or end-labeled free-solution electrophoresis) can be used to separate different types of molecules based on size or charge. Perhaps the most interesting example is the separation of DNA fragments with different lengths, which was crucial in sequencing the entire human genome [18, 19]. Another important application of electrophoresis is to extract information about the value and distribution of a particle's charge [106–108]. Electrophoresis can be performed on different particles, from single ions and small molecules, to macromolecules such as DNA and proteins. Here, I focus on the electrophoresis of colloids, particles of size $\text{nm} - \mu\text{m}$, in *free* solutions, i.e. the supporting medium only consists of an electrolyte and no gels are involved.

In this section, first the theoretical principles of electrophoresis and the governing electrokinetic equations are introduced. In Sec. 3.5.2, the most commonly used numerical method for solving the electrokinetic equations for spherical particles, which is also employed in parts of this thesis, is discussed. As will seen later, even in the case of numerical solutions, approximations have to be made and tricks need to be used in order to simplify the problem to a level where it is solvable. After that, the modified electrokinetic equations and the common numerical method of solving them for *soft particles* encountered in the second part of this thesis are discussed.

3.5.1 Electrokinetic equations

When a charged particle immersed in a fluid is subject to a uniform applied electric field $\vec{E}$, it moves in a process termed electrophoresis as illustrated in Fig. 3.10. The medium resists the particle's motion by exerting a drag force $\vec{F}_\mathrm{d}$. Usually, the particle is surrounded by counterions and in an electrolyte solution, an EDL will form around it as introduced in subsection 3.4.3. The counterions in the EDL also move under the influence of the electric field, dragging the fluid along with them. This generates an *electro-osmotic flow* (EOF) in the fluid, the velocity of which is the counterpart of the electrophoretic velocity of the particle. Since the counterions have a charge opposite to that of the particle, they move in the opposite direction and thus exert an extra hydrodynamic friction force on the particle, mediated by the surrounding solvent. This force is known as the retardation force $\vec{F}_\mathrm{rt}$.

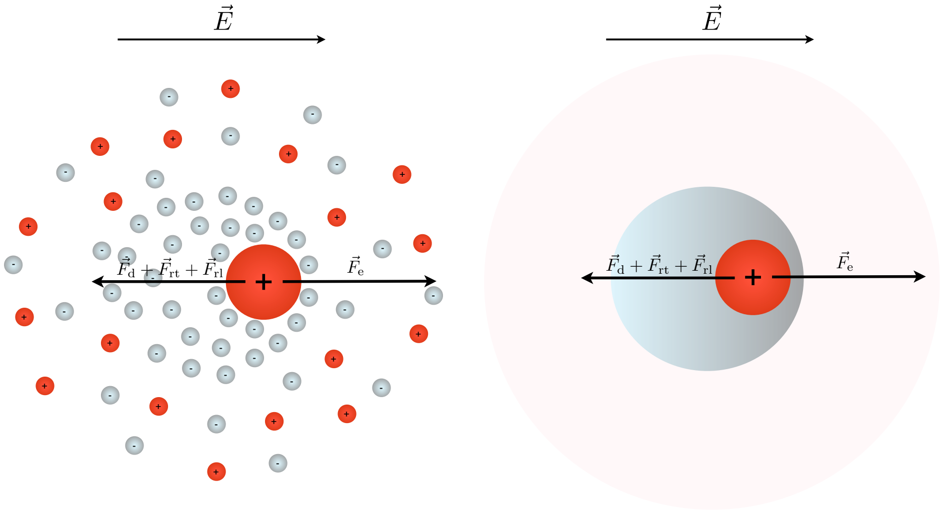

Figure 3.10: A sketch of the electrophoresis of a positively charged colloid (large red sphere). On the left-hand side the ions are depicted explicitly, the negative ones shown in gray and the positive ones shown in red, while the equivalent mean-field implicit ion approach is illustrated on the right-hand side. In the steady state, the electric force $\vec{F}_\mathrm{e}$ exerted on the colloid is canceled by the sum of the drag force $\vec{F}_\mathrm{d}$, the retardation force $\vec{F}_\mathrm{rt}$, and the relaxation force $\vec{F}_\mathrm{rl}$.

The concurrent action of the applied field and that of the particle motion deforms the counterion cloud, creating a dipole which causes an electric retarding force to act on the particle called the relaxation force $\vec{F}_\mathrm{rl}$. The retardation and relaxation forces are coupled; the asymmetry of the counterions cloud affects the retardation force, and the fluid's velocity distribution needs to be explicitly taken into account in the calculation of ion densities leading to relaxation force. In the steady state, the net force acting on the particle is zero and it acquires a drift speed v_d. At low field strengths, v_d is linearly proportional to the strength of the applied field $|\vec{E}| \equiv E$ and the proportionality constant is defined as the electrophoretic mobility:

$$\mu = \frac{v_\mathrm{d}}{E} \tag{3.58}$$

μ is the main quantity of interest in electrophoresis and also the one measured in experiments. It is related to ζ, the potential drop at the shear plane (introduced below) with respect to the bulk, and hence to the charge density of the object. When the fluid adjacent to a surface flows tangentially as a result of electrical forces, or shear mechanical forces, or *etc.*, a thin layer, referred to as the Stern layer, is shown to adhere to the surface and become stagnant [100, 109]. No hydrodynamic flow can develop within this layer and the fluid starts to shear beyond it. The imaginary surface separating this stagnant layer from the mobile part of the fluid is referred to as the *shear* or *slip* plane. Information about the value and distribution of the particle's charge, often unknown *a priori*, can be extracted by measuring μ and converting it to ζ. As will become clear in the course of this section, the conversion from μ to ζ, or vice versa, is not always straight forward and needs a theory which takes into account all the important properties of the system.

In order to calculate the electrophoretic mobility theoretically, a set of coupled nonlinear differential equations, referred to as the electrokinetic (EK) equations, needs to be solved. They describe the motion of the fluid as well as that of the particle and the ions. In the following, the origin of the co-moving coordinate system is fixed on the particle. The force balance in the liquid can be described via the NS equations (Eq. 3.20), as introduced in Sec. 3.3. In the limit of low Reynolds numbers[4], the convective accelerations can be neglected and the NS reduces to Stokes equation which in the steady state ($\partial\vec{u}/\partial t = \vec{0}$) reads:

$$\eta\nabla^2\vec{u}(\vec{r}) - \vec{\nabla}p(\vec{r}) - \sum_{j=1}^{N} n_j z_j e\vec{\nabla}\phi(\vec{r}) = \vec{0}, \tag{3.59}$$

where n_j is the number density of the ion species j. The last term in this equation is the body force density due to the electrostatic interactions and introduces the retardation force in the equations. The electric potential ψ (including the applied field) satisfies the Poisson equation, Eq. 3.41. At the low velocities typically encountered in electrophoresis, the fluid can in a good approximation be considered as incompressible, in which case the continuity equation simplifies to:

$$\vec{\nabla}\cdot\vec{u}(\vec{r}) = 0. \tag{3.60}$$

The number of ions in the system is conserved:

$$\frac{\partial n_j}{\partial t} = -\vec{\nabla}\cdot(n_j\vec{v}_j) = 0, \tag{3.61}$$

where the ion velocities $\vec{v}_j$ can be found from the Nernst-Planck (NP) equation plus an advective term in the steady state:

$$\lambda_j(\vec{u}(\vec{r}) - \vec{v}_j) - z_j e\vec{\nabla}\phi(\vec{r}) - k_\mathrm{B}T\vec{\nabla}\log n_j = \vec{0}. \tag{3.62}$$

The first term of this equation is the advective contribution due to the fluid flow with λ_j being the drag coefficient of the ith ion species. The second term is the electric force due to the external field, and the last term is the diffusive contribution due to the ideal gas contribution to the chemical potential.

---

[4] The Reynolds number is a dimensionless quantity defined as the ratio of the inertial to the viscous forces and is used to determine the flow regime in a fluid or find similar flow patterns in different ones. Since it is the only parameter present in the non-dimensional form of the NS equation, the Reynold number characterizes the flow for a given geometry.

The boundary conditions needed to solve these equations are:

$$\begin{cases} \vec{u}(|\vec{r}| = r_\mathrm{s}) & = \vec{0}, \\ \vec{u}(|\vec{r}| \to \infty) & = -\mu \vec{E}, \end{cases} \tag{3.63}$$

associated with equations 3.59 and 3.61, where r_s is the position of the shear plane, and:

$$\begin{cases} \vec{v}_i(|\vec{r}| = r_\mathrm{s}) \cdot \hat{n} & = 0, \\ n_i(|\vec{r}| \to \infty) & = n_i^0(\infty), \end{cases} \tag{3.64}$$

for the ions, where $\hat{n}$ is the unit vector perpendicular to the surface and $n_i^0(\infty)$ is the equilibrium density of the ions in the bulk.

These equations govern electrokinetic phenomena and can, in principle, be used for solid surfaces of arbitrary shape. In this work, I will focus on the electrophoresis of spherical colloids. Solving this set of coupled nonlinear partial differential equations analytically is possible only for the most simple geometries or situations. Recently, Lizana *et al.* [110] derived asymptotically exact expressions for the electrophoretic mobility of weakly charged spheres in a monovalent salt solution using the DH approximation. However, for generic conditions the usual approach is numerical, and analytical solutions exist only for a few limiting cases which will be introduced below.

Hückel limit

In the absence of added salt, the only ions in the system are the intrinsic counterions produced by the dissociation of surface groups. For a charged sphere the electrical potential decreases as $1/r$ with distance and cannot compete with the increase in entropy which causes the counterions to "evaporate" from the surface. In an infinite volume or in the limit of no salt, the particle is merely a sphere with charge Q subject to an electric force $\vec{F}_\mathrm{e} = Q\vec{E}$. The only force opposing its motion is the Stokes viscous drag force exerted by the fluid $\vec{F}_\mathrm{d} = 6\pi\eta R\vec{v}$, where R is the radius of the particle and $\vec{v}$ its velocity. In the steady state, these two forces cancel each other and the particle moves with a drift velocity v_d:

$$\vec{v}_\mathrm{d} = \frac{Q}{6\pi\eta R}\vec{E}. \tag{3.65}$$

For low applied field strengths, the electrophoretic mobility in this salt-free limit, known as the "Hückel limit" [111–113], is then simply given by:

$$\mu = \frac{Q}{6\pi\eta R}. \tag{3.66}$$

Since the potential vanishes at infinity, the zeta potential in this case is merely the potential at the surface:

$$\zeta = \frac{Q}{4\pi\varepsilon R}, \tag{3.67}$$

such that the mobility in Eq. 3.66 can be rewritten as:

$$\mu = \frac{2\varepsilon}{3\eta}\zeta. \tag{3.68}$$

This analytical expression derived for the Hückel limit can be used as an approximation for very low salt conditions where $\kappa R \ll 1$.

Helmholtz-Smoluchowski limit

In contrast to the Hückel limit, at very high salt concentrations the Debye layer is thin, $\kappa R \gg 1$. Most counterions accumulate in the close vicinity of the interface and "see" the particle as effectively flat. In other words, the local radius at each point is much larger than the Debye length and the geometry is essentially planar. This is the well-known "Helmholtz-Smoluchowski limit". Under these conditions at low Reynolds numbers, the Stokes equation (Eq. 3.59), with a body force proportional to a tangentially applied electric field $\vec{E} = \{E_x, 0, 0\}$, yields the tangential fluid speed u_x as:

$$\frac{\mathrm{d}^2 u_x}{\mathrm{d}h^2} = -\frac{E_x \rho(h)}{\eta}, \tag{3.69}$$

where h is the vertical distance from the surface and $\vec{\nabla} p = \vec{0}$ parallel to it due to symmetry arguments. The pressure gradient perpendicular to the surface is cancelled by the perpendicular force component arising from the gradient in the ion distribution. Substituting the Poisson equation, Eq. 3.41, we obtain:

$$\frac{\mathrm{d}^2 u_x}{\mathrm{d}h^2} = \frac{\varepsilon E_x}{\eta}\frac{\mathrm{d}^2 \phi}{\mathrm{d}h^2}. \tag{3.70}$$

This ordinary differential equation is straight forward to solve. Integrating both sides twice with respect to h and applying the boundary conditions $\mathrm{d}u_x/\mathrm{d}h = \mathrm{d}\phi/\mathrm{d}h = 0$ as $h \to \infty$, $u_x(h_\mathrm{s}) = 0$, $u_x(\infty) = u_\mathrm{eo}$, $\phi(h_\mathrm{s}) = \zeta$, and $\phi(\infty) = 0$, we find the Helmholtz-Smoluchowski (HS) equation for the EOF velocity:

$$u_x = u_\mathrm{eo} = -\frac{\varepsilon\zeta}{\eta}E_x. \tag{3.71}$$

The *electrophoretic* mobility in this limit is then:

$$\mu = -u_\mathrm{eo}/E_x = \varepsilon\zeta/\eta. \tag{3.72}$$

The HS equation describes the constant plug flow velocity profile outside the Debye layer. Inside the layer the charge density decreases exponentially with distance from the surface as discussed in subsection 3.4.3, and so does the velocity:

$$u_x(h) = u_\mathrm{eo}\left(1 - e^{-\kappa h}\right). \tag{3.73}$$

The HS formula applies to all particle shapes as long as the condition $\kappa R \gg 1$ is fulfilled and

ζ is low, *i.e.* at very high salt concentrations the electrophoretic mobility is independent of the shape [114]. For high zeta potentials ($\zeta \gtrsim 2\ k_\mathrm{B}T/e \simeq 50$ mV) other effects such as the polarization of the Debye layer and surface conductance [100] become important and need to be taken into account. This is done either by solving the EK equations numerically or using approximate analytical expressions[100]. O'Brien provided such an expression which account for the diffuse-layer conductivity [115]:

$$\mu_\mathrm{red} \equiv \frac{3}{2}\frac{\eta e}{\varepsilon k_\mathrm{B} T}\mu = \frac{3}{2}\zeta_\mathrm{red} - \frac{6\left[\frac{\zeta_\mathrm{red}}{2} - \frac{\ln 2}{z}\left(1 - \exp\left(-z\zeta_\mathrm{red}\right)\right)\right]}{2 + \frac{\kappa R}{1+3m/z^2}\exp\left(-\frac{z\zeta_\mathrm{red}}{2}\right)}, \tag{3.74}$$

where μ_red and $\zeta_\mathrm{red} = e\zeta/(k_\mathrm{B}T)$ are respectively the reduced electrophoretic mobility and the reduced $\zeta-$potential, and m is the dimensionless mobility of the ions ($m \simeq 0.15$ in aqueous solution). The O'Brien equation (Eq. 3.74) is a simplified form of an equation derived by Dukhin and Semenikhin [100, 116] by neglecting terms of order $(\kappa R)^{-1}$.

Henry's formula

Henry [117] deduced a formula for the electrophoretic mobility of a spherical particle at intermediate salt concentrations, assuming the zeta potential to be low ($\zeta \leq 50$ mV):

$$\mu = \frac{2\varepsilon\zeta}{3\eta} f(\kappa R), \tag{3.75}$$

where $f(\kappa R)$ is a function smoothly varying between 1 (Hückel limit) and 1.5 (Helmholtz-Smoluchowski limit):

$$f(\kappa R) = 1 + \frac{(\kappa R)^2}{16} - \frac{5(\kappa R)^3}{48} - \frac{(\kappa R)^4}{96} + \frac{(\kappa R)^5}{96} + \left(\frac{(\kappa R)^4}{8} - \frac{(\kappa R)^6}{96}\right)\exp(\kappa R)\int\limits_{\infty}^{\kappa R}\frac{\exp(-t)}{t}\mathrm{d}t. \tag{3.76}$$

In needs to be mentioned that retardation effects are taken into account in this expression [118].

3.5.2 The Standard Electrokinetic Model (SEM)

The most commonly used method for solving the EK equations introduced in subsection 3.5.1 is the standard electrokinetic model (SEM) established by Wiersema *et al.* [24] and developed further by O'Brien and White [25]. Wiersema *et al.* employed an iterative numerical scheme to calculate the electrophoretic mobility of a spherical particle as a function of the zeta potential in the linear response regime, i.e. weak applied field. In this regime, $E \ll \kappa\zeta$, the distortion of the ionic cloud due to the applied field is assumed to be linear in E and a first-order perturbation can be applied to the EK equations. In this manner, besides the retardation force which is represented by the electric body force in the Stokes equation (Eq. 3.59), the theory takes into account small deformations of the EDL and thus, the first-order electrophoretic relaxation effect. Even though the theory is valid only for small applied fields, it makes no assumptions about the salt concentration or the size of the particle and can be used for the whole range of κR. Their method, however, suffers from a convergence problem for large values of ζ. O'Brien and White [25] used symmetry arguments to simplify the EK equations and thus, managed to solve the problem for large ζ-potentials. To linearize the set of coupled second-order differential EK equations, they write the number density of the ions and the electric potential respectively as:

$$\begin{aligned} n_i(\vec{r}) = &\quad n_i^{\mathrm{eq}}(\vec{r}) + \delta n_i(\vec{r}), && (3.77)\\ \phi_i(\vec{r}) = &\quad \phi^{\mathrm{eq}}(\vec{r}) + \delta\phi(\vec{r}), && (3.78) \end{aligned}$$

where $n_i^{\mathrm{eq}}(\vec{r})$ and $\phi^{\mathrm{eq}}(\vec{r})$ are the equilibrium values of the two quantities. Substituting these in the EK equations and neglecting smaller terms such as $\delta n_i\vec{u}$ or $(\delta n_i)^2$ yields:

$$\begin{cases} \nabla^2\delta\phi = -\frac{4\pi}{\varepsilon}\delta\rho, \\ \eta\nabla^2\vec{u} - \vec{\nabla}p = \rho^{\mathrm{eq}}\vec{\nabla}\delta\phi + \delta\rho\vec{\nabla}\phi^{\mathrm{eq}}, \\ \vec{\nabla}\cdot\left(k_{\mathrm{B}}T\vec{\nabla}\delta n_i + z_i e n_i^{\mathrm{eq}}\vec{\nabla}\delta\phi + z_i e\delta n_i\vec{\nabla}\phi^{\mathrm{eq}} - n^{\mathrm{eq}}\lambda_i\vec{u}\right) = 0. \end{cases} \tag{3.79}$$

The main idea of O'Brien and White for solving this set of linearized EK equations is to decouple the electrophoretic problem into two separate subproblems. Fixing the origin of the reference frame on the center of the particle, these are:

(1) No electric field is applied and the particle is held fixed in a fluid flow $-\vec{U}$. The corresponding boundary conditions far from the particle in the limit $\vec{r}\to\infty$ are:

$$\begin{cases} \vec{u}\to-\vec{U}, \\ \delta\phi\to 0. \end{cases} \tag{3.80}$$

$\delta\phi$ is the linear perturbation of the equilibrium potential $\phi^{\mathrm{eq}}(\vec{r})$ due to the applied field, $\phi(\vec{r}) = \phi^{\mathrm{eq}}(\vec{r}) + \delta\phi(\vec{r})$. This subproblem regards the purely hydrodynamic part of the problem and the force needed to fix the particle is $\vec{F}_1 = \alpha\vec{U}$ with α being a constant.

(2) The particle is held fixed under the application of an electric field and the electrolyte is assumed to be at rest far from it. The far-field boundary conditions in this case read:

$$\begin{cases} \vec{u}\to\vec{0}, \\ \delta\phi\to-\vec{E}\cdot\vec{r}. \end{cases} \tag{3.81}$$

The force needed to hold the particle against the applied electric field is $\vec{F}_2 = \beta\vec{E}$ where β is the proportionality constant.

The superposition of the solutions to these uncoupled subproblems, solves the main electrophoretic problem. The constraint of zero net force determines the velocity $\vec{U}$ obtained from the sum of equations 3.80 and 3.81. O'Brien and White [25] then set $\vec{F}_1$ and $\vec{F}_2$ to be equal, and use the definition of the electrophoretic mobility to find:

$$\mu = -\frac{\beta}{\alpha}. \tag{3.82}$$

The constants α and β are obtained numerically by solving problems (1) and (2) with $|\vec{U}| = 1$

and $|\vec{E}| = 1$, respectively, considering a Boltzmann-like distribution of the ions. The details of the numerical scheme is outside of the scope of this thesis and can be found in [25].

For the purposes of this thesis, it is important to emphasize on the fact that this model accounts for small EDL deformations and takes into account relaxation effects.

3.5.3 Modified Electrokinetic Equations for Soft Surfaces

In this section, the modified EK equations for polymer-grafted surfaces, referred to as *soft* surfaces or particles, are introduced. Soft particles play an important role in biology as well as in technology. Many cells and surfaces are coated with polymers influencing the adhesion of bacteria and as such, the infection rates [27–30]. The coating also affects the rheological properties of electrorheological fluids and can have important industrial applications [31, 32]. In the laboratory, polymer coatings are used to manipulate the electrokinetic properties of surfaces in micro- and nanofluidic devices [40–42]. The broad range of occurrences and applications necessitates a good understanding of soft particles. Their behavior is, on the other hand, more complex due to the non-uniform surface properties and the effect of the grafted polymers on the electro-osmotic flow. These effects should be considered in the theory as well in order explain and predict their behaviour correctly. In Ch. 5, the electrophoresis of soft particles are studied via computer simulations and it is therefore necessary to know the underlying theory for the electrokinetics of such systems.

The electrokinetic behaviour of soft particles is more complex than that of solid surfaces due to the extra viscous friction of the coating layer and, in case of grafted polyelectrolytes, the inhomogeneous surface charge density. A good model should take these effects into account by modifying the EK equations introduced in the previous section. Since the polymers are grafted to the surface, when subject to an EOF they will move with the same velocity $\vec{V}$ as the particle relative to the fluid and cause extra friction. This additional hydrodynamic drag enters the steady-state Stokes equation, Eq. 3.59, as a body force:

$$\eta\nabla^2\vec{u}(\vec{r}) - \vec{\nabla}p(\vec{r}) + \frac{\eta}{l^2(\vec{r})}(\vec{V} - \vec{u}(\vec{r})) - \sum_{j=1}^{N} n_j z_j e\vec{\nabla}\phi(\vec{r}) = \vec{0}. \tag{3.83}$$

This modified Stokes equation is referred to as the Darcy-Brinkman equation and accounts for the local viscous shearing stresses acting on a volume element of the fluid. It was originally proposed to describe the fluid around a spherical particle embedded in a porous media by Brinkman [119]. The important parameter here is the Brinkman length l related to the monomer distribution, with l^2 being the permeability of the coating. The higher the monomers density, the less permeable the polymer layer that acts like a porous medium, and hence the larger the extra hydrodynamic drag it exerts on the fluid. The relation between l and the monomer distribution can be established via different strategies. Harden *et al.* [120] use the de Gennes' blob picture discussed in subsection 3.6.3 to describe the Brinkman screening length, while Hill *et al.* [7] interpret the grafted layer as a random distribution of resistance centers. The concept of zeta potential used to characterize bare colloids is not helpful in the case of soft particles due to the nonuniform surface structure and charge distribution (for polyelectrolytes). Defining the location of the slip plane becomes unclear and even if defined, the conversion of ζ to μ would be dependent on the specific system [28, 44]. Instead, the charge density or the electrostatic potential at the core particle's surface and the Donan potential at the layer's edge are used as boundary conditions [7, 121–123]. Below, I first introduce the theoretical work of Harden *et al.* [120] and some of their results which are used later in Ch. 5. Next, I present the main concepts of a numerical method for solving the modified EK equations similar to the SEM (see 3.5.2) developed by Hill et al. [7] and exploited later in Ch. 5

3.5.4 A Scaling Theory for the Electrokinetics of Polyelectrolyte-Grafted Surfaces

Harden *et al.* [120] investigated the influence of grafted polyelectrolytes on the EOF past a charged flat surface. They focus on the limit of a thin Debye layer where λ_{D} is the smallest length scale of the system and consider the two cases of sparsely and densely grafted chains. In the former case, the "mushroom regime", the distance between the grafting points d is large so that the chains retain their equilibrium shape and form a coil of radius R where $R \ll d$. The latter case is the "brush regime" where $R \gg d$, the chains overlap strongly and as a result stretch to form a brush of height H. The high salt concentration guarantees that the electrostatic interactions between the monomers are screened and have no influence on the polymer configurations. They also disregard the deformation of the grafted layer due to electrostatic attraction/repulsion to the substrate.

Independent of the chains regime, each component, i.e. the surface and the polyelectrolytes, generates its own EOF. Characterizing the charged substrate by its electrophoretic mobility μ_{s} and similarly the chains by μ_{p}, the slip velocity of the fluid far away due to each part is $\vec{U}_{\mathrm{s}} = -\mu_{\mathrm{s}}\vec{E}$ and $\vec{U}_{\mathrm{p}} = -\mu_{\mathrm{p}}\vec{E}$, respectively. The authors of [120] decompose the system into two parts:

$$\begin{cases} 1- \ \mu_{\mathrm{s}} = \hat{\mu},\ \mu_{\mathrm{p}} = 0, \\ 2- \ \mu_{\mathrm{s}} = \mu_{\mathrm{p}} \neq 0, \end{cases}$$

where $\hat{\mu} \equiv \mu_{\mathrm{s}} - \mu_{\mathrm{p}}$ is the electrophoretic mobility of the composite. In the first case, the polymers are considered to be neutral and the surface is assigned an effective mobility. In the second case, both the surface and the chains are charged and have the same mobility. The superposition of these two reconstructs the original situation of the charged flat surface grafted with charged polymers. In the mushroom regime, the first case is analogous to a flat surface with heterogeneous charge density [124] where the mobility can be written as $\hat{\mu}_{\mathrm{eff}} = \hat{\mu}_{\mathrm{s}}(1 - \sigma R^2)$, with $\sigma \sim 1/d^2$ being the grafting density. Here, the neutral polymer coils respond hydrodynamically as impermeable bumps and affect the fluid flow. This is regarded for by a prefactor α in writing the effective mobility as $\hat{\mu}_{\mathrm{eff}} = \hat{\mu}_{\mathrm{s}}(1 - \alpha\sigma R^2)$. α is constant of the order of unity and depends on the shape of the bump. Applying the aforementioned superposition strategy, the mobility of the original composite surface and polyelectrolytes reads:

$$\mu_{\mathrm{eff}} = \hat{\mu}_{\mathrm{eff}} + \mu_{\mathrm{p}} = \mu_{\mathrm{s}} - (\mu_{\mathrm{s}} - \mu_{\mathrm{p}})\sigma R^2. \tag{3.84}$$

For the first problem (charged substrate and neutral polymers) in the brush regime, the grafted layer can be viewed as a collection of blobs which behaves as a porous media with characteristic pore size $\xi = d$ that screens the hydrodynamic flow of the solvent, see Fig. 3.12. Calculating the permeability from the blob size and solving the equation $\nabla^2\vec{U}(z) \propto (\vec{U}(z) - \mu_\mathrm{s}\vec{E})/d$, it is found that the EOF decays exponentially within the brush as $\vec{U}(z < H) \simeq \vec{U}_\mathrm{s}\cosh[(H - z)/d]/\cosh[H/d]$. It needs to be noted that this differential equation for $\vec{U}$ is a variant of the Darcy-Brinkman equation, Eq. 3.83 introduced in subsection 3.5.3. Outside the grafted layer, there are no screening effects and the uniform plug flow is $\vec{U}_> = \vec{U}(z = H) = -\hat{\mu}_\mathrm{eff}\vec{E}$ where:

$$\hat{\mu}_\mathrm{eff} = \frac{\hat{\mu}_\mathrm{s}}{\cosh[(\sigma R^2)^{5/6}]}. \tag{3.85}$$

$(\sigma R^2)^{5/6} = H/d$ is the dimensionless brush thickness. When the chains are charged, the effective mobility is the sum of Eq. 3.85 and the mobility of the polyelectrolytes μ_p as discussed above, i.e. $\mu_\mathrm{eff} = \hat{\mu}_\mathrm{eff} + \mu_\mathrm{p}$. Note that in the limit of $H/d \to \infty$ this effective mobility approaches that of the polyelectrolytes, $\mu_\mathrm{eff} \to \mu_\mathrm{p}$.

The results reported here from Harden *et al.*'s work [120] are for weak applied fields where the deformation of the grafted chains is negligible. The authors discuss in length the effects of strong fields on the layer conformation which in turn affects the induced EOF. But this is not relevant to the subject of this thesis as it is restricted to weak fields and therefore not considered here.

3.5.5 Numerical Method for Solving the Modified EK Equations

Using a different method as discussed in the previous subsection to describe the grafted layer and viewing the monomers as uniformly distributed resistance centers, Ohshima [43, 44, 122, 123] has derived analytical approximations for the mobility of spherical soft particles at different limits of salt concentration and layer thickness. Nevertheless, as in the case of bare particles, to obtain the electrophoretic mobility of a soft particle under general conditions, the modified EK equations introduced in subsection 3.5.3 should be solved numerically. Hill *et al.* have developed such a numerical method, which uses a technique similar to the SEM, discussed in subsection 3.5.2, to solve the governing set of equations [7, 125]. Considering the monomers as fixed spherical Stokes particles with radius a_s, they obtain the Brinkman length by equating the Darcy drag term, the third term on the right-hand side of Eq. 3.83, to the total drag force exerted on the polymer segments $6\pi\eta n_\mathrm{s}(r)a_\mathrm{s}(\vec{u} - \vec{V})F_\mathrm{s}$:

$$l^2 = 1/(6\pi n_\mathrm{s} a_\mathrm{s} F_\mathrm{s}) = 2a_\mathrm{s}^2/(9\varphi_\mathrm{s} F_\mathrm{s}). \tag{3.86}$$

$n_\mathrm{s}(r)$ is the monomer density which is assumed to be spherically symmetric, a_s is the monomer size, and $\varphi_\mathrm{s} = \frac{4}{3}\pi n_\mathrm{s} a_\mathrm{s}^3$ is the volume fraction of the segments. F_s is a dimensionless constant taking into account the collective effect of the other monomers on the fluid flow or equivalently the hydrodynamic drag. For randomly distributed spherical segments considered here, F_s only depends on φ_s:

$$F_\mathrm{s} = \frac{1 + 3(\varphi_\mathrm{s}/2)^{1/2} + (135/64)\varphi_\mathrm{s}\ln\varphi_\mathrm{s} + 16.456\varphi_\mathrm{s}}{1 + 0.681\varphi_\mathrm{s} - 8.48\varphi_\mathrm{s}^2 + 8.16\varphi_\mathrm{s}^3}. \tag{3.87}$$

The boundary conditions are the same as in the SEM except one could specify the surface charge density instead of using ζ-potential. In that case, the following equation is applied at the interface:

$$\varepsilon_0\varepsilon_\mathrm{s}\nabla\psi\big|_+\cdot\hat{n}-\varepsilon_0\varepsilon_\mathrm{p}\nabla\psi\big|_-\cdot\hat{n}=-\sigma_\mathrm{s}\ \text{ at }\ r=\kappa R, \tag{3.88}$$

where ε_p and ε_s are the dielectric constant of the particle and the solvent, respectively. In this equation, the distances are scaled with the Debye length λ_D, potentials with $k_\mathrm{B}T/e$, and the surface charge density with $\kappa\varepsilon_0 k_\mathrm{B}T/e$. The authors then use the separation method of SEM to obtain μ numerically.

More recently, Bhattacharyya *et al.* used a different technique to calculate the electrophoretic mobility of soft particles numerically [126, 127]. Their method is also based on the nonlinear Poisson-Nernst-Planck equation coupled with the Darcy-Brinkman equation. But, to analyze the fluid flow field, they use a numerical approach in which the porous media is considered as a pseudo-fluid and the composite region as continuum.

In Ch. 5 of my work, I use the computer program provided by Rhegan Hill [125] to compare my simulations with numerical results. A more detailed description of this method can be found there.

3.6 Polymers

Polymers are an important component of many biological and technological systems. Most familiar examples are DNA, proteins, and plastics. They are also encountered in the second part of this thesis where polyelectrolyte-grafted spherical particles are investigated. Therefore, here some basics of polymer physics are provided. The content in this section is mostly gathered from Rubinstein and Colby's book of "Polymer Physics" [128], de Gennes' book of "Scaling concepts in Polymer Physics" [129], and Iwao Teraoka's "Polymer Solutions: An Introduction to Physical Properties" [130].

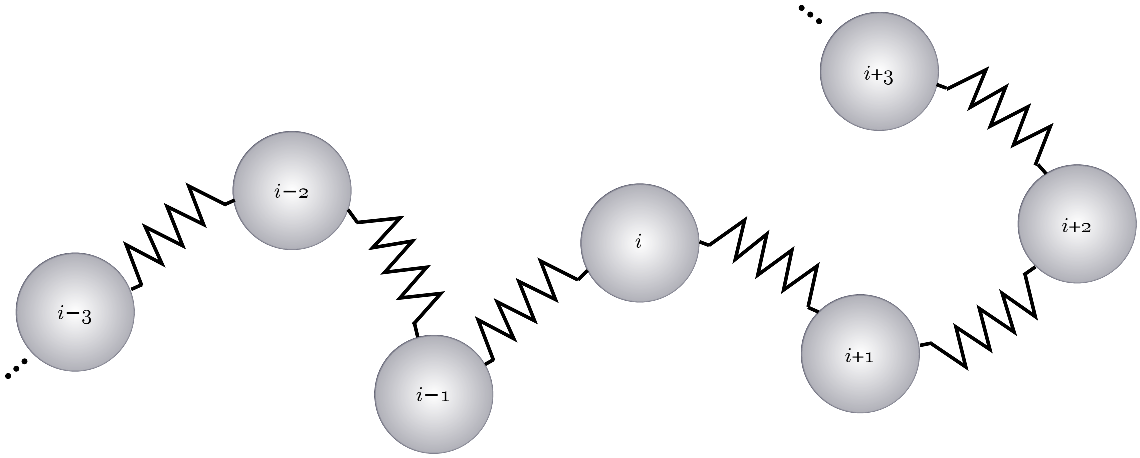

Figure 3.11: A schematic of a polymer. The gray circles are the monomers connected via bonds represented by the springs.

3.6.1 Conformation of an Ideal Chain

In an ideal polymer chain, the interactions between monomers i and j far apart from each other along the chain, i.e. $|j-i| \gg 1$, are ignored even as they approach each other spatially. This is a subtle assumption which is not generally met for real polymers, but in many situations real polymers behave like ideal chains. The conformation of an ideal chain is relatively easy to derive and many of the same ideas can be used in the study of real polymers with small modifications. It is therefore useful to start with deriving the conformation of ideal chains.

The simplest model to describe an ideal polymer is the freely jointed chain model in which it is assumed that there are no preferred bond directions between two adjacent monomers. The end-to-end vector connecting the two ends of a single polymer chain consisting of n monomers is:

$$\vec{R}_n = \sum_{i=1}^{n} \vec{r}_i, \tag{3.89}$$

where $\vec{r}_i$ is the bond vector between monomers $i-1$ and i. A direct consequence of the assumption mentioned above is that $\left\langle \vec{R}_n \right\rangle = \vec{0}$. The first nonzero quantity containing information about the size of a chain is the mean-square end-to-end distance:

$$\left\langle R^2 \right\rangle \equiv \left\langle \vec{R}_n^2 \right\rangle = \left\langle \vec{R}_n \cdot \vec{R}_n \right\rangle = \sum_{i,j=1}^{n} \left\langle \vec{r}_i \cdot \vec{r}_j \right\rangle. \tag{3.90}$$

Considering the equilibrium bond length to be $|\vec{r}_i| = l$ for all i, and using the fact that $\langle \cos\theta_{ij} \rangle = 0$ for $i \neq j$, with θ_{ij} being the angle between $\vec{r}_i$ and $\vec{r}_j$, we find $\langle R^2 \rangle$ for an ideal polymer chain as:

$$\left\langle R^2 \right\rangle = nl^2. \tag{3.91}$$

The condition $\langle \cos\theta_{ij} \rangle = 0$ is an oversimplification. In general, the main assumption for ideal chains is that correlations between bond vector orientations are negligible only for monomers distant along the chain contour, i.e.

$$\lim_{|i-j| \to \infty} \langle \cos\theta_{ij} \rangle = 0.$$

Defining $C'_i \equiv \sum_{j=1}^{n} \langle \cos\theta_{ij} \rangle$, the mean-square end-to-end distance for an ideal chain in general reads:

$$\left\langle R^2 \right\rangle = l^2 \sum_{i=1}^{n} C'_i = C_n n l^2, \tag{3.92}$$

where in the last step Flory's characteristic ratio C_n is introduced. Due to steric repulsions and bond angle restrictions, $C_n > 1$ for all polymers, its exact value depends on the local stiffness of the polymer. This makes the description of flexible ideal polymers non-universal. By considering groups of monomers such that no correlation exists between them even when they are distant, it is possible to map any ideal polymer into a freely jointed chain model. Each such group of monomers is called a "Kuhn monomer" (often simply referred to as a monomer), and an effective bond of length b, termed the "Kuhn length", connects them together.The so-called "equivalent freely jointed chain" model uses the concept of Kuhn length and monomers to provide a unified description of all ideal chains. The effective bonds have no preferred direction and the maximum chain length $R_{\text{max}} = Nb$ is obtained when all the monomers are aligned. The root-mean-square end-to-end distance is usually denoted by R_0 and for an ideal chain reads:

$$R_0 \equiv \sqrt{\langle R^2 \rangle} = bN^{1/2}. \tag{3.93}$$

Another important quantity used to characterize the size of a chain is the radius of gyration defined as the average square distance between monomers and the center of mass of the polymer in a given conformation:

$$R_{\text{g}}^2 = \frac{1}{N} \sum_{i=1}^{N} \left(\vec{R}_i - \vec{R}_{\text{cm}} \right)^2. \tag{3.94}$$

In this equation, $\vec{R}_i$ and $\vec{R}_{\text{cm}}$ are the positions of the ith monomer and the center of mass, respectively. For a linear (i.e. not ring or branched) ideal chain with $N \gg 1$ segments, the sum can be replaced by an integral and, making use of the definition of the center of mass and treating each subsection also as an ideal chain, the average radius of gyration can be written as:

$$\left\langle R_{\text{g}}^2 \right\rangle = \frac{b^2 N}{6} = \frac{\langle R^2 \rangle}{6}. \tag{3.95}$$

For determining the hydrodynamic friction coefficient of a polymer, the hydrodynamic radius R_{h} is defined as:

$$\frac{1}{R_{\text{h}}} \equiv \frac{1}{N^2} \left\langle \sum_{i \neq j} \frac{1}{|\vec{r}_{ij}|} \right\rangle. \tag{3.96}$$

R_{h} is the radius of an equivalent sphere having the same friction coefficient as the polymer when dragged in a fluid.

The (equivalent) freely jointed chain model is equivalent to a random walk and each possible conformation of a polymer with N monomers can be considered as a possible trajectory after N steps. The statistics of a random walk can therefore be used to derive further information about the static conformation of an ideal chain. For example the number of possible configurations for a fixed N corresponds to the number of distinct walks with N steps on a discrete lattice of size b:

$$\sum_{\vec{r}} \mathcal{R}_N(\vec{r}) = z^N, \tag{3.97}$$

where z is the number of nearest neighbors at each lattice site and $\vec{r}$ is the position of the last step (i.e. the end monomer). One of the interesting quantities is the distribution of the end-to-end distance. Putting the origin of the coordinate system on the first monomer, this is,

$$p(\vec{r}) = \frac{\mathcal{R}_N(\vec{r})}{\sum_{\vec{r}} \mathcal{R}_N(\vec{r})}. \tag{3.98}$$

It can be shown [130] that $p(\vec{r})$ is Gaussian for $N \gg 1$ and in 3D can be written as:

$$p(\vec{r}) = (2\pi N b^2/3)^{-3/2} \exp\left(-\frac{3\vec{r}^{\,2}}{2Nb^2} \right). \tag{3.99}$$

The entropy $\mathcal{S}(\vec{r}) = k_{\text{B}} \ln(\mathcal{R}_N(\vec{r}))$ associated with all chain conformations in 3D can be calculated from $p(\vec{r})$ obtained above as:

$$\mathcal{S}(\vec{r}) = \mathcal{S}(0) - \frac{3k_{\mathrm{B}}}{2R_0^2}\vec{r}^2. \tag{3.100}$$

The corresponding Helmholtz free energy is then obtained to be:

$$\mathcal{F}(\vec{r}) = \mathcal{F}(0) + \frac{3k_{\mathrm{B}}T}{2R_0^2}\vec{r}^2. \tag{3.101}$$

In equilibrium the end-to-end vector $\vec{r}$ is minimized in order to minimize the free energy. The spring constant of the ideal chain can thus be calculated by taking the derivative of $\mathcal{F}$ with respect to $\vec{r}$.

3.6.2 Conformation of a Real Chain

In a real polymer, the excluded volume of the monomers plays a role and the interaction between monomers far apart along the chain cannot be neglected when they come close to each other in space. Each monomer has an excluded volume v where it is energetically unfavorable for other monomers to enter. This changes the chain conformation compared to an ideal polymer. The bond orientations are no longer equally probable and the random walk model cannot be applied to real polymers. The simplest model in this case is the self-avoiding random walk (SAW) where a lattice point is not visited more than once. This represents the fact that in real polymers monomers do not overlap each other even when they lie far apart along the chain contour. The total number of distinct SAW trajectories with N steps has the asymptotic behavior:

$$\mathcal{R}_N(tot) \approx \tilde{z}^N N^{\gamma-1}, \tag{3.102}$$

in the limit of $N \to \infty$. $\tilde{z}$ is the equivalent of the number of lattice nearest neighbors z in a random walk, but is smaller than z for the same grid geometry. The exponent γ is a universal quantity depending *only* on the dimensionality. Using the SAW statistics, the end-to-end distance of a real chain R_{F} is found to be:

$$R_{\mathrm{F}} = \sqrt{\langle r^2 \rangle} = bN^{\nu}. \tag{3.103}$$

ν is another universal exponent called the Flory exponent for reasons that will become clear below. In 3D $\gamma = \gamma_3 \cong 7/6$ and $\nu = \nu_3 \cong 3/5$.

When the chain is immersed in a solvent, the monomers interact both with each other and the solvent particles. The difference between the direct interaction of a monomer with another monomer and its interaction with a solvent molecule determines if the effective monomer-monomer interaction is attractive, or repulsive, which in turn dictates the conformation of the chain. Solvents are categorized in different types with regard to this effective interaction, the main ones being:

- *Good Solvent*: the attractive well of the monomer-monomer interaction is slightly deeper than that of the monomer-solvent interaction. The net attraction reduces the excluded volume effect but the chain is still larger than the ideal case and has a $\nu = 3/5$ behavior. Hence, usually a polymer in a good solvent is simply referred to as a real chain.

- *Theta Solvent*: The attractive and repulsive contributions to the effective monomer-monomer interaction exactly cancel at a special temperature called the θ-temperature. The net excluded volume is zero and the chains behave like ideal polymers.
- *Poor solvent*: At $T < \theta$, the attractive part dominates, monomers prefer each other to solvent particles and the chain forms a coil to minimize its free energy. In the limiting case of a poor solvent, called a non-solvent, almost all the solvent molecules are excluded from the polymer coil.

Flory and Huggins developed a mean-field theory, known as the Flory theory, to address the problem of the equilibrium conformation of polymers in different solvent types. It is based on the minimization of the free energy $\mathcal{F}$ with respect to enthalpy and entropy. Here I focus on the case of good solvents such as the model used in our simulations, introduced in Ch. 5.

Assume a uniform distribution of monomers in a polymer of size R, neglecting all correlations. The probability of a monomer being in the excluded volume of another is Nv/R^3 and its energy cost is of the order of $k_\mathrm{B}T$. The energetic contribution due to dispersive interactions of all monomers is then:

$$\mathcal{F}_\mathrm{int} \approx k_\mathrm{B}Tv\frac{N^2}{R^3}. \tag{3.104}$$

The contribution due the entropy loss is found from the energy needed to stretch an ideal chain to size R (see Eq. (2.101) of Ref. [128]) and can be written as:

$$\mathcal{F}_\mathrm{ent} \approx k_\mathrm{B}T\frac{R^2}{Nb^2} \tag{3.105}$$

The total free energy is the sum of these two parts and minimizing it with respect to R, the characteristic size of a polymer in a good solvent R_F is obtained:

$$R_\mathrm{F} \approx v^{1/5}b^{2/5}N^{3/5}. \tag{3.106}$$

Calculating the swelling ratio $R_\mathrm{F}/R_0 \sim (vN^{1/2}/b^3)^{1/5}$ reveals that a real polymer is larger than an ideal chain containing the same number of monomers. In the general case of d-dimensions, the total free energy is $\mathcal{F}_\mathrm{tot} \propto vN^2/R^d + R^2/(Nb^2)$ and the generalized Flory exponent can be obtained by

$$\frac{\partial\mathcal{F}_\mathrm{tot}}{\partial R} \propto -\frac{dvN^2}{R^{d+1}} + \frac{2R}{Nb^2} = 0 \quad\Rightarrow\quad R \propto N^{\frac{3}{d+2}},$$

to be $\nu = 3/(d+2)$.

As shown in the previous subsection, the Flory exponent ν for a linear ideal chain (or a polymer in a Theta solvent) has the value $\nu = 1/2$. The Flory approximation $\nu = 3/5$ for a swollen linear chain in a good solvent in 3D has been proven to be a very good approximation by experiments [131], numerical calculations [129, 132], and more sophisticated theories [130, 133].

3.6.3 Polymer Brushes

Surfaces grafted with polymers are found in a wide variety of biological as well as artificial systems. When the grafting density σ is high enough so that the chains partially overlap, they stretch in order to minimize their free energy and form a brush. Depending on the geometry

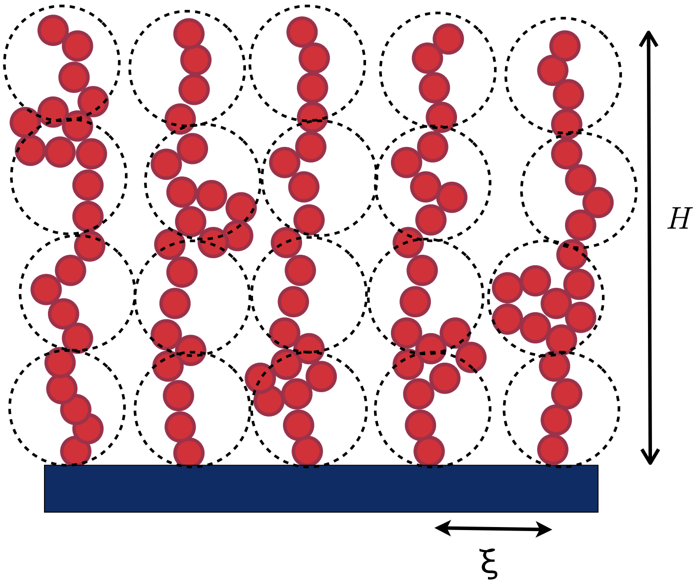

Figure 3.12: 2D schematic view of a polymer Alexander-de Gennes brush. The dashed circles visualize the de Gennes blobs.

of the substrate (e.g. planar, spherical or cylindrical), the brush can have different forms. The case of a flat grafting surface is known as the Alexander-de Gennes brush where it is assumed that all chains have a height H which is also then the height of the layer. To find H, the chains are considered as a stretched array of "blobs" of size ξ, as shown in Fig. 3.12. $\xi \approx 1/\sqrt{\sigma}$ is the distance between the grafting points and defines the correlation length in the layer. The chain segment within the correlation volume behaves like a self-avoiding random walk and the number of monomers g in each blob can be determined via the SAW statistics to be:

$$g \approx \left(\frac{\xi}{b}\right)^{1/\nu} \approx \sigma^{-1/2\nu} b^{-1/\nu}. \tag{3.107}$$

The number of blobs in each chain is then simply $N/g \approx N\sigma^{1/2\nu} b^{1/\nu}$ and the height of the brush reads:

$$H \approx \xi \frac{N}{g} \approx N\sigma^{(1-\nu)/2\nu} b^{1/\nu}. \tag{3.108}$$

Similar arguments can be applied to other brush geometries assuming step-like polymer segments distribution, having a uniform density within the layer and dropping to zero abruptly at a well-defined height, as done in the Alexander-de Gennes brush model. This assumption is an oversimplification not met in real systems where the monomer distribution is continuous. Duval *et al.* [134, 135] were the first to relax this restriction in the context of electrokinetics by considering a gradual change in the diffuse layer properties. The impact of the inhomogeneous distribution adopted on the electrokinetic behavior of such systems was further investigated by Duval and Ohshima [136]. They found that the electrokinetic properties of polymer-grafted particles are greatly affected by the inhomogeneity of the layer, for example minima and maxima in the electrophoretic mobility disappears by increasing the heterogeneity of the brush.

4 Electrophoretic Mobility Reversal of Bare Colloids in Multivalent Salt Solutions

The topic of electrophoresis dates back as far as the late 19th century [137]. The earnest study of the electrophoresis of colloidal particles began in the early 1900s [137, 138] and has developed significantly since then. Extensive experimental, numerical, and theoretical studies had been performed [24, 25, 111, 112, 139, 140], and many related phenomena are now quite well understood, but not all of them. In recent years some experiments have demonstrated phenomena which cannot be explained by the common theories such as the standard electrokinetic model (SEM) [24, 25] (introduced in subsection 3.5.2). For example, charge inversion, and the closely related phenomenon of mobility reversal in the presence of multivalent salt observed in many experiments [4, 5, 20–23] are beyond the capacity of the mean-field approach employed by these theories. In charge inversion, more counterions are attracted to the surface than necessary to neutralize the particle and consequently its effective charge [141, 142] becomes opposite in sign to that of the surface charge, which can, in turn, lead to mobility reversal. Most theoretical studies attribute charge inversion to the ion-ion correlations at high concentrations of multivalent salt [143–153], an important feature absent in PB and other mean-field theories. Comprehensive discussions on this view can be found in refs [154, 155]. Another view claims specific ion adsorption of the counterions in the Stern layer to the surface to be responsible for charge inversion [5, 156–158]. In this context, *specific* means of non-Coulombic origin. Most works on this subject recognize only one of these effects as the cause of the charge inversion and the resulting mobility reversal. In this part of the thesis it is shown that in some cases neither the Coulombic correlations, nor the non-Coulombic specific adsorption *singly* explains this counter-intuitive phenomenon.

Here, the interesting and counter-intuitive phenomena of mobility reversal is investigated and some experimental results are explained using a new technique which employs both MD simulations and the SEM. There have been a wide variety of computational models developed for the electrophoretic mobility of colloids [61, 159], however these methods have certain drawbacks. Several studies have looked at the mobility of colloids by modeling the colloid, as well as the ions, explicitly via charged spheres coupled to a lattice-Boltzmann (LB) model (see subsection 3.3.1) for the fluid [160–162]. This approach has the disadvantage that it is limited to colloids of a few tens of nanometers, which is much smaller than the colloids used in experiments that are typically on the order of micrometers. Other approaches such as [163–166] are able to access much larger length scales by considering the ions on a mean-field level. This essentially produces the same results as one gets by solving the EK equations using PB to describe the electrostatics, ignoring the ion-ion correlations which are crucial for multivalent salt. We circumvents these deficiencies by employing MD simulations of the restricted primitive model (described in detail in Sec. 4.1) to examine the ionic structure and to calculate the $\zeta-$potential. The electrophoretic mobility is then computed by using the obtained $\zeta-$potential as an input for the numerical solver available for the SEM. In this manner, we take into account the ion correlations explicitly and produce a modified boundary condition for the mean-field treatment in the sense of Perel and Shklovskii [167]. We apply our method to two different colloids having different radii and surface charge densities studied in two distinct experiments [4, 5] in the presence of mono-, di-, and trivalent salt. Our simulations show that for these systems both the Coulombic correlations and the specific adsorptions are responsible for the mobility reversal observed in the trivalent case.

Here, I first introduce the simulation method used for this purpose in Sec. 4.1, and then discuss the results in Sec. 4.2. It needs to be noted that most of the content in this chapter is directly taken from the publication "*Langmuir*, 2014, 30(7), pp 1758 – 1767" [3].

4.1 Simulation Method

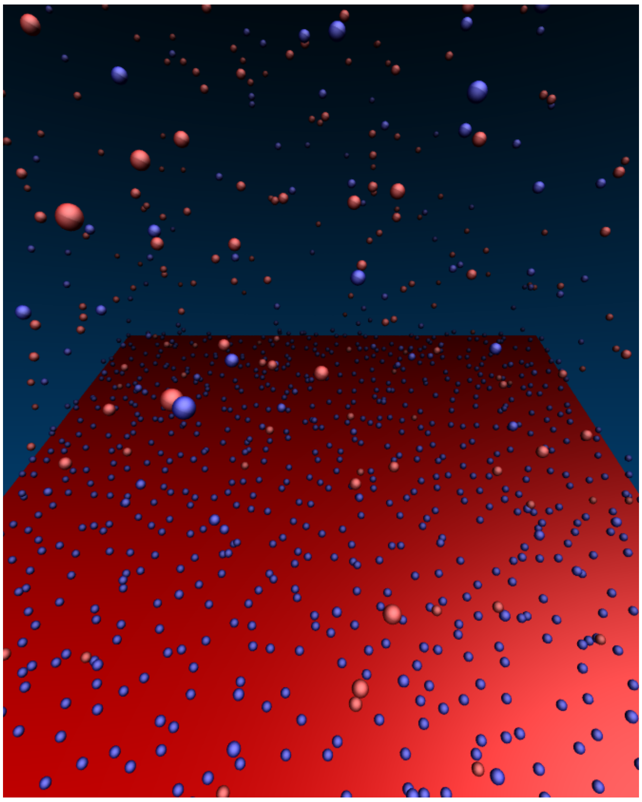

Figure 4.1: An MD snapshot of the bare colloid in the presence of $c_s = 0.003$ M of divalent salt. The colloid (red surface at the bottom) is modelled as a flat homogeneously charged plane with surface charge density $\sigma_s = -5.64\ \mu\text{C/cm}^2 \simeq -0.35\ \text{e/nm}^2$. The positive and negative ions are represented via blue and red spheres, respectively.

We perform MD simulations, using the Extensible Simulation Package for Research on Soft matter (ESPResSo) package [168], to calculate the ζ of a single colloid and use numerical solutions of the SEM (see subsection 3.5.2) to obtain the corresponding electrophoretic mobility. The colloidal particles investigated are quite large (with radii about one micrometer) compared to the surrounding salt ions (of Angstrom size), having radii about 10^4 times larger. Direct modeling of the colloid as a sphere in the presence of explicit ions would thus require an unreasonably large number of counterions, even at a coarse grained level. As shown in the next section, the large size of the colloid assures that the Debye length is smaller than the particle size ($\kappa R \gg 1$) over the whole salt concentration rage considered here. As discussed in 3.5.1, this is the Helmholtz-Smoluchowski limit in which the geometry is essentially planar and the colloid can be safely modeled as a uniformly-charged flat plate as shown in Fig. 4.1. This model has the limitation that the mobility cannot be obtained directly by applying an electric field and measuring the particle velocity, or the equivalent electroosmotic flow velocity. However, we take advantage of the fact that in the limit of low applied field strength, the distortion of the ionic cloud due to the field can be ignored. This means that the ζ calculated from the ion distribution in equilibrium can be assumed to be equal to that of a system subject to a weak applied field, allowing us to perform equilibrium simulations, *i.e.*, with no applied electric field. Using this potential as an input in the SEM numerical solver, we obtain the corresponding electrophoretic mobility. In this manner we take into account ion correlations, crucial in the case of multivalent salt, which are ignored in the PB approach used in the SEM.

We make use of the restricted primitive model, where ions are treated explicitly as charged spheres all having the same size, as shown in Fig. 4.1, and the solvent is considered as a homogeneous dielectric medium having the electric permittivity of water at room temperature. This method is called "primitive" because it ignores the structural details of the fluid, and "restricted" since all ion species have the same size. We simulate mono-, di-, and trivalent salts, with the coions having valency -1 and the counterions valency $z = 1$, 2 or 3, respectively. The system is simulated at different salt ionic strengths, $I = \frac{1}{2}\sum_{i=1}^{N} c_i z_i^2$, where c_i is the molar concentration of the i^{th} salt species and z_i is its valency. In order to find the molar concentrations corresponding to the ionic strength, the relation $c_{\text{coions}} = z c_{\text{counterion}}$ is used. Charge neutrality of the whole system is maintained by inserting additional counterions of valency z to neutralize the charged plate, whose charge density is taken from the experiments. Periodic boundary conditions are applied parallel to the charged plate and the system is confined in the perpendicular direction. The electrostatic interactions are calculated taking into account the contribution from all periodic copies in the $x-y$ plane using the Electrostatic Layer Correction (ELC) method combined with the particle-particle-particle mesh (P3M) algorithm (see subsections 3.4.2 and 3.4.1 for introductions to these methods). The size of the MD box is at least five Debye lengths in the non-periodic direction. In the periodic directions, the minimum of the box size is one Debye length and it is chosen such that the ionic strength is not strongly changed due to the wall counterions.

In addition to the electrostatic interactions, the ions interact via a Weeks-Chandler-Anderson (WCA) potential, introduced in subsection 3.4.3 of chapter 3, with each other as well as with the wall. The unit system is defined by $\sigma_{\text{lj}} = 3.5$ Å, $\varepsilon_{\text{lj}} = \text{k}_{\text{B}}T = \varepsilon_{\text{MD}}$ and putting the mass of all particles to $m = 1m_0$, corresponding to the mass of an ion ($\sim 10^{-26}$ kg). $r_{\text{off}} = 0$ for ion-ion as well as ion-wall interaction and the ion-wall interaction strength is $\varepsilon_{\text{col}} = 4\ \text{k}_{\text{B}}T$. The simulations where we refer to the full Lennard-Jones (LJ) interaction (introduced in subsection 3.4.3) also include an attractive part by setting $r_{\text{cut}} = 2.5\sigma_{\text{lj}}$ and in this case $\varepsilon_{\text{col}} = 4\ \text{k}_{\text{B}}T$ for the trivalent La^{+3} counterions. The Bjerrum length takes on the value $l_{\text{B}} = 2\sigma_{\text{lj}} = 7$ Å which corresponds to water at room temperature. Simulations are performed in the canonical NVT ensemble, using a Langevin thermostat (see subsection 3.3.1) to keep the temperature constant. The time step is $\Delta t = 0.01\tau$ where τ is the unit of time derived from the length, mass and energy units as $\tau = \sigma_{\mathrm{lj}}\sqrt{m/\varepsilon_{\mathrm{lj}}}$. Each system is first equilibrated for at least 10^6 MD steps, assuring that the ion distribution does not change with time, before running eight production simulations with different random number generator seeds for 10^7 MD steps each.

We extract the average ion density and the total integrated charge density as a function of the distance from the wall from the MD simulation data. The reduced electric potential ($\Phi = e\Psi/k_{\mathrm{B}}T$, Ψ being the electric potential) is then calculated via double integration of the latter

$$\frac{\mathrm{d}^2\Phi}{\mathrm{d}z^2} = -\rho/\varepsilon \quad \Rightarrow \quad \Phi(z) = -\frac{1}{\varepsilon}\int\limits_0^z \int\limits_0^{z'} \rho(z'')\,\mathrm{d}z''\,\mathrm{d}z' \tag{4.1}$$

As the SEM requires ζ as an input, we need to first define the shear plane. Due to the absence of explicit water and drag forces, it is not possible to determine directly the position of the shear plane as the location of the no-slip boundary condition. However, the dependence of the no-slip boundary condition as a function of several parameters such as surface corrugation, shear rate, or contact angle has been investigated in many studies (see, e.g., [169–172]), also in the presence of charged surfaces [173]. For hydrophilic surfaces one can safely approximate this boundary with the position of the shear plane [173]. This is applicable to the polystyrene sulfonate colloids which we investigate here since they are hydrophilic due to the presence of sulfonate groups. Note that while in the presence of explicit solvent, the density profile of ions shows marked layering compared to the coarse-grained case, the electrostatic potentials computed in the two cases are very close to each other [173]. Based on the aforementioned studies, a distance slightly larger than one ion diameter from the surface, that encompasses the majority of ions in contact with the surface, should be a good approximation of the position of the slip plane. In our case we have chosen a shear plane at distance $z_{\mathrm{sp}} = 1.5\sigma_{\mathrm{lj}}$ from the wall, corresponding to 5.25 Å. Note that for our interaction definitions, the distance of the closest approach of the center of an ion of diameter σ_{lj} to the wall is approximately σ_{lj}. Thus, at $z_{\mathrm{sp}} = 1.5\sigma_{\mathrm{lj}}$ we take into calculation the ions in the first layer. As shown in the next section, slight changes in the location of the slip plane do not significantly alter the results.

It is worth noting here that despite the fact that the SEM is based on a mean-field theory (PB), we do take the ion correlations into account by obtaining the ζ-potentials from simulations with explicit finite-sized ions. These correlations are crucial in systems with highly charged surfaces and/or multivalent salt.

4.2 Results and Discussions

In this section, the results of the electrophoretic mobility for large colloids with different charge densities, obtained from simulations performed using the method discussed in the previous section, are compared to two different sets of experimental results [4, 5, 174, 175] that have been obtained with very different techniques, but with exactly the same salt molecular composition.

4.2.1 Simulations Vs. Experiments of Semenov et al.

Semenov *et al.* [4, 174, 175] measured the electrophoretic mobility of a single colloid in solutions of varying salt concentration and valency (KCl, $CaCl_2$ and $LaCl_3$) using low applied electric fields to ensure the validity of the linear regime. They use a technique based on optical tweezers to measure the electrophoretic mobility of a *single* colloid. The partially sulfonated polystyrene latex colloids used in their experiments have a diameter of 2.23 μm and a surface charge density of $\sigma_\mathrm{s} = -0.31\ \mu\mathrm{C/cm}^2 \simeq -0.02\ \mathrm{e/nm}^2$, and are considered to have both hydroxyl and carboxyl surface groups. These colloids are much larger than the experimental Debye lengths, and κR is notably larger than one. For the investigated systems we have values $11.6 < \kappa R < 2800$, and therefore the planar approximation should be reasonable over the whole range of salt concentration. To test the validity of this assumption we calculate the $\zeta-$potentials in the monovalent salt case from numerical results of the nonlinear PB in both spherical and planar geometries. Figure 4.2 shows the reduced $\zeta-$potentials as a function of ionic strength. The results for the spherical geometry using different radii are compared with the planar result. As can be seen, the difference between the two geometries decreases by increasing the ionic strength or the radius. For $R > 400$ nm, the two geometries are almost identical over the whole range of ionic strengths. This validates the use of the planar geometry for the mean-field case without an applied electric field. The convective flow and the ionic electric current might change the ion distribution in non-mean-field systems out of equilibrium. We are not able to investigate these changes directly in the simulations which are performed in equilibrium. However, as discussed in description of the SEM in subsection 3.5.2 of chapter 3, all these effects are actually taken into account by the SEM numerical solver. On the other hand, by inserting the $\zeta-$potential obtained from the simulations, we include the important correlations, which are strongest within the shear plane, explicitly and the SEM equations are solved beyond this plane, where the correlations are much weaker. Based on this and the excellent agreement of our results with the experimental data, we believe that the use of the planar geometry is also valid for the non-mean-field cases out of equilibrium. Although, strictly speaking, we have no analytical proof for the validity of this approximation in the non-equilibrium case.

In Fig. 4.3, the experimental electrophoretic mobilities as a function of ionic strength are compared to simulation results for the three different valencies. The reduced mobility reported in this work is defined as $\mu_\mathrm{red} = 3\eta e\mu/(2\varepsilon k_\mathrm{B}T)$. It should be noted here that we use only experimentally measured parameters such as the surface charge density and salt concentration in our simulations and there are no fitting parameters. An exception is in the full LJ trivalent case where we add a specific adsorption potential of 4 $k_\mathrm{B}T$ between the counterions and the surface, as discussed in detail further in this section.

In the monovalent case, our simulation results (blue circles) are in excellent agreement with the numerical PB curves, where the $\zeta-$potentials are obtained from numerical solution to the nonlinear spherical or planar PB equation and converted to electrophoretic mobilities using the O'Brien's formula, Eq. 3.74. These numerical results are shown respectively by the solid blue and dotted red lines in Fig. 4.3. Also shown are the mobilities computed from the simulations ζ-potentials via the Helmholtz-Smoluchowski (HS) equation, Eq. 3.72 (solid black lines). The HS calculations match the simulations only at large ionic strengths where the $\zeta-$potential is low. As discussed in subsection 3.5.1, it is known that the HS formulation is not appropriate

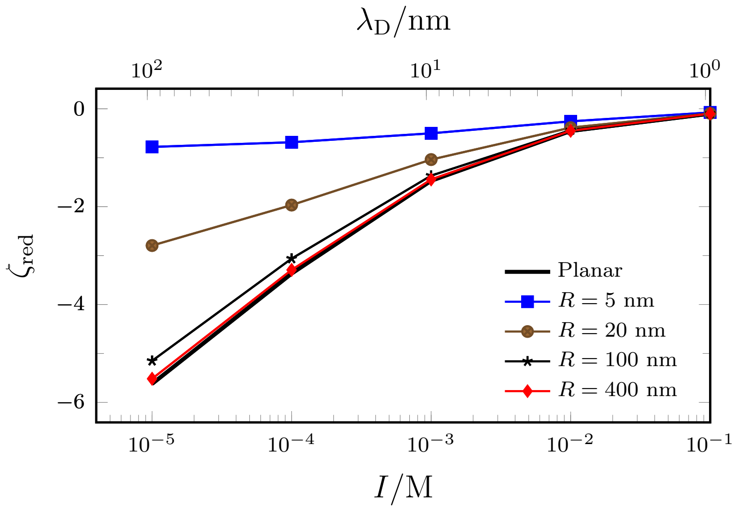

Figure 4.2: Numerically calculated reduced ζ, $\zeta_{\mathrm{red}} = e\zeta/(k_{\mathrm{B}}T)$, as a function of monovalent salt ionic strength I and the corresponding Debye length λ_{D}. The solutions for the spherical geometry with surface charge density $\sigma_{\mathrm{s}} = -0.31\ \mu\mathrm{C/cm}^2 \simeq -0.02\ \mathrm{e/nm}^2$ for different radii R are compared to the solution for the planar geometry. Figure taken from [3].

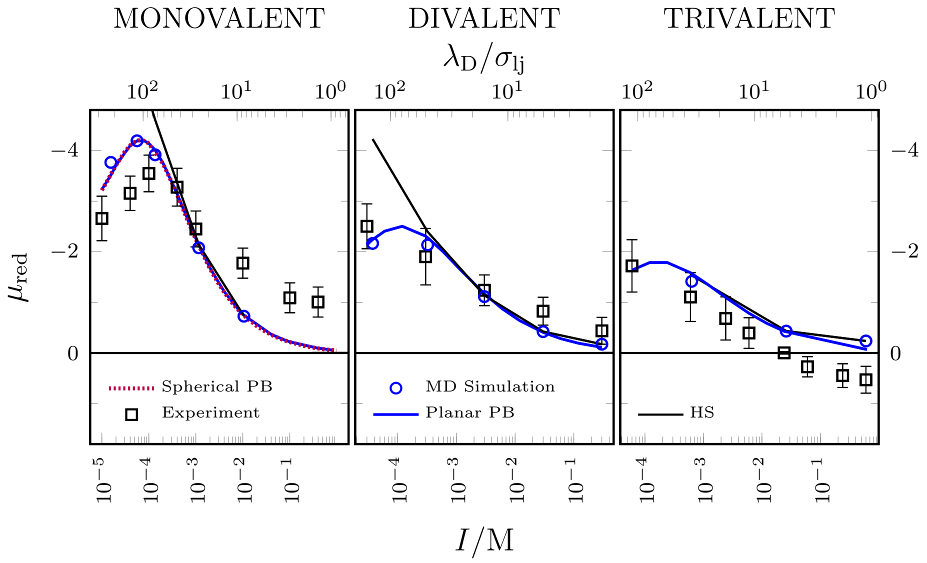

Figure 4.3: Reduced mobility μ_{red} of a latex colloid with surface charge density $\sigma_{\mathrm{s}} = -0.31\ \mu\mathrm{C/cm}^2 \simeq -0.02\ \mathrm{e/nm}^2$ and diameter 2.23 μm as a function of salt ionic strength I, and the corresponding Debye length λ_{D}, for mono-, di-, and trivalent salt. Simulation and experimental results (taken from [4]) are represented via the blue circles and black squares, respectively. Numerical calculations using the nonlinear spherical or planar PB, are shown as red dotted and blue solid lines, respectively. The black solid lines represent the Helmholtz-Smoluchowski equation (Eq. 3.72) using the ζ-potentials obtained from simulations.

for high ζ-potentials ($|\zeta| \gtrsim 2\ k_{\mathrm{B}}T/e \simeq 50\ mV$) since it ignores the surface conductivity and relaxation effects of the EDL. Fig. 4.4 shows the corresponding ζ_{red}-potentials and it is seen that it increases monotonically with decreasing ionic strength and $\zeta_{\mathrm{red}} \simeq -3$ at $I = 0.0001$ M in the monovalent case. The O'Brien approximative expression, on the other hand, takes these effects into account to the first order and the perfect agreement between the simulations and the numerical results in Fig. 4.3, shows that for this set of parameters the ion correlations are negligible. Thus, they can be ignored and the mean-field treatment matches the explicit ion simulations excellently. Furthermore, the numerical results for spherical nonlinear PB is almost identical to that of the planar case, certifying once again the validity of the planar approximation. The results show a mobility maximum of a similar height at roughly the same ionic strength ($I = 5 \times 10^{-5}$ M) as in the experiment and semiquantitative agreement with the experiment is achieved for all values of the ionic strength. The discrepancy between simulation and experiment increases at higher ionic strengths. As discussed later in this section, part of this might be due to systematic errors in the experimental determination of the mobilities.

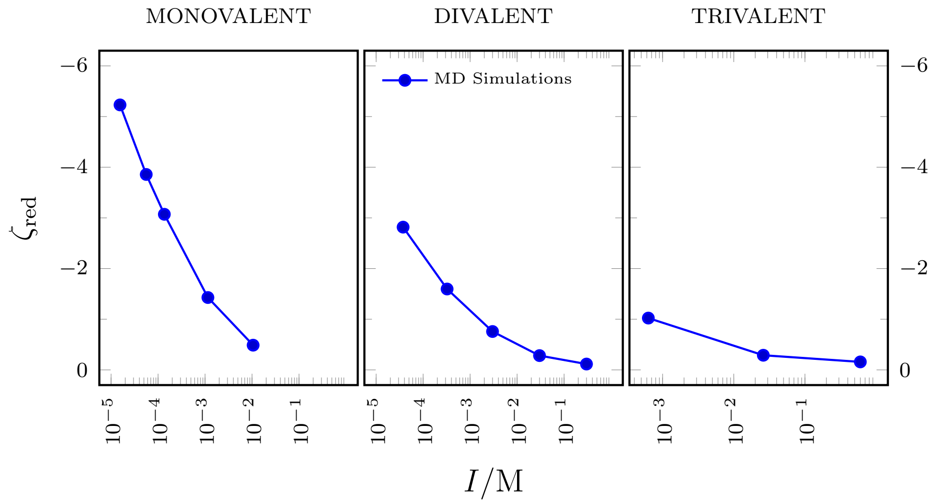

Figure 4.4: Reduced ζ-potential ζ_{red} as a function of ionic strength I obtained from MD simulations. The position of the shear plane is $z_{\mathrm{sp}} = 1.5\sigma_{\mathrm{lj}}$ and data corresponds to the MD simulation electrophoretic mobilities depicted by blue circles in Fig. 4.3.

In the divalent case, shown in the middle panel of Fig. 4.3, we see a semiquantitative agreement between simulation and experiment. Simulation data perfectly matches the results obtained via the numerical solution to the nonlinear planar PB using the O'Brien formula to convert ζ to μ. This indicates that the ion correlations are weak even for divalent ions at this surface charge density. The numerical solutions show a maximum at ionic strength $I \sim 10^{-4}$ M. The agreement of the simulation results with the HS calculations, which use the HS equation (Eq. 3.72) to convert the ζ-potentials obtained from simulation to mobilities, is however limited to high ionic strengths, i.e. small ζ. It is seen in Fig. 4.4 that $|\zeta_{\mathrm{red}}| > 2$ for $I < 0.0001$ M in the divalent case, which explains the discrepancies between HS and simulation mobilities at lower ionic strengths as discussed above.

The experimentally observed mobility reversal in the trivalent case could not be reproduced and the data shown in Fig. 4.3 are thus not even qualitatively correct. The electrostatic interactions *alone* seem to be not strong enough to attract sufficient counterions to the charged surface to produce the experimentally observed mobility reversal. The relative unimportance of the electrostatic correlations is corroborated by the good agreement between simulation and the PB+O'Brien results. The disagreement of the former with PB+HS results at low ionic strength is the consequence of ignoring the surface conductivity effect in HS. As in the divalent case, the PB+O'Brien curve exhibits a maximum around $I = 10^{-4}$ M.

The strong coupling theory of Netz *et al.* [176] also supports the conclusion that the charge inversion necessary for mobility reversal observed here cannot be caused by pure electrostatic interactions. This theory states that the dimensionless Coulomb coupling parameter $\Xi = 2\pi\sigma_s l_B^2 z^3$ needs to be larger than about 10 to produce charge inversion purely by electrostatic effects. For the most strongly coupled system, the trivalent La^{3+} salt system, we have only $\Xi = 1.7$, which is well below the threshold for charge inversion, and consequently mobility reversal through electrostatic interactions alone does not occur. This also explains why the PB curves fit the simulation results so remarkably well.

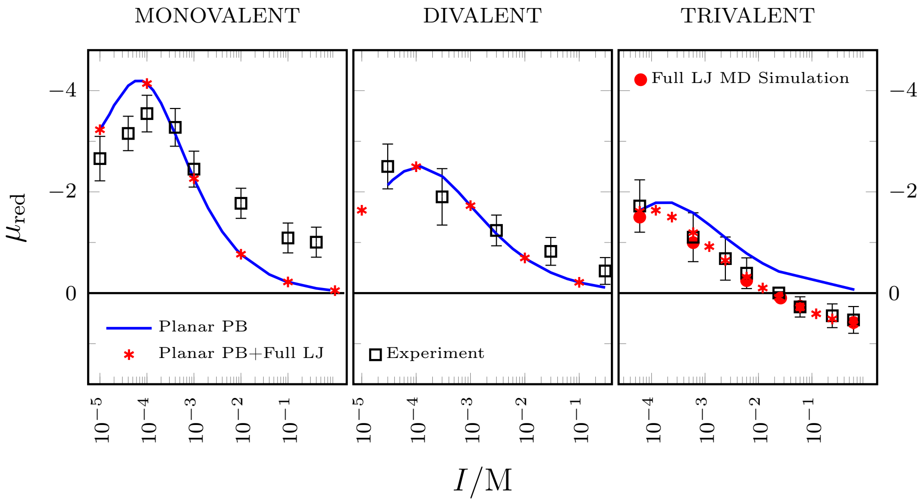

Figure 4.5: Reduced mobility μ_{red} as a function of ionic strength I for mono-, di-, and trivalent salts. The results are obtained by numerically solving the nonlinear planar PB with and without the specific adsorption between the counterions and the surface (blue lines and red symbols respectively). The ζ-potential is converted to μ using Eq. 3.74. The surface charge density is $\sigma_s = -0.31\ \mu\text{C/cm}^2 \simeq -0.02\ \text{e/nm}^2$ as the colloids used in Semenov *et al.*'s experiments [4].

As mentioned in the introduction to this chapter, specific adsorption is considered by some authors to be responsible for charge inversion. To test if it also plays a role here, we replaced the WCA potential between the counterions and the charged surface with a full LJ interaction, described in Sec. 4.1, implying a specific adsorption of the La^{3+} ions on the latex colloid. We used interaction strengths $\varepsilon_{\text{col}} = 2\ k_B T$, and $\varepsilon_{\text{col}} = 4\ k_B T$ for a system at the experimental ionic strength for which the mobility is zero. The two strengths resulted in $\mu_{\text{red}} = -0.31$ and $\mu_{\text{red}} = 0.12$, respectively. Therefore, we chose $\varepsilon_{\text{col}} = 4\ k_B T$ and all the reported results with full LJ use this value for the interaction strength. This is essentially a fitting parameter and is in line with previous studies of colloidal electrophoresis, where a reasonable value for the energy of specific adsorption was found to be a few $k_B T$ [156]. In Fig. 4.6, the potential distribution is shown for

I= 0.6 M, both with and without the full LJ interaction. As can be seen $\zeta-$potential reversal, and consequently mobility reversal, does not occur in the absence of specific adsorption. The effect of this additional attraction on the mobility for all three salt valencies is depicted in Fig. 4.5. The specific adsorption between the counterions and the surface is also taken into account in the nemerical calculations by including the full LJ interaction in the PB equation. In the trivalent case, the simulations with the additional attraction (red circles) match the experiments very good. Since the agreement between PB+O'Brien calculations and simulations are perfect (see Fig. 4.3), we suffice to provide only numerical results in the mono-, and divalent cases. It is seen that extra adsorption does not influence the mono-, and divalent cases since the electrostatic interaction between the counterions and the surface is weak and most of them are not close enough to enter the short-ranged LJ attraction part. Therefore, if existing, the specific adsorption between K^+ and Ca^{2+} cannot be observed here. On the other hand, the full LJ PB calculations in the trivalent case are again in perfect agreement with the simulations showing that the electrostatic correlations are very weak even for higher valency.

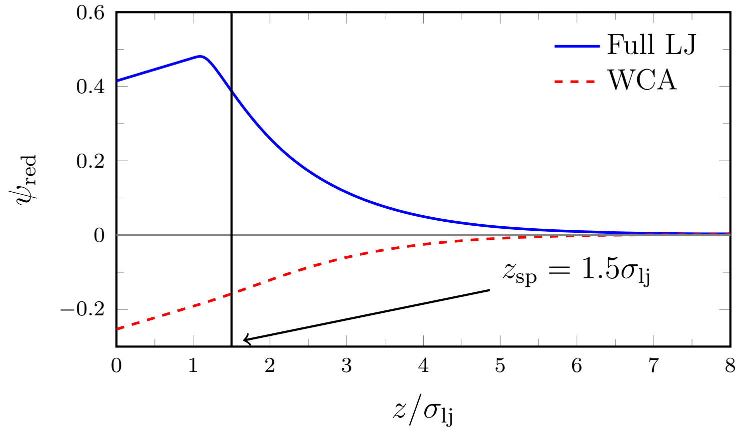

Figure 4.6: Reduced potential, ψ_{red}, as a function of the distance from the surface z for $\sigma_s = -0.31\ \mu\mathrm{C/cm}^2 \simeq -0.02\ \mathrm{e/nm}^2$ and $I = 0.6$ M of trivalent salt with WCA or full LJ interaction between the counterions and the charged surface (red dashed and blue solid lines respectively). The position of the shear plane z_{sp} is marked by the vertical solid black line. Figure also used in [3].

It has been pointed out several times that using a discrete surface charge distribution in simulations can increase the ionic correlations and lead to stronger attraction of the counterions to the surface [177–180]. We found, however, that even the discreteness of the surface charge does not induce a mobility reversal in this system. For this purpose, we simulated the system at $I = 0.026$ M using 100 monovalent charges distributed on a surface of area $A = 200 \times 200\sigma_{\mathrm{lj}}^2$. The discrete charges are modeled as spheres of size $1\sigma_{\mathrm{lj}}$, interacting with all other ions via a WCA potential with $\varepsilon_{\mathrm{col}} = 4\ \mathrm{k_B}T$. Two different distributions were used; in the regular one, the surface charges were fixed at on a square grid of lattice size $20\sigma_{\mathrm{lj}}$. In the second case, the charges were disorderly distributed, having a minimum distance of $2\sigma_{\mathrm{lj}}$. The result is observed in Fig. 4.7 where the total charge density is shown for the different discrete surface charge distributions and compared to those obtained from the homogeneous case with and without the full LJ interaction between the counterions and the wall. Overcharging occurs only in the presence of the additional specific adsorption. The dicretization results in minimal differences

	Disordered discrete (WCA)	Regular discrete (WCA)	Continuous (WCA)	Continuous (full LJ)
$\zeta_{\rm red}$	-0.26	-0.28	-0.29	0.06
$\mu_{\rm red}$	-0.38	-0.42	-0.43	0.1

Table 4.1: Reduced zeta-potential $\zeta_{\rm red}$ and the corresponding reduced mobility $\mu_{\rm red}$ values for an interface with $\sigma_{\rm s} = -0.31\ \mu{\rm C/cm}^2 \simeq -0.02\ {\rm e/nm}^2$ at $I = 0.026$ M of trivalent salt, using different surface charge distribution models in the simulations. The non-electrostatic interaction between the counterions and the interface is mentioned in parentheses. Data used in [4] with the shear plane at $z_{\rm sp} = 1.5\sigma_{\rm lj}$.

to the continuous counterpart, which are slightly larger in the case disorderd distribution. The corresponding reduced ζ-potential and mobility values are listed in Table 4.1.

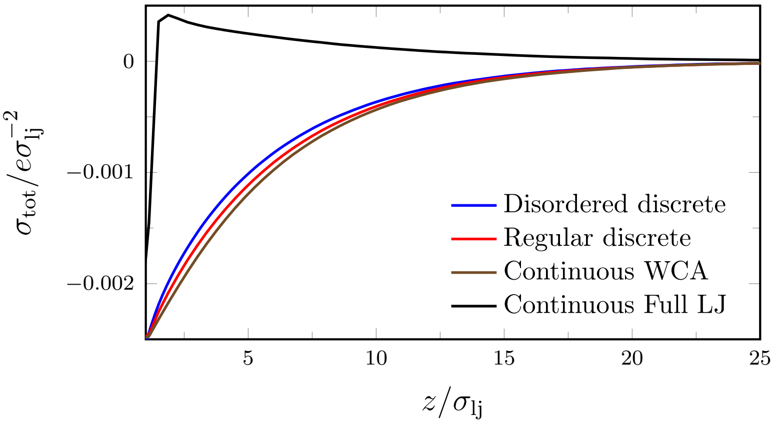

Figure 4.7: Cumulative total surface charge density $\sigma_{\rm tot}$ as a function of the distance from the interface obtained from simulations with $\sigma_{\rm s} = -0.31\ \mu{\rm C/cm}^2 \simeq -0.02\ {\rm e/nm}^2$ at $I = 0.026$ M of trivalent salt for different surface charge distributions on the interface. In addition to electrostatic interactions, there is a WCA potential acting between the counterions and the charged surface in the discrete models between. The corresponding values of $\zeta_{\rm red}$ and $\mu_{\rm red}$ are listed in Table 4.1. Data taken from [4].

The simulations results including the attractive part of the LJ interaction between the counterions and the wall exhibit very good quantitative agreement with the experiment. We also show the reduced mobility curve calculated via the nonlinear planar PB with the additional full LJ interaction in Fig. 4.3. Again, the numerical curve matches our simulation results very well, indicating the weakness of the electrostatic correlations.

In Fig. 4.8 the simulation results for ion densities and the reduced potential are compared to the numerical solutions of the nonlinear planar PB for mono-, di-, and trivalent salt (with and without the specific adsorption) at the specified ionic strengths. The PB equations are modified to include a WCA interaction between the ions and the charged surface. In the trivalent cases where specific adsorption is considered, the interaction between the counterions and the surface is replaced by a full LJ potential with $\varepsilon_{\rm col} = 4\ k_{\rm B}T$. It is seen that in the monovalent case, where ion correlations are negligible, simulation and numerical results match each other perfectly. In the divalent case small deviations are observed due to weak ion correlations, but the overall agreement between is very good. Deviations are observed for the trivalent salt with WCA interaction, due to the ion correlations absent in PB. These correlation effects are not very strong and overwhelmed by the attraction between the counterions and the charged plane when full LJ interaction is used. Only when including the specific ion interaction does the potential inverse sign.

The existence of this specific interaction between La^{+3} and polystyrene latex has also been reported by several other authors [5, 157, 158, 181]. Its origin is suspected to be the hydrolysis of lanthanum; it is known that lanthanum ions hydrolyze around $\mathrm{pH} \simeq 6$ [182, 183] which leads to specific adsorption. Given the fact that despite the explicit presence of ion correlations in our simulations no mobility reversal occurs at the experimentally observed ionic strength without modeling the specific adsorption, we strongly believe that the latter is the key to the reversal in this system. The coarse-grained nature of our model and the absence of explicit water makes it impossible for us to investigate directly the origin of this adsorption and more detailed simulations would be required for this purpose. It is interesting to note that Martín-Molina *et al.* [22] reported mobility reversal of sulfonated polystyrene latex in the presence of La^{3+} ions at $\mathrm{pH} = 5.8$. Using ions correlation theories to explain their results without taking into account specific adsorption, they are able to reproduce the mobility reversal at the same salt concentration as in the experiment. However, the overall agreement between theory and experiment is otherwise poor which might be due to the usage of the Helmholtz-Smoluchowski equation for converting their results to mobilities. The colloids they study possess a much higher charge density ($\sigma_\mathrm{s} = -11.5\ \mu\mathrm{C/cm}^2 \simeq -0.72\ \mathrm{e/nm}^2$) which increases the electrostatic correlations significantly. The Coulomb parameter in their case is $\Xi = 62$.

Finally, as mentioned in the Sec. 4.1, slight changes in the position of the shear plane do not affect the results significantly. This is shown in Fig. 4.9 where the results obtained using two different slip plane positions ($z_\mathrm{sp} = 1.025\sigma_\mathrm{lj}$ and $z_\mathrm{sp} = 1.5\sigma_\mathrm{lj}$) are compared with each other. It is seen that the two cases are almost indistinguishable.

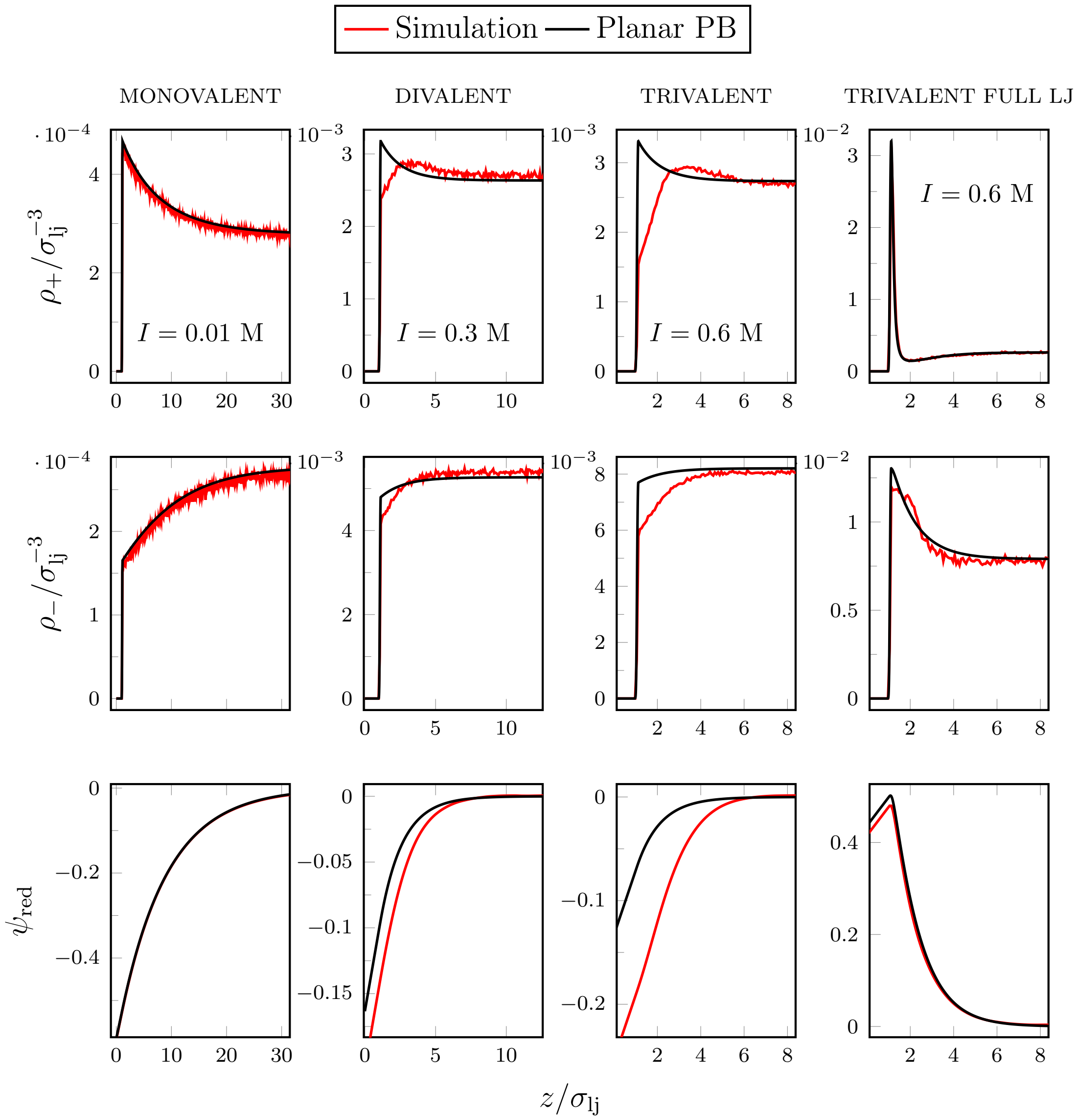

Figure 4.8: Number density of positive and negative ions (ρ_+ and ρ_- respectively) and reduced potential ψ_{red} as a function of the distance z from a surface with surface charge density $\sigma_{\mathrm{s}} = -0.31\ \mu\mathrm{C/cm}^2 \simeq -0.02\ \mathrm{e/nm}^2$ for mono-, di-, and trivalent salt at the stated ionic strengths. The simulation results (red) are compared to the numerical results of planar PB. The non-electrostatic interaction between the counterions and the charged surface is maintained via a WCA potential (Eq. 3.18) except in the furthest right column where a full LJ with $\varepsilon_{\mathrm{col}} = 4\ k_{\mathrm{B}}T$ acts between the trivalent counterions and the interface, both in the simulations and the PB approach.

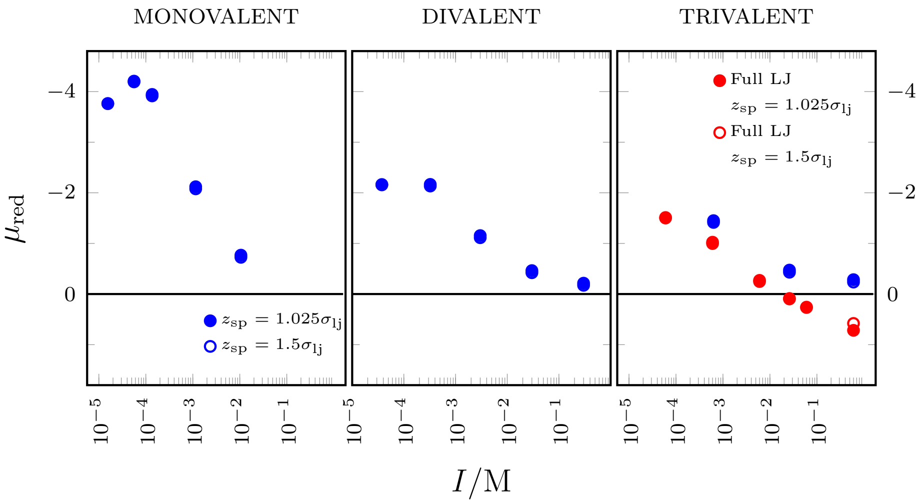

Figure 4.9: Reduced electrophoretic mobility μ_{red} as a function of ionic strength I for monovalent (KCl), divalent (CaCl_2) and trivalent (LaCl_3) salt solutions for latex colloids of diameter 2.23 μm and surface charge density $-0.31\ \mu\text{C/cm}^2 \simeq -0.02\ \text{e/nm}^2$. The results are obtained from MD simulations, in the absence of an applied field, combined with the SEM. Results obtained with WCA interaction are represented by blue circles (full circles for $z_{\text{sp}} = 1.025\sigma_{\text{lj}}$ and empty ones for $z_{\text{sp}} = 1.5\sigma_{\text{lj}}$) whereas the results using full LJ interaction in the trivalent case is shown via red circles (full circles for $z_{\text{sp}} = 1.025\sigma_{\text{lj}}$ and empty ones for $z_{\text{sp}} = 1.5\sigma_{\text{lj}}$). Figure taken from [3].

4.2.2 Simulations Vs. Experiments of Elimelech et al.

Elimelech *et al.* [5] have also performed experiments where they measure electrophoretic mobilities of latex colloids in mono-, di- and trivalent salt (KCl, CaCl_2 and LaCl_3, respectively) as a function of ionic strength using a Mark II microelectrophoresis apparatus. We compare our simulation results to their experimental data for a colloid of diameter 0.753 μm and surface charge density $\sigma_s = -5.64\ \mu\text{C/cm}^2 \simeq -0.35\ \text{e/nm}^2$. Due to the large size of the colloid in comparison to the Debye length in the considered range of salt concentrations, $12 < \kappa R < 391$, the planar geometry inherent in our simulation technique is also appropriate for this system. This assumption is verified by comparing numerical results for the planar case with that of spheres of different radii having the same surface charge density as illustrated in Fig. 4.10. Here, the planar geometry is an acceptable approximation even for the smallest sphere ($R = 5$ nm) at low salt concentrations. For $R > 20$ nm the planar and spherical results are almost identical. The reason why in this case the planar geometry becomes applicable for smaller spherical particles in comparison to the previous case shown in Fig. 4.2, is the higher surface charge density of the particle. As the counterion densities in Fig. 4.11 show, the surface with higher charge density attracts more counterions to the close vicinity of the surface where the geometry can be considered as planar. This implies that κR is not the only criterion for the validity of this approximation. At low surface charge densities where $\psi_{\text{red}} \ll 1$, Eq. 3.44 can be linearized and the Debye-Hückel limit applies in which the scaling of the potential distributions in the spherical and planar geometry differ by a factor of $1/r$. This is not the case at high surface charge densities, i.e., high surface potentials. The large accumulation of counterions close to the interface causes the nonlinear part of the PBE to dominate, reducing the difference between the planar and spherical geometries. In Fig. 4.11, the potentials for both the spherical and planar cases are also compared for the low and high surface charge densities mentioned above.

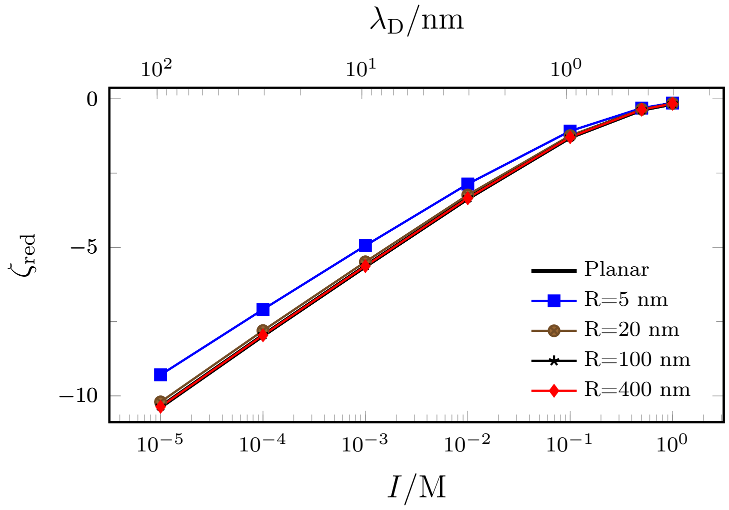

Figure 4.10: Numerically calculated reduced $\zeta-$potentials, $\zeta_{\mathrm{red}} = e\zeta/(k_{\mathrm{B}}T)$, as a function of monovalent salt ionic strength I and the corresponding Debye length λ_{D}. The solutions for the spherical geometry with surface charge density $\sigma_{\mathrm{s}} = -5.64\ \mu\mathrm{C/cm}^2 \simeq -0.35\ \mathrm{e/nm}^2$ for different radii R are compared to the solution for the planar geometry.

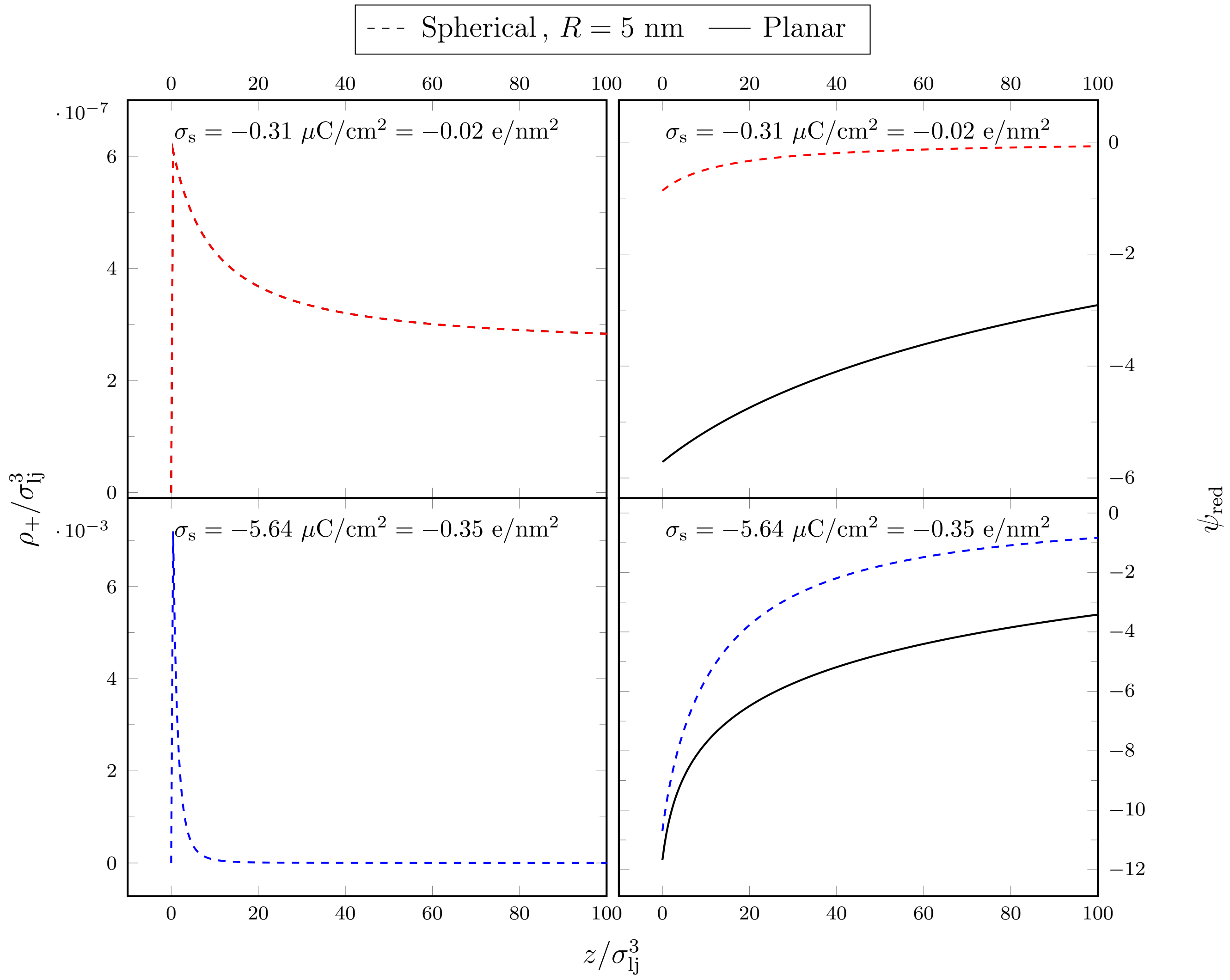

Figure 4.11: Counterion number density ρ_+ and reduced potential ψ_{red}, obtained from numerical solution to the nonlinear PBE, as a function of the distance from a surface with the specified surface charge density σ_s at $I = 1e - 5$ M of monovalent salt. The dashed lines indicate spherical geometry with radius $R = 5$ nm and the solid lines correspond to planar geometry.

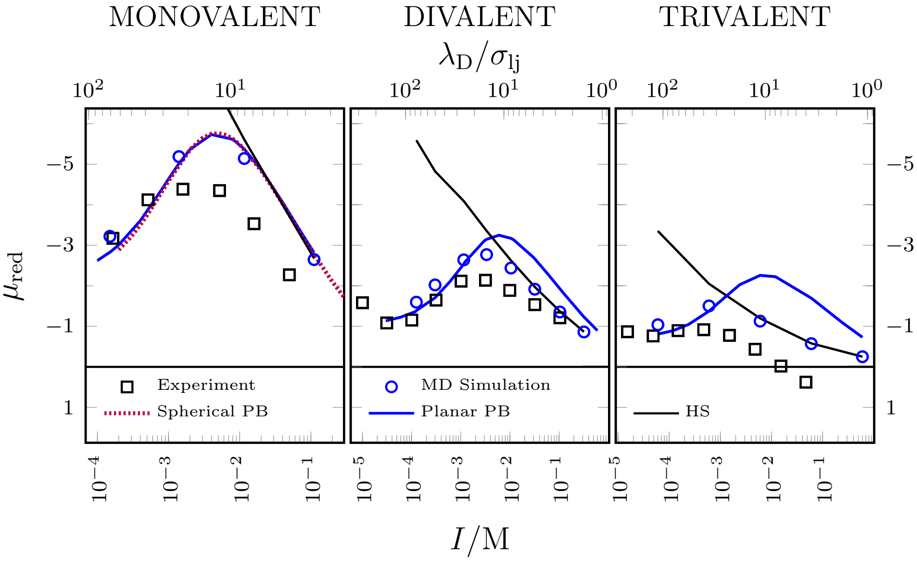

Figure 4.12: Reduced mobility μ_{red} of a latex colloid with surface charge density $\sigma_{\mathrm{s}} = -5.64\ \mu\mathrm{C/cm}^2 \simeq -0.35\ \mathrm{e/nm}^2$ and diameter 0.753 μm as a function of salt ionic strength I, and the corresponding Debye length λ_{D}, for mono-, di-, and trivalent salt. Simulation and experimental results (taken from [5]) are represented via the blue circles and black squares, respectively. Numerical calculations using the nonlinear spherical or planar PB, are shown as red dotted and blue solid lines, respectively. The black solid lines represent the Helmholtz-Smoluchowski equation (Eq. 3.72) using the ζ-potentials obtained from simulations.

The mobility results are shown in Fig. 4.12. For the monovalent case there is a fairly good qualitative agreement between the simulation results and the experiments of Elimelech *et al.* Importantly, the simulations reproduce the peak in the mobility at roughly the same value of the ionic strength as the experimental data. This peak is shifted towards higher ionic strengths, about 100 times higher compared to the data from Semenov *et al.* (Fig. 4.3). Given that the colloids in this case are about three times smaller, this means that the peak occurs not only at higher ionic strengths, but also at about three times larger κR. This shift is due to the higher charge density of the colloid and in line with the findings of Antonietti and Vorweg [184]. Calculating the $\zeta-$potentials from the solution to the nonlinear planar and spherical PB, and using the O'Brien formula, Eq. 3.74 to convert them to mobilities, we again find superb agreement between the two geometries. These numerical curves are also in good agreement with the simulation results except for the two points of lowest salt concentration. The deviation seems to increase with decreasing ionic strength which we believe is due to the increased ionic correlations between ions very close to the colloid that are taken into account in our simulations, but ignored in the PB theory. It is known that mean-field theory is only exact in the weak coupling regime, $\Xi \ll 1$ but it breaks down in the strong coupling limit, when $\Xi \gg 1$ and the Gouy-Chapman length, $l_{\mathrm{GC}} = 1/(2\pi z \sigma_{\mathrm{s}} l_{\mathrm{B}})$, $\kappa l_{\mathrm{GC}} < 1$. Since here $l_{\mathrm{GC}} \simeq 6.45$ Å, hence $0.02 < \kappa l_{\mathrm{GC}} < 0.6$, and $\Xi = 1.13$ some slight deviations from mean-field theory are expected [185–187]. Using the HS equation, Eq. 3.72 to convert the ζ-potentials obtained from simulations to μ (black solid line), the agreement with simulation is limited to the highest ionic strengths where the ζ is relatively small. It is known that HS is only exact for $|\zeta| \lesssim 2\ k_{\mathrm{B}}T/e \simeq 50\ mV$ and at higher ζ, i.e. lower ionic strengths, the neglect of relaxation effects leads to large deviations. The corresponding reduced ζ-potentials shown in Fig. 4.13

reveal that in the monovalent case $\zeta_{\rm red}$ exceeds this value for $I < 0.1$ M which is much larger than it is in the case Semenov *et al.*'s system (see Fig. 4.4) due to the higher surface charge density.

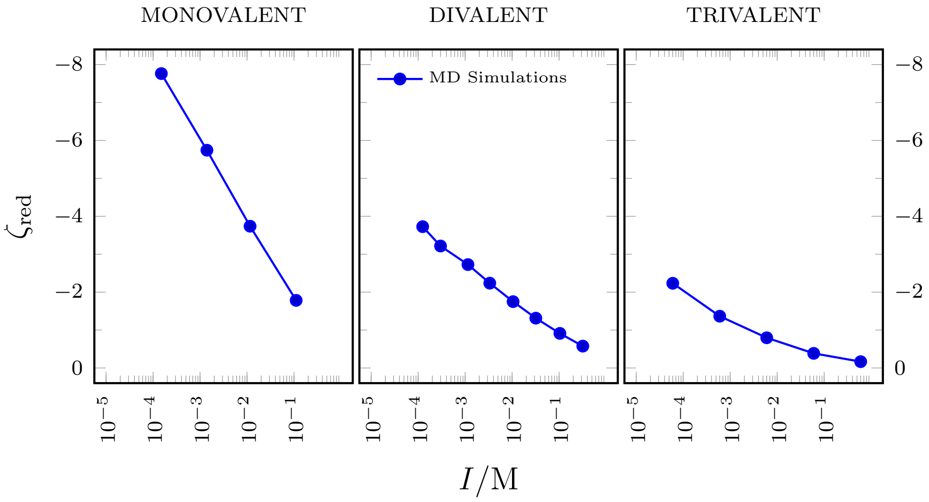

Figure 4.13: Reduced ζ-potential $\zeta_{\rm red}$ as a function of ionic strength I obtained from MD simulations. The position of the shear plane is $z_{\rm sp} = 1.5\sigma_{\rm lj}$ and data corresponds to the MD simulation electrophoretic mobilities depicted by blue circles in Fig. 4.12.

The divalent data in Fig. 4.12 also shows good agreement between our simulations and the experimental results. In contrast to the previous experimental set (Fig. 4.3), the divalent numerical calculations (blue solid curve) match the simulations only qualitatively. Most notably at higher ionic strengths there is a systematic overestimation of the mobility. This is the result of stronger ion correlations in this system due to the higher surface charge density (more than 10 times higher than in the Semenov *et al.*'s experiments), which are not captured by PB. It should be noted that the good agreement between simulation and numerical results for low ionic strengths is partly due to the fact that the $\mu - \zeta$ curves are non-monotonic and show a maximum around this $\zeta-$potential. More specifically, in the case of $I = 0.003$ M the difference between the $\zeta-$potential obtained from simulation and PB is about 25%, but the nonlinearity of mobility as a function of $\zeta-$potential results in smaller deviations in mobility, in this case about 10%, see Fig. 4.14. The non-monotonicity of the mobility as a function of $\zeta-$potential is related to surface conductivity and relaxation effect. The excess charge in the EDL can move in and out of the layer under the influence of the applied electric field, creating an excess electric conduction referred to as the surface conduction [100]. As a result, the ionic cloud deforms and an electric field is generated in the opposite direction as the applied field which slows down the particle. Furthermore, the surface conductivity results in a concentration polarization in the bulk, which in turn affects the electrophoretic mobility by establishing a chemiosmotic flow opposing the electroosmotic flow [188]. The effect of the surface conductivity becomes considerable for large ζ ($|\zeta_{\rm red}| \gtrsim 2$, say) and thin Debye layers, which leads to the non-monotonicity of the $\mu - \zeta$.

This combination of colloidal diameter and surface charge density produces a maximum in the mobility for the divalent case. Our simulation results reproduce this maximum at approximately the same value of the ionic strength as seen in experiment. In Fig. 4.12 we get quite accurate values for low ionic strengths while we systematically overestimate the experimental

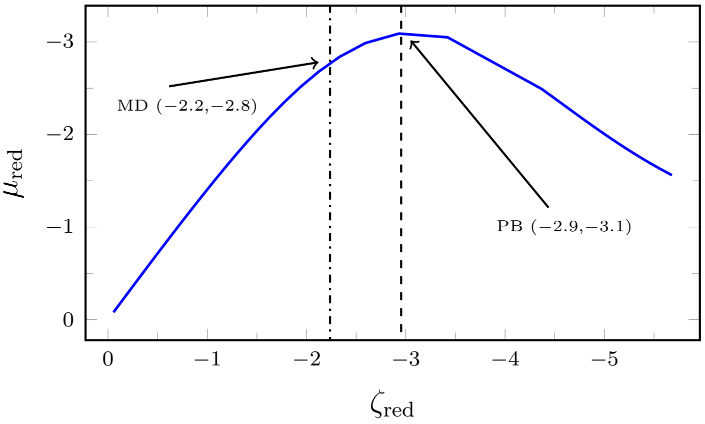

Figure 4.14: Reduced mobility μ_{red} as a function of the reduced $\zeta-$potential ζ_{red} for a spherical colloid of diameter 0.753 μm in $I = 0.003$ M of divalent salt calculated via the SEM numerical solver. The dashed line corresponds to the $\zeta-$potential obtained via numerically solution of the nonlinear planar PB for surface charge density $\sigma_{\text{s}} = -5.64\ \mu\text{C/cm}^2 \simeq -0.35\ \text{e/nm}^2$. The dot-dashed line marks the ζ-potential obtained from equilibrium MD simulations (i.e. no applied electric field) of a plane with the same charge density. The non-monotonicity of the $\mu - \zeta$ curve results in a mobility difference ($\sim 10\%$) much smaller than the corresponding $\zeta-$potential difference ($\sim 25\%$). Figure taken from [3].

mobility values at high ionic strengths. This systematic overestimation of the mobilities at high ionic strength appears both in the mono- and divalent cases, and is in contrast to the results in Fig. 4.3, where we overestimate the mobility at low ionic strengths and underestimate it at high ionic strengths. In the absence of a better explanation we speculate that at least some of the discrepancy could be due to systematic errors of the experiments. The agreement between the HS calculations (black solid line) and simulation breaks down at moderate to low ionic strengths. This can be explained by the corresponding ζ_{res} data depicted in Fig. 4.13 and noting that $\zeta_{\text{red}} > 2$ for $I < 0.02$ M. The considerable effect of relaxation at high ζ which is ignored by the HS equation leads to the observed discrepancies in the mobilities.

The trivalent simulation results in Fig. 4.12 show a strong resemblance to the previously presented data for Semenov *et al.*'s system in Fig. 4.3. No mobility reversal is observed, indicating that also for this system, the electrostatic correlations *alone* are not strong enough to cause a mobility reversal. The discrepancy between the numerical calculations (the blue solid line) and the simulation data is larger than it is in the divalent case due to stronger correlations absent in the mean-field theory. As noted above, the good agreement between the two results at low ionic strengths partly stems from the nonmonotonicity of μ with respect to ζ as a result of surface condutivity and relaxation effects. The black curve, depicting the mobilities computed from simulation ζ-potentials via HS equation (Eq. 3.74), again matches the simulation only at high ionic strength. The corresponding ζ_{red} data shown in Fig. 4.13 are only slightly larger than 2 for the lowest ionic strength, but the stronger electrostatic interactions of the trivalent ions cause the relaxation effect to be significant at smaller ζ-potentials than in the mono- and divalent cases.

The effect of including the additional specific attraction as done in the case of Semenov et al.'s system, is shown in Fig. 4.15. Remarkably, the same attractive interaction of 4 $\text{k}_{\text{B}}T$ be-

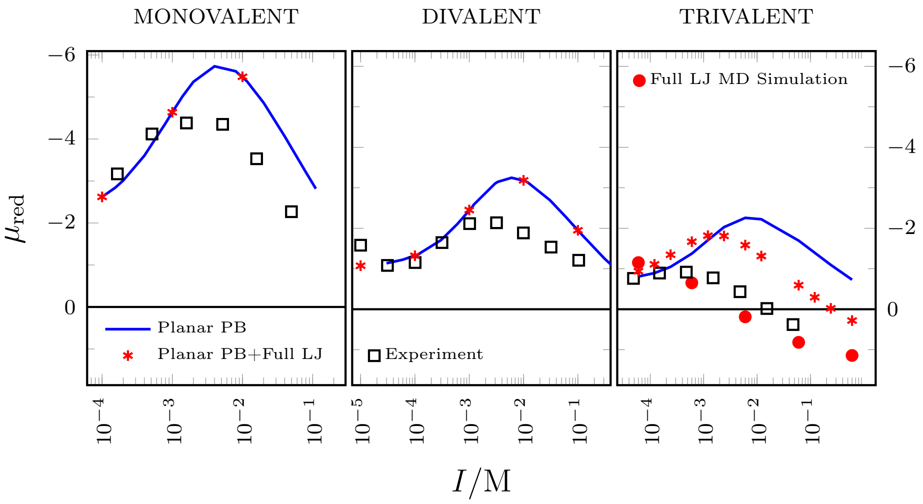

Figure 4.15: Reduced mobility μ_{red} as a function of ionic strength I for mono-, di-, and trivalent salts. The results are obtained by numerically solving the nonlinear planar PB with and without the specific adsorption between the counterions and the surface (blue lines and red symbols respectively). The ζ-potential is converted to μ using Eq. 3.74. The surface charge density is $\sigma_s = -5.64\ \mu\text{C/cm}^2 \simeq -0.35\ \text{e/nm}^2$ as the colloids used in Elimelech *et al.*'s experiments [5].

tween the counterions and the surface again yields an excellent agreement between simulation (red circles) and the experimental data, suggesting that our added potential stems from an underlying specific physical interaction for La^{3+}. Including the full LJ interaction between the counterions and the surface in the nonlinear planar PB (red asterisks), a mobility reversal is obtained at $I \sim 0.3$ M, about ten times higher than the ionic strength for which mobility reversal is observed in the experiment. This is a consequence of ignoring the important ion correlations in the mean-field theory which results in fewer counterions near the surface, and thus higher ζ-potential. The PB results both with and without the LJ attraction show a maximum in the mobility around $I \sim 10^{-3}$ M in the trivalent case. In the mono- and divalent cases, we have again sufficed to numerical calculations to investigate the effect of the extra attraction between the counterions and the surface. This is justified by the excellent agreement between simulation and PB+O'Brien for the monovalent, and the acceptable agreement for divalent salt, see Fig. 4.12. The additional attraction seems to have a negligible influence on the mobility for these valencies, rendering our ability to further hypothesizing its existence.

In order to assure that surface charge discreteness does not result in mobility reversal in this system without the specific adsorption, we used two different types of discrete surface charge distribution in the presence of 0.06 M of trivalent salt; regular and disordered. For the first case, 484 monovalent charges were regularly distributed over a square grid of lattice size of about $4.8\sigma_{\text{lj}}$. In the second case, the same number of surface charges were disorderly distributed over the surface with a minimum distance of $2\sigma_{\text{lj}}$. In both cases, the surface charges have a diameter of $1\sigma_{\text{lj}}$ and interact only via the WCA potential and electrostatic interactions with the free ions. The area of the surface is chosen to be about $105 \times 105\sigma_{\text{lj}}^2$, giving rise to the experimental surface charge density. The integrated surface charge density profile computed from the two discrete charge distributions are compared to the corresponding results of continuous surface charge, both with and without the additional LJ attraction, in

	Disordered discrete (WCA)	Regular discrete (WCA)	Continuous (WCA)	Continuous (full LJ)
ζ_{red}	-0.28	-0.35	-0.38	0.55
μ_{red}	-0.41	-0.51	-0.57	0.82

Table 4.2: Reduced zeta-potential ζ_{red}, and the corresponding reduced mobility μ_{red} values for an interface with $\sigma_{\mathrm{s}} = -5.64\ \mu\mathrm{C/cm}^2 \simeq -0.35\ \mathrm{e/nm}^2$ at $I = 0.06$ M of trivalent salt, using different surface charge distribution models in the simulations. The non-electrostatic interaction between the counterions and the interface is mentioned in parentheses. Data used in [3].

Fig. 4.16. It is clearly seen that the discreteness of the surface charge distribution does not have a significant impact on the results and the additional LJ attraction is indeed required in order to reproduce the experimentally observed mobility reversal. The values of the $\zeta-$potentials and the corresponding electrophoretic mobilities are listed in Table 4.2.

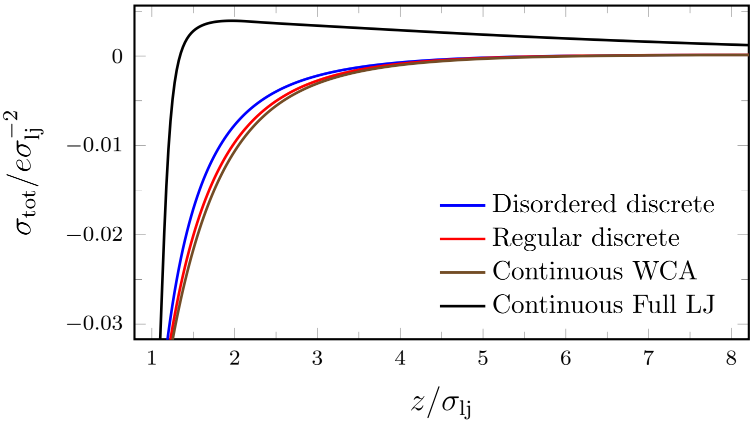

Figure 4.16: Cumulative total surface charge density σ_{tot} as a function of the distance to the interface z obtained from simulations with $\sigma_{\mathrm{s}} = -5.64\ \mu\mathrm{C/cm}^2 \simeq -0.35\ \mathrm{e/nm}^2$ at $I = 0.06$ M of trivalent salt for different surface charge distributions on the interface. In addition to electrostatic interactions, there is a WCA potential acting between the counterions and the charged surface in the discrete models. The corresponding values of ζ_{red} and μ_{red} are listed in Table 4.2. Data taken from [3].

The comparison between simulation results and numerical solution to the nonlinear planar PB for ion densities and the reduced potential is shown in Fig. 4.17. As in the cases presented in Fig. 4.8, the PB equation is modified to include a WCA interaction between the ions and the charged surface. In the trivalent case, a full LJ potential with $\varepsilon_{\mathrm{col}} = 4\ k_{\mathrm{B}}T$ is set between the counterions and the wall when specific adsorption is considered. The ionic correlations are negligible in monovalent salt at $I = 0.1$ M and the simulation results match the PB calculations perfectly. For divalent salt at, the effect of correlations is larger than it was for Semenov *et al.*'s system (see Fig. 4.8) since the surface charge density is much higher. This leads to some deviations between simulation and numerical results which become more evident in the trivalent case. In contrast to the system investigated in the previous section, here the deviations are not overwhelmed by the inclusion of the full LJ interaction between the counterions and the surface due to the higher surface charge density. As discussed above, the Coulombic correlations are much stronger for this system than in the case of Semenov *et* *al.*, but still not strong enough to explain the observed mobility reversal *alone*.

The authors in [143] used hypernetted chain/mean-spherical approximation (HNC/MSA), which includes electrostatic and excluded volume correlation effects, to fit the experimental data of Elimelech *et al.* [5] for the trivalent salt. While being able to observe a mobility reversal, they obtain only qualitative agreement with the experimental results. The mobility reversal predicted by their theory occurs at much higher salt concentrations compared to the experiment. In fact, their results are very much comparable to our MD simulations in the absence of the full LJ interaction. Extrapolating our WCA results to higher ionic strengths would also produce a mobility reversal at an ionic strength greater than 1 M. This strongly supports our argument that *pure* electrostatic correlations are not strong enough to cause mobility reversal at the experimentally observed ionic strength in the system under study and an *additional* specific adsorption term is required.

It is interesting to mention that the coupling parameter, in this case is $\Xi = 30$ and, as discussed before, electrostatic interactions can lead to overcharging for $\Xi > 10$. This might sound contradictory, but as shown in Fig. 4.18, the system *is* overcharged at high ionic strengths, yet the $\zeta-$potential does not change sign, and thus no mobility reversal occurs. This shows that although the reversal of the electrophoretic mobility is related to the overcharging of the particle, overcharging does not always lead to mobility reversal. All-atom MD simulations have shown similar behavior for DNA [189]. The electrophoretic mobility of the DNA reverses at high concentrations of trivalent (spermidine^{3+}) and quadrivalent (spermine^{4+}) salt, whereas charge inversion can occur at lower concentrations. For divalent salt (Mg^{2+}), only charge inversion of the DNA is observed. The mobility reversal of the DNA is demonstrated to be a complex interplay of electrostatics and hydrodynamics; charge inversion is characterized by the change of sign of the cumulative radial charge density, that is the sum over all ions within a certain distance. It is clear that the *whole* charge of each ion contributes to the sum. Mobility reversal, on the other hand, is due to the electro-osmotic flow generated by the counterions which applies a shear force on the DNA. If this force is strong enough, the DNA will change direction. Since only a fraction of the counterions' momentum is transfered to the DNA, it can happen that despite overcharging the mobility does not reverse.

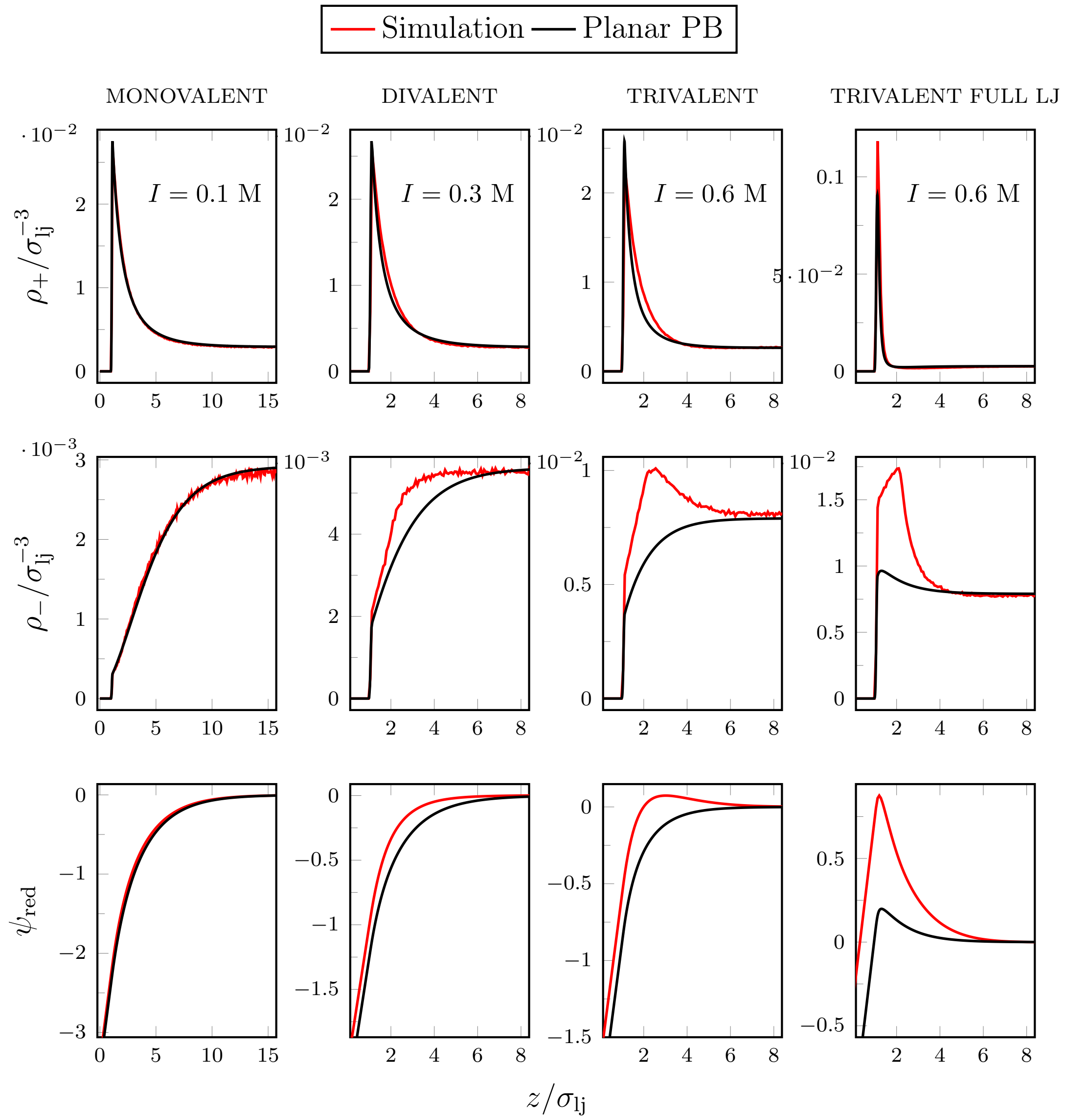

Figure 4.17: Number density of positive and negative ions (ρ_+ and ρ_- respectively) and reduced potential ψ_{red} as a function of the distance z from a surface with surface charge density $\sigma_{\text{s}} = -5.64$ μC/cm^2 $\simeq -0.35$ e/nm^2 for mono-, di-, and trivalent salt at the stated ionic strength. The simulation results (red) are compared to the numerical results of planar PB. The non-electrostatic interaction between the counterions and the charged surface is maintained via a WCA potential (Eq. 3.18) except in the furthest right column where a full LJ with $\varepsilon_{\text{col}} = 4$ $k_{\text{B}}T$ acts between the trivalent counterions and the interface, both in the simulations and the PB approach.

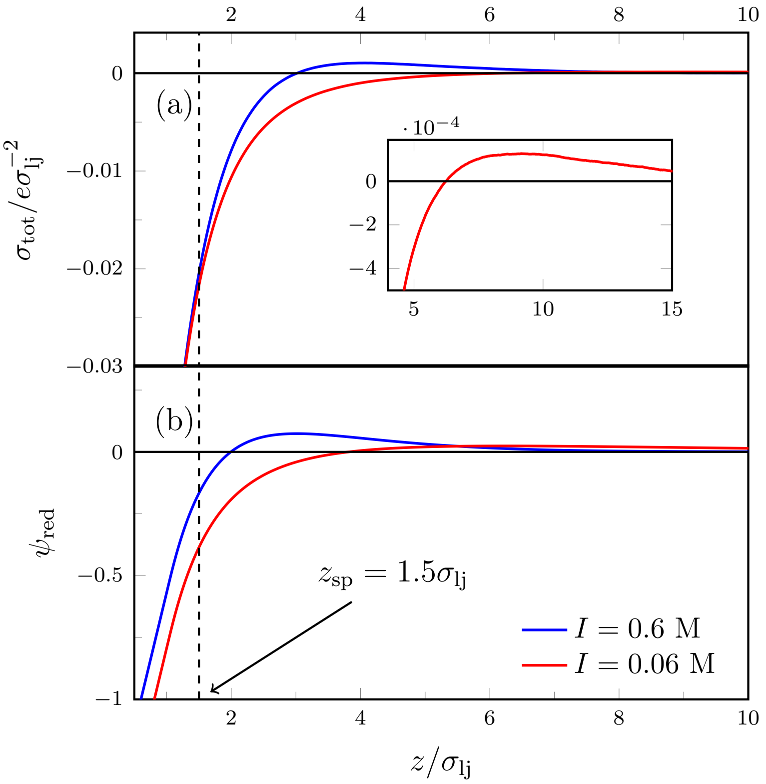

Figure 4.18: (a) Cumulative total surface charge density σ_{tot}, and (b) reduced potential ψ_{red} as a function of the distance from the surface z for $\sigma_{\mathrm{s}} = -5.64\ \mu\mathrm{C/cm}^2 \simeq -0.35\ \mathrm{e/nm}^2$ and trivalent salt of stated ionic strengths. The position of the shear plane is marked by the dashed vertical line. The inset in (a) shows a close up. Data also used in [3].

4.3 Summary

In this chapter, I presented in detail a novel method for studying the electrophoretic mobility of colloids whose radii are much larger than the Debye length. The method represents a unique approach to predicting the electrophoretic mobility of colloids in electrolytic solutions of different valencies for colloids with diameters from 100 nm up to the order of micrometers. While this is the regime in which most experiments are conducted, most of the existing methods used to model colloidal electrophoresis are incapable of capturing it. In the method presented here, this problem is circumvented by taking advantage of the usability of the planar geometry in such cases. First the ζ-potential of the colloids was calculated by means of equilibrium (i.e., no applied electric field) MD simulations of the restricted primitive model using a planar geometry. This $\zeta-$potential was then used as an input into the SEM continuum description to extract the corresponding mobility.

The electrophoretic mobility of large colloids ($\kappa R \gg 1$) was computed in salt solutions of varying valency and concentration. The results were compared to two independent sets of experimental results [4, 5, 174, 175] for latex colloids in mono- (KCl), di- ($CaCl_2$), and trivalent ($LaCl_3$) salt and good agreement was found between our simulations and experimental data. The results demonstrate the validity and usefulness of the planar approximation for studying the electrophoretic behavior of colloids whose radii are much larger than the Debye length, where modeling the whole colloid still remains far beyond what is possible using modern supercomputers. Furthermore, the good agreement between simulation results and experimental data shows that the SEM can be used to obtain the electrophoretic mobility in the presence of multivalent salt, given that the important ion correlations are taken into account when calculating the $\zeta-$potential.

It was further shown that in the trivalent cases considered here, electrostatic attraction *alone* is not enough to reproduce the experimentally observed mobility reversal of latex colloids in the presence of La^{3+} ions and an additional attractive LJ potential acting between the counterions and the colloidal surface is needed. This further supports the existence of ion-specific adsorption between La^{3+} ions and latex colloids which has also been suggested by several other authors [5, 157, 181]. The effect of the additional attraction in the mono- and divalent cases was investigated via numerical calculations and was found to be negligible in both systems.

Furthermore, an example for the system with higher surface charge density and trivalent salt was provided where the surface is overcharged by the counterions in its vicinity but no mobility reversal occurs, revealing that overcharging does not always lead to mobility reversal.

Numerical solutions to the nonlinear PB equation were used to check the validity of the planar approximation and also to compare mobility results obtained from numerically-calculated $\zeta-$potentials with simulations. For low surface charge densities, the effect of ion correlations is negligible and only causes slight deviations in the case of trivalent salt. This is not the case for high surface charge densities were ion correlations play an important role and cannot be disregarded. The comparison between theory and simulation shows these effects clearly in ion densities and potential profiles.

5 Electrophoretic Mobility of Soft Colloids in Monovalent Salt Solutions

Electro-osmotic flow (EOF) plays a crucial role in the electrokinetic behavior of soft colloids, introduced in subsection 3.5.3, where the charges on the polyelectrolytes contribute more to the overall EOF than the surface charges whose EOF is screened by the polymer coating [6, 120, 122, 125, 190–193]. A very interesting and counterintuitive phenomenon observed in electrophoresis, is the non-zero electrophoretic mobility (or non-zero EOF in case of stationary objects) of net neutral objects [42, 190, 194–197]. Notably, in the field of induced-charge electroosmosis (ICEO) electrodes bearing no net charge have been used in order to pump fluid in micro- and nanofluidic devices [198]. Since the charges on the electrodes are induced there is no net charge on the electrodes, which, if they are asymmetric, nevertheless generate a net EOF. This effect has been shown to be enhanced by the production of structured three-dimensional (3D) electrodes in which one section is elevated creating a "conveyor-belt" effect. Similar phenomena are known for the case of polyelectrolyte-grafted surfaces; the coating changes the electrokinetic properties of the surface and results in the electrophoretic movement of a net-neutral object [190]. Grafted polymers are also often used as a means of controlling the EOF to optimize the resolution by grafting either charged or uncharged polymers to the surface of capillaries [199–201].

In this section, MD simulation results of the electrophoretic mobility of spherical soft colloids are presented. Both net-neutral and charged soft colloids are considered and the effect of charge and salt concentration on their mobility is investigated. The results are compared by the numerical solutions to the modified electrokinetic equations presented in subsection 3.5.1, and approximate analytic expressions. Also the validity of the theoretical predictions discussed in subsection 3.5.4 is tested through simulations.

Most of the material of this section is directly taken from publications [190, 202].

5.1 Simulation Method

We perform coarse-grained MD simulations in the canonical (isothermal-isochoric) ensemble (NVT) using the Extensible Simulation Package for Research on Soft matter (ESPResSo) [168, 203]. The simulations are carried out in a periodic box of length $L = 48\sigma_{\text{lj}}$, where σ_{lj} is the fundamental MD length scale. The application of periodic boundary conditions introduces some finite size effects since both electrostatic and hydrodynamic interactions present in this system are long-ranged and the image particles can interact with each other. But here due to the existence of salt and the charge neutrality outside the Debye layer, these interactions are

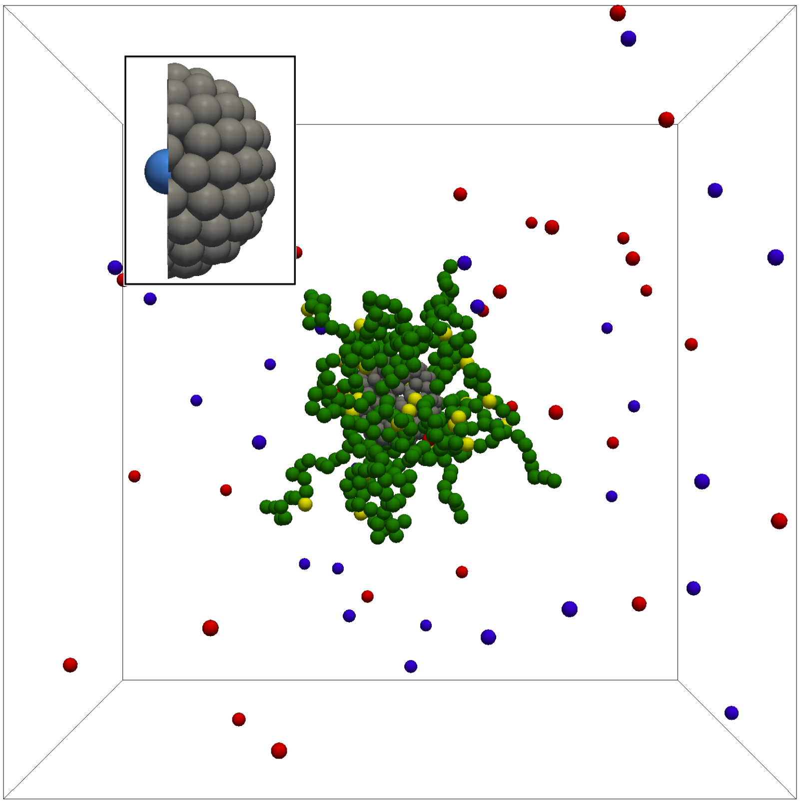

Figure 5.1: An MD snapshot of a net-neutral soft colloid at monovalent salt concentration $c_{\mathrm{s}} = 0.1$ M. Gray spheres represent the colloidal core, green beads are the neutral monomers, and the yellow ones are the charged monomers. The positive and negative ions are depicted via red and blue spheres, respectively. The inset shows a closeup of the colloidal core cut in half with the (negatively charged) central bead in blue.

screened on longer length scales. It has been shown that in electrophoresis, the far-field fluid velocity decays as $1/L^3$ as opposed to the $1/L$ decay in systems not including charges [161, 204]. Therefore, as long as the sum of the Debye length and the hydrodynamic radius of the soft colloid, R_H, is smaller than $L/2$, the finite size effects are negligible. As will become clear in the course of the discussions, for our parameters the finite size effects only play a role at the lowest salt concentration considered. Even there, the existence of counterions reduces the effect of finite box size.

The fundamental MD energy and length units are $\varepsilon = k_\mathrm{B}T$, $\sigma_\mathrm{lj} = 3.5$ Å, respectively. The fundamental MD mass unit m_0 corresponds to the mass of an ion ($\sim 10^{-26}$ kg) and all of the ions and monomers are given a mass $m = 1m_0$. τ is the fundamental MD unit of time derived from the length, mass and energy units as $\tau = \sigma_\mathrm{lj}\sqrt{m_0/\varepsilon}$. The system consists of a spherical colloid grafted with polyelectrolytes and salt ions as seen in Fig. 5.1. All particles in the simulation interact via the WCA potential, introduced in subsection 3.2.2. r_off in Eq. 3.18 is set to 0 except for the central particle where $r_\mathrm{off} = 3.0\sigma_\mathrm{lj}$ which sets the radius of the colloid to $R_\mathrm{col} = 3\sigma_\mathrm{lj}$.

The colloidal core is simulated with the raspberry model [111, 160, 205, 206]. It consists of a central particle and 113 neutral particles at a distance $R_\mathrm{col} = 3\sigma_\mathrm{lj}$ such that the whole object resembles a raspberry, as shown in the inset of Fig. 5.1. By using the raspberry model, as opposed to a single sphere with a large radius, we take into account the hydrodynamic interactions as explained in detail later in this section. The surface beads also serve as grafting points for the polymers. The colloidal core is rigid and uses the virtual sites algorithm in ESPResSo. The raspberry has a mass $m = 114m_0$ and a moment of inertia of $678m_0\sigma_\mathrm{lj}^2$ corresponding to a hollow sphere. Making the colloidal core rigid allows for larger time steps compared to previous studies using the non-virtual raspberry model [111, 160, 205]. This is due to the absence of the fast vibrations of the internal bonds within the raspberry. The electric charge of the colloid Q_col is put on the raspberry's central particle in the case of charged colloids.

M polyelectrolytes of degree of polymerization N are grafted to the colloid's surface beads in such a way that they are almost uniformly distributed on the surface with a minimum distance of $1.5\sigma_\mathrm{lj}$ between the chains. In our simulations, we use $N = 20$ and $M = 20$. The connectivity of the monomers both to each other and to the surface is maintained through Finitely Extensible Non-linear elastic (FENE) bonds (see Eq. 3.19). In these simulations $k = 30\varepsilon/\sigma_\mathrm{lj}^2$ and $R_0 = 1.5\sigma_\mathrm{lj}$ between monomers and $k = 30\varepsilon/\sigma_\mathrm{lj}^2$ and $R_0 = 2.0\sigma_\mathrm{lj}$ for the grafting of the chains to the surface beads of the colloid. The SAW model introduced in subsection 3.6.2 is used for the chains. Since only fully-repulsive potentials are used, the solvent behaves rather as an athermal solvent where the excluded volume of the monomers is temperature-independent.

A fraction λ of the monomers are given a charge +1 e. The total charge on the polymers is λNM. Note that the monomers are chosen at random from the entire group of MN monomers meaning that not all chains have the same number of charges. In order to have a fair comparison between different parameters, we used the same configuration (i.e. the same grafting points and charged monomers) for all systems with the same λ. For systems with different polyelectrolyte charge densities, the configuration with the closest smaller λ is used as the initial configuration and then the appropriate number of charges are added to the chains. For example, when we already have a system with $\lambda = 0.4$ and want to simulate a system with $\lambda = 0.5$, we start with the polymer and charge configuration of the former system and charge up neutral monomers until we have reached the desired charge density of $\lambda = 0.5$.

The salt ions are modeled explicitly as LJ spheres and $N_\mathrm{i} = c_\mathrm{s} V \mathrm{N_A}$ ions with charge $\pm 1\ e$ are added to simulate a system with molar concentration c_s of monovalent salt. $V = L^3$ is the volume of the simulation box. Electrostatic interactions are calculated via the P3M algorithm [76, 77] (refer to subsection 3.4.1 for an introduction) with an absolute accuracy of $10^{-2}\varepsilon/\sigma_\mathrm{lj}$ in the forces and $\lambda_\mathrm{B} = 2\sigma_\mathrm{lj} = 7$ Å, which is the value for the Bjerrum length in water at room temperature. An electric field of strength $E = 0.1\varepsilon/(e\sigma_\mathrm{lj})$ is applied in the x-direction as a constant force $q_i E$ on all particles where q_i is the charge of the ith particle. The time step is $\Delta t = 0.01\tau$.

The D3Q19 lattice-Boltzmann (LB) method [58, 207], explained in subsection 3.3.1, is used as implemented in ESPResSo [208] with an LB-lattice constant $a = 1\sigma_\mathrm{lj}$ and time step $\tau_\mathrm{LB} = 0.01\tau$. The LB fluid has a density $\rho = 0.85 m_0/\sigma_\mathrm{lj}^3$ and kinematic viscosity $\nu = 3\sigma_\mathrm{lj}^2/\tau$, yielding a dynamic viscosity of $\eta = 2.55 m_0/(\sigma_\mathrm{lj}\tau)$ [209–211]. All particles are dissipatively coupled to this background lattice-fluid by a bare coupling constant $\Gamma_0 = 20\sigma_\mathrm{lj} m_0/\tau$ using the scheme proposed by Ahlrichs and Dünweg [58]. As explained in subsection 3.3.1, this yields an effective mobility μ_eff of the beads (see Eq. 3.33):

$$\mu_\mathrm{eff} = \frac{1}{\Gamma} = \frac{1}{6\pi\eta R_\mathrm{H0}} = \frac{1}{\Gamma_0} + \frac{1}{g\eta a}, \tag{5.1}$$

where $g = 25$ is an empirical constant, Γ is the hydrodynamic friction coefficient, and R_H0 is the effective hydrodynamic radius. In our simulations $\mu_\mathrm{eff} \simeq 0.065\tau/m_0$ and $R_\mathrm{H0} \simeq 0.32\sigma_\mathrm{lj}$. This results in an effective hydrodynamic core radius slightly larger than the one given, $R_\mathrm{col}^\mathrm{H} = (3 + 0.32)\sigma_\mathrm{lj}$. An LB thermostat with temperature $k_\mathrm{B}T = \varepsilon$ keeps the temperature constant at room temperature.

Each system is simulated for 3×10^7 MD steps and found to be equilibrated after 5×10^6 steps, as the speed of the center of the mass of the colloid is constant. This speed is the drift speed of the colloid, which is in turn used to calculate its electrophoretic mobility. Here, the reduced mobility $\mu_\mathrm{red} = 3\mu\eta e/(2\varepsilon_\mathrm{rs}\varepsilon_0 k_\mathrm{B}T)$ is reported.

The simulation results are compared to the numerical solutions of the modified electrokinetic equations, introduced in subsection 3.5.3, obtained via the program provided by Reghan Hill. It solves the set of modified electrokinetic equations using a theory developed by Hill *et al.* [7, 125] (see subsection 3.5.5) based on the standard electrokinetic model discussed in subsection 3.5.2. The program requires several system parameters to calculate the mobility. One of the main inputs is the monomer density distribution, for which the solver allows the user to select from a number of functions. Here, an exponential function is chosen which fits the simulation monomer densities best:

$$\rho_\mathrm{mono}(r) = N_\mathrm{s} \exp[(r - R_\mathrm{col})/\delta], \tag{5.2}$$

N_s is the monomer density at the surface, r is the characteristic distance from the center of the colloid, R_col is the colloidal core's radius, and δ is the characteristic distance over which the density decays. The position of the shear plane is set to be the sum of the radius of the colloid and one ion diameter yielding $R_\mathrm{col} = 14$ Å. The radius of the spherical resistance centers, i.e. the monomers, is chosen to be the effective Stoke's radius of an ion $a_\mathrm{s} = a_\mathrm{eff} =$

$1/(6\pi\eta\mu_{\text{eff}}) = 1.12$ Å, where μ_{eff} is the effective ion mobility calculated by Eq. 5.1. The value of μ_{eff} is 2.535×10^{-7} m^2/(V.s). Since the monomer density fits are only approximations, the total number of the monomers N_{mono} in the numerical calculations, which is computed by integrating the fit function Eq. 5.2, is different from its value in the simulations. Thus, the charge fraction on the polymers λ used in the calculations is chosen such that $\lambda N_{\text{mono}} + Q_{\text{col}} = Q_{\text{net}}$, where Q_{net} is the net charge of the whole complex.

Taking advantage of the spherical symmetry, Gauss' law is used to calculate the gradient of the potential at the core's surface (scaled with $\kappa k_{\text{B}}T/e$) from its surface charge density (scaled with $\kappa\varepsilon k_{\text{B}}T/e$) as $\partial\psi^0/\partial r|_{r=\kappa R_{\text{col}}} = -\sigma_{\text{s}}$. The program also takes in the scaled electric field strength $E' = eE/\kappa k_{\text{B}}T$ which, setting $E = 0.1k_{\text{B}}T/(e\sigma_{\text{lj}})$ to be equal to that in the simulations, gives $E' = 0.1/\kappa\sigma_{\text{lj}}$. The limiting ionic conductivity used to calculate the drag coefficient of the ions is determined from the effective mobility to be $\Lambda = eN_{\text{A}}\mu_{\text{eff}} \simeq 0.024$ m^{2}A/(Vmol^{-1}). The radial extent of the calculations is set to be $R_{\text{min}} = 5\lambda_{\text{D}}$ or $R_{\text{max}} = L/2 - R_{\text{col}}$ depending on which is larger.

5.2 A Toy Model for the Electrokinetics of Polymer-Grafted surfaces

Before discussing the results, it is helpful to get a qualitative realization of the solution to the modified electrokinetic equations, introduced in subsection 3.5.3, and the effect of the grafted polymers on the EOF. A toy model is developed here for this purpose in which an approach similar to the Green's function method is used to solve Eq. 3.83 by placing a single test point charge $q(x)$ at different distances x from a surface. The charge distribution is given by a delta-like function centered at position $x = m$:

$$q(x) = \frac{1}{\sigma\sqrt{2\pi}} \exp\left(-\frac{(x-m)^2}{2\sigma^2}\right), \tag{5.3}$$

where σ is the standard deviation chosen to be $\sigma = 0.05$ in order to strongly localize the distribution around position $x = m$, see Fig. 5.2.

In order to simplify the problem and gain some basic understanding of the underlying physics, the Darcy-Brinkman equation is considered as one-dimensional (1D) and solved in the Cartesian coordinates. This is only strictly valid for the EOF above a flat polymer-grafted surface or in the limit of thin Debye layer, *however* the qualitative behavior is the same as for e.g. a spherical soft colloid. When an electric field is applied parallel to the surface, it exerts a force on the test charge which in turn causes a fluid flow in that direction. The electrostatic body force, the last term on the left-hand side of Eq. 3.83, is $E_x q(x)$. The pressure gradient is considered to be zero and, as a further simplification, the polymer layer is modeled by a step-like function as plotted in Fig. 5.3. In this picture, the monomer density is constant within the layer and drops abruptly to zero outside. The following expression can then be used to calculate the permeability of the polymer layer:

$$\frac{1}{l^2(x)} = \frac{1}{2l_0^2}\left(1 - \tanh\left(\frac{x-H}{\epsilon_{\text{d}}}\right)\right), \tag{5.4}$$

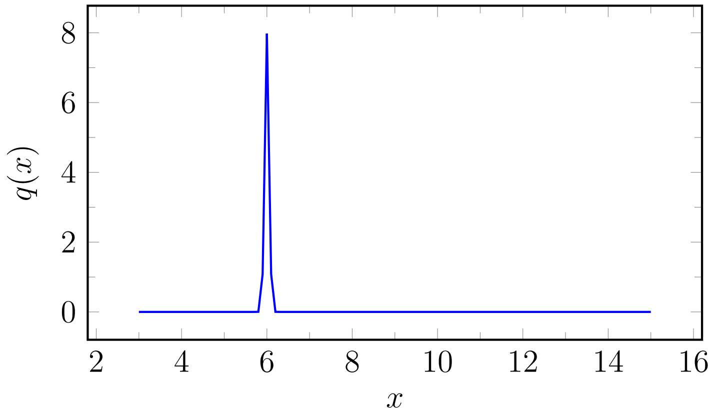

Figure 5.2: The charge distribution function $q(x)$ (see Eq. 5.3) with $\sigma = 0.05$ and $m = 6$, used to solve Eq. 3.83 in 1D. This represents an approximation of the delta peak that corresponds to a single point charge located at point $x = 6$.

where l_0 is the Brinkman length at the surface, and H and ϵ_d are the height and the characteristic decay length of the polymer layer, respectively. The smaller the decay length, the more homogeneous the polymer distribution is. In this case study $\epsilon_\mathrm{d} = 0.1$, $H = 5$, and $l_0 = \sqrt{R^2/M}$ to imitate the parameters used in the simulations of the spherical soft colloid presented here. $M/(R^2)$ is the grafting density with $R = 3$ being the radius and $M = 20$ the number of grafted chains. The origin of the coordinate system is fixed on the surface and, therefore, the particle velocity $\vec{V} = \vec{0}$. The velocity of the fluid in the bulk in the co-moving frame of reference represents the negative of the substrate's velocity in the lab frame. In Fig. 5.4 the fluid flow is shown for different positions of the test point charge. Unlike the plug flow typical for the EOF at bare surfaces, the results show a strong dependence of the flow far from the surface on the position of the charge. When the charge is positioned within the polymer layer, i.e. $m < H$, the fluid velocity increases from zero at the surface to a maximum value at the position of the charge. It then decreases exponentially due to the drag

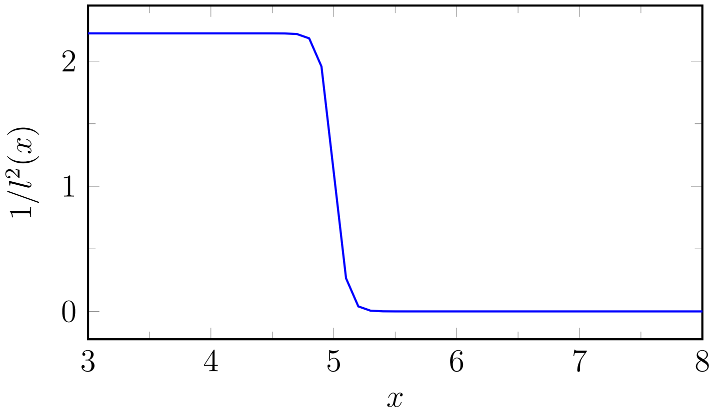

Figure 5.3: The monomer distribution function $1/l^2(x)$ (see Eq. 5.4) used to solve Eq. 3.83 in 1D with $l_0 = \sqrt{R^2/M} \simeq 0.67$, $H = 5$, and $\epsilon_\mathrm{d} = 0.1$.

force exerted on it by the polymers and reaches a constant value, the electro-osmotic speed, outside the layer. On the other hand, when $m > H$, the velocity increases from zero at the surface up to the position of the charge and then remains constant. The fluid speed depends on the position of the charge; it increases with m both inside as well as outside the brush. This shows that the screening effect decreases further away from the surface. The position of the test charge in this simplified toy model can be interpreted as the thickness of the Debye layer which, as will become clear below, has important and interesting consequences on the electrophoretic mobility of the soft particle.

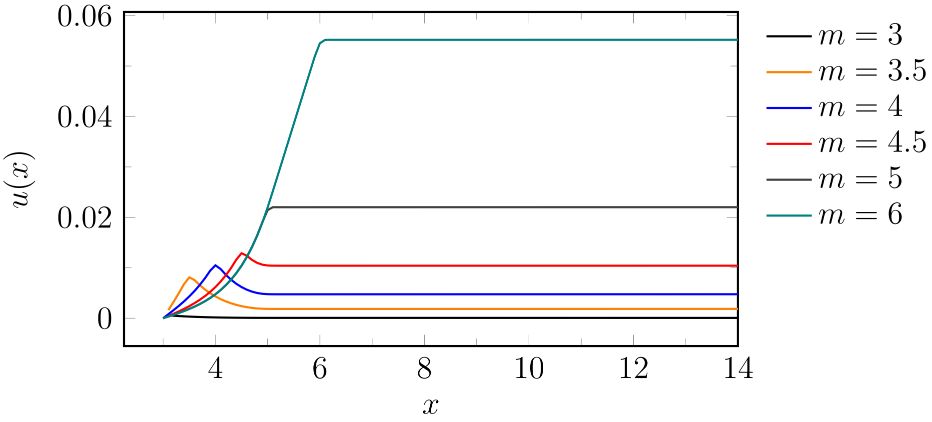

Figure 5.4: Fluid flows u as a function of the distance to the center of the colloid x obtained from solving Eq. 3.83 in 1D with a single point charge placed at different positions $x = m$. The equation is solved in the stationary state, i.e., $\partial\vec{u}/\partial t = 0$, with the origin of the coordinate system on the center of the colloid, i.e., $V = 0$. Other parameters are as in Figs. 5.3 and 5.2.

5.3 Characterization of the Polymer Layer

In this section, the typical structure of the polymers is examined as it plays an important role in the electrokinetic behavior of the soft colloid. In most cases studied here, the grafted polymers are charged and can therefore be polarized by the applied electric field. If this is the case, the induced dipole of the layer will interact with the applied field and thus affect the mobility of the particle. To verify that this does not occur for the parameters used in this work, we analysed the simulated density of the charged monomers on the left and the right side of the colloidal core. The applied electric field is from left to right. An example is shown in Fig. 5.5 where is seen that the distribution of the charged monomers is fairly symmetric and no significant polarization occurs. The same is also shown for all monomers (charged and uncharged) in Fig. 5.6.

In the thin Debye layer limit, the scaling behavior of the effective electrophoretic mobility of a composite is different in the mushroom or brush regime [120] as discussed in subsection 3.5.4. In the mushroom regime the polymers are grafted far from each other and maintain their equilibrium form, while in the brush regime the grafting density is high and the chains stretch out due to steric interactions. The brush regime is characterized by strong screening of the

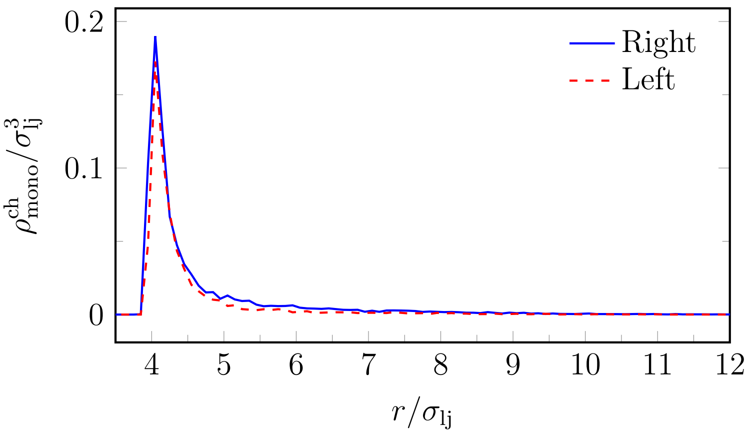

Figure 5.5: Radial density distribution of the charged monomers $\rho^{\mathrm{ch}}_{\mathrm{mono}}(r)$ on the right (solid line) and the left (dashed line) halves of the polyelectrolyte-grafted colloid with $Q_{\mathrm{col}} = -90$ e and $\lambda = 0.1$ ($Q_{\mathrm{net}} = -50$ e) at $c_{\mathrm{s}} = 0.001$ M of monovalent salt. The applied electric field is from left to right.

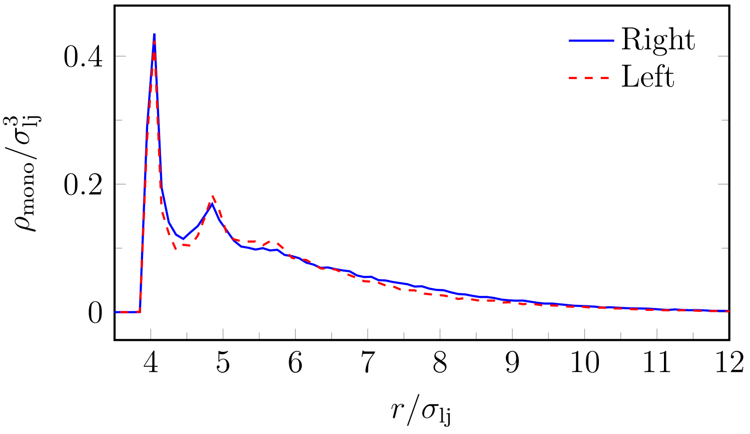

Figure 5.6: Radial density distribution of monomers $\rho_{\mathrm{mono}}(r)$ on the right (solid line) and the left (dashed line) halves of the polyelectrolyte-grafted colloid with $Q_{\mathrm{col}} = -90$ e and $\lambda = 0.1$ ($Q_{\mathrm{net}} = -50$ e) at $c_{\mathrm{s}} = 0.001$ M of monovalent salt. The applied electric field is from left to right.

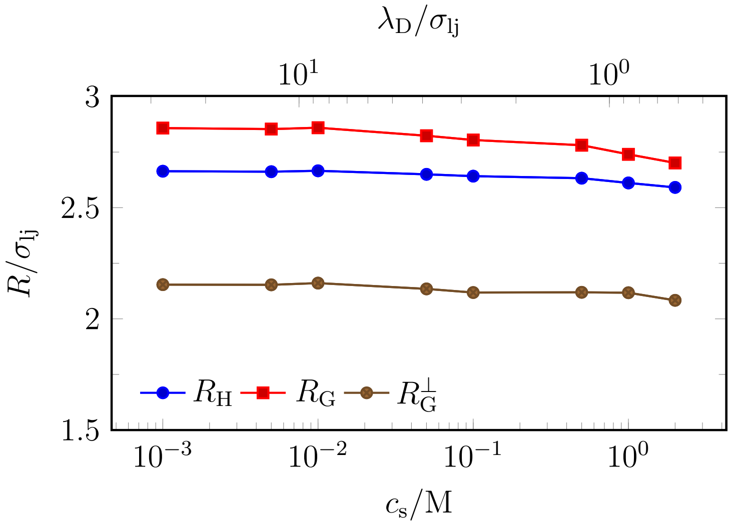

Figure 5.7: Hydrodynamic radius R_H, radius of gyration R_G, and its component perpendicular to the surface of the colloid $R_G^\perp$ of the grafted polyelectrolytes as a function of salt concentration c_s and the Debye length λ_D for a soft colloid with $Q_{col} = 0$ e and $\lambda = 0.1$. The dimensionless 'effective' surface coverage $\gamma^* = \gamma\pi(2R_H)^2$ is used to determine the regime in which the grafted polymers are [6]. Here, $\gamma^* > 15 \gg 1$ over the whole range of salt concentration and thus the system is always in the brush regime.

EOF produced by the underlying surface, resulting in a mobility similar in value to the mobility of the coating polyelectrolytes [7, 120, 190, 212]. This screening effect is significantly weaker in the mushroom regime and the mobility is dominated by the bare surface.

The hydrodynamic radius, Eq. 3.96, is used as a measure of the size of the polymer chains and shown over a range of salt concentrations in Fig. 5.7 for a composite object with $Q_{col} = 0$ e and $\lambda = 0.1$. Also the ensemble average of the radius of gyration R_G of the polymers (see Eq. 3.94), and its perpendicular component $R_G^\perp$, which can be used to estimate the height of the polymer layer, in Fig. 5.7. All three quantities are roughly constant over the whole range of salt concentrations. As the concentration increases, the electrostatic repulsion between the charged monomers is increasingly screened, which results in a slightly smaller size of the polyelectrolytes.

To determine whether the system is in the mushroom or the brush regime, the dimensionless quantity $\gamma^* = \gamma\pi(2R_H)^2$ is used as a measure of the coverage of the surface by the polyelectrolytes (an appropriate measure based on [6]). γ is the grafting density, i.e. here $\gamma = M/(4\pi R_{col}^2)$. For $\gamma^* \ll 1$ the system is in the mushroom regime and for $\gamma^* \gg 1$ it is in the brush regime. Here, the effective surface coverage is $\gamma^* > 15 \gg 1$ putting our system firmly in the brush regime over the whole range of salt concentrations. This implies a strong screening of the EOF produced by the underlying colloid at high salt concentrations [120].

5.4 Results and Discussion

In this section, the results for the electrophoresis of a polyelectrolyte-grafted spherical colloid are presented. The effect of different parameters, such as the salt concentration and charges, is discussed.

5.4.1 Effect of Salt Concentration on the Mobility of a Net-Neutral Soft Colloid

We start by studying the influence of monovalent salt concentration on the mobility of a soft colloid with a negatively charged core and positively charged polyelectrolyte brush. This is shown in Fig. 5.8 for the case of $Q_{\mathrm{col}} = -40$ e and $\lambda = 0.1$ (resulting in $Q_{\mathrm{net}} = 0$ e), together with three simulation snapshots for $c_{\mathrm{s}} = \{0.001, 0.1, 1.0\}$ M.

In the Hückel limit of no salt, one could think of the polyelectrolytes and the colloid as a solid sphere with the shear plane roughly at the edge of the polymer layer. The total charge is then zero and the object does not move under an applied electric field. This is borne out by the low salt mobility values in Fig. 5.8. This can also be seen by examining the net charge of the fluid, ρ_{ch}. It is minimal even close to the colloid as seen in Fig. 5.9 (b) for the lowest salt concentration $c_{\mathrm{s}} = 0.001$ M. This is because the Debye length $\lambda_{\mathrm{D}} \approx 27\sigma_{\mathrm{lj}}$ is much larger than the height of the polymer brush $H \sim 2R_{\mathrm{G}}^{\perp} \approx 4\sigma_{\mathrm{lj}}$. The counterions are mostly outside the coating and thus the charges on the polymers neutralize the core. Since they are grafted to the colloid, they are unable to move relative to it and thus produce no EOF, resulting in only a negligible velocity of the complex. This can also be seen in the numerically calculated tangential velocity as a function of the radial distance from the center of the colloid perpendicular to the applied electric field in Fig. 5.9 (c).

The approximative analytical expression derived by Ohshima [44] for a soft colloid, also show that at low salt concentrations it behaves like a bare particle in the Hückel limit. The mobility is proportional to the net charge as $\mu = Q_{\mathrm{net}}/D_{\mathrm{H}}$, where D_{H} is the hydrodynamic drag coefficient of the soft colloid and depends on the height and the softness of the polymer layer through rigorous equations. Here, $Q_{\mathrm{net}} = 0$ e and the formula results in $\mu = 0$.

Naively, one might expect the mobility to be zero for all salt concentrations since the object as a whole is charge neutral. However, as discussed in subsection 3.5.3, the polymers exert a viscous drag on the fluid locally and thus partially screen its flow. When the core's counterions are predominantly within the polymer layer, i.e. when $\lambda_{\mathrm{D}} \leq H$, the polymers screen their EOF. In contrast, the EOF generated by the polyelectrolytes' counterions, which are further from the surface and thus subject to less screening, dominates and the electrophoretic mobility of the soft colloid becomes non-zero. This is what happens when more salt is added, the Debye length decreases and more and more counterions of the colloid penetrate the brush (as can be seen in the snapshots in Fig. 5.8). At $c_{\mathrm{s}} = 0.1$ M the Debye length is $\lambda_{\mathrm{D}} \approx 3\sigma_{\mathrm{lj}}$ and we see in Fig. 5.9 (b) that there is now a significant accumulation of counterions within a few ion diameter of the colloidal core. It is evident from the initial increase and the following exponential decrease of the tangential velocity as a function of the radial distance from the center of the colloid perpendicular to the applied electric field in Fig. 5.9 (c) that the EOF generated by these ions is mostly screened. On the other hand, a larger part of the EOF generated by the polyelectrolytes' counterions reaches the bulk, resulting in a positive mobility of the neutral soft colloid. At yet higher salt concentrations there are even more counterions around the colloidal core as shown in Fig. 5.9 (b). There is thus even more screening of the EOF generated by the underlying colloid's counterions. This is why we see the highest mobilities at the highest salt concentrations, in contrast to bare colloids where the electrophoretic mobility generally decreases with increasing salt concentration [3, 4].

A secondary cause for the increase of the mobility with salt concentration is the effect of salt on the height of the polymer layer, as can be seen in Fig. 5.9 (a). Since the colloid and the polyelectrolytes are oppositely charged, they attract each other reducing the layer thickness. With increasing salt concentration the electrostatic attraction is progressively screened and the polyelectrolytes stretch farther into the fluid, increasing the thickness of the layer. This in turn increases the screening of the colloid's EOF and thereby, the net mobility of the composite.

Ohshima also derived an approximative equation for the mobility of a soft colloid with small surface and brush charge densities in the $\kappa H \gtrsim 1$ regime

$$\mu = \frac{z_\mathrm{p} e \lambda}{6\pi a_\mathrm{s} \eta}\left[1 + \left(\frac{\lambda_\mathrm{p}}{\kappa}\right)^2 \frac{1 + \lambda_\mathrm{p}/(2\kappa)}{1 + \lambda_\mathrm{p}/\kappa}\right] + \frac{\sigma_\mathrm{s}}{\eta\kappa}\left[\frac{e^{-\kappa H}/\kappa}{1/\lambda_\mathrm{p} + 1/\kappa} + \frac{2}{\lambda_\mathrm{p}} \frac{e^{-\lambda_\mathrm{p} H}/\lambda_\mathrm{p} - e^{-\kappa H}/\kappa}{(1/\lambda_\mathrm{p})^2 - (1/\kappa)^2}\right]. \quad (5.5)$$

Here, z_p is the valency of the charged monomers, σ_s is the surface charge density of the substrate, and $\lambda_\mathrm{p} = (6\pi a_\mathrm{s} n_\mathrm{p})^{1/2}$, with n_p being the uniform monomer volume density. $1/\lambda_\mathrm{p}$ is the electrophoretic softness of the brush. Note that in the limit of $\kappa \to \infty$, Eq. 5.5 reduces to $\mu = ze\lambda/(6\pi a_\mathrm{s}\eta)$ which depends only on the charge density of the brush. Taking $H = 2R_\mathrm{G}^{\perp}$ and $n_\mathrm{p} \simeq NM/V_\mathrm{p}$, with V_p being the volume of the polymer layer, the result of Eq. 5.5 is shown in Fig. 5.8. Due to the exponential dependence of this expression to κ, it diverges rapidly with decreasing salt, where the large κ assumption becomes less and less valid.

The numerical results, depicted in Fig. 5.8 by the solid lines, agree well with the simulation results. The differences are mostly due to the small discrepancies of the fits to the simulations monomer density profiles shown in Fig. 5.9 (a). The fits underestimate the monomer density near the surface where the simulations show a peak, then overestimate it slightly farther from the surface, followed by a slight underestimation far from the surface. Underestimation of the monomers' density decreases the total mobility by decreasing the viscous drag force exerted by the monomers and thus increasing the portion of the core's EOF reaching the bulk. Similarly, overestimation of the monomer density tends to increase the total mobility. Likewise, the ion density near the colloid's surface in Fig. 5.9 (b) is slightly higher in the case of the numerical calculations due to the absence of steric interactions in the mean-field approach. The discrepancies with the simulation values are, however, small and therefore have only a minimal influence on the calculated mobilities.

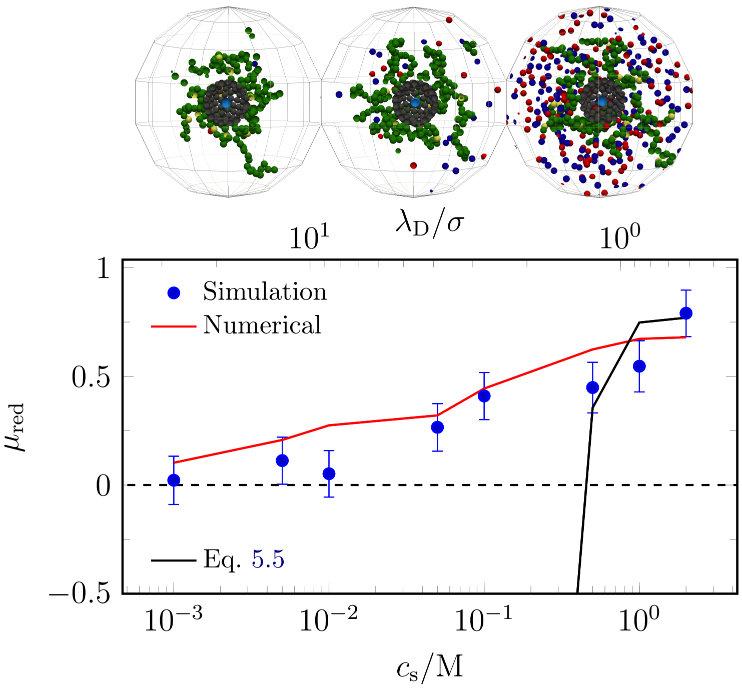

Figure 5.8: The reduced mobility μ_{red} of a neutral soft colloid as a function of monovalent salt concentration c_s and the corresponding Debye length λ_D. MD simulations (blue circles) are compared to the numerical results produced using the program provided by Hill [7] (red line), and Eq. 5.5 (black line). At the top three simulation snapshots are shown for $c_s = \{0.001, 0.1, 1.0\}$ M, respectively from left to right. The snapshots show only a radius of 14σ from the center of the colloid and are cut in half, the color coding is the same as in Fig. 5.1. The applied electric field is from left to right in these pictures.

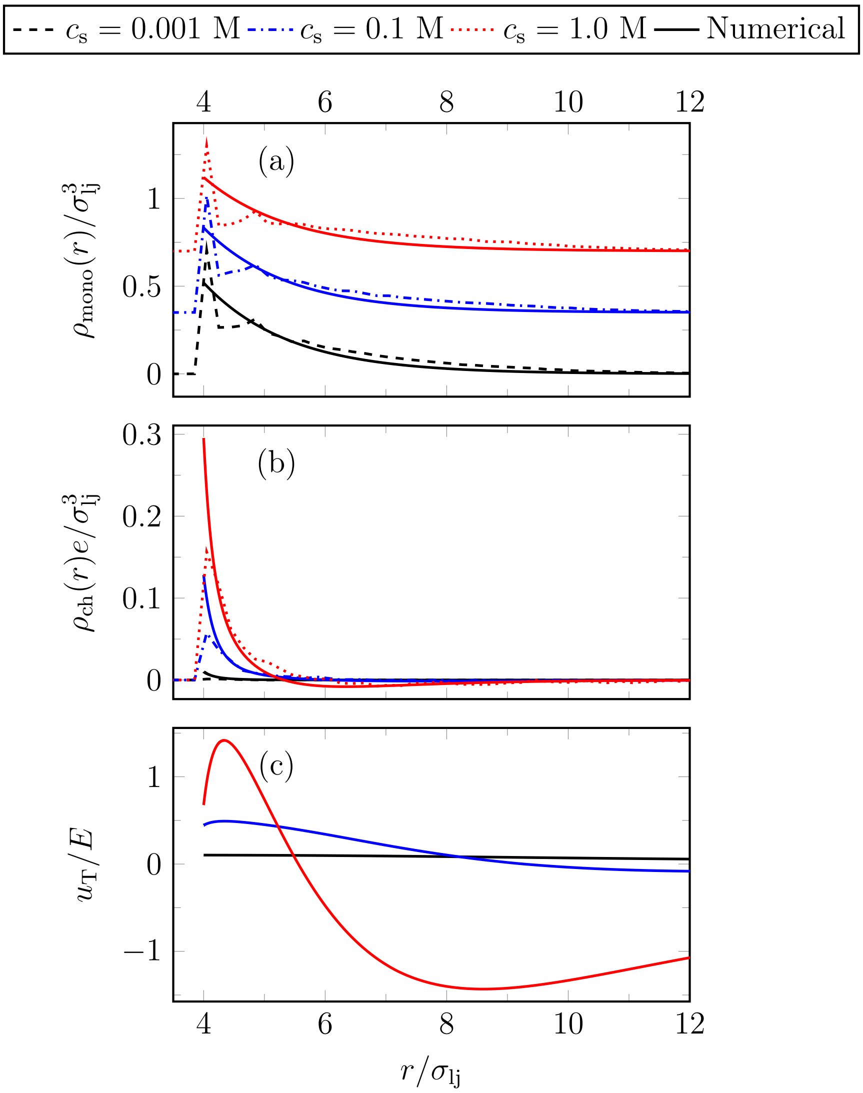

Figure 5.9: (a) Radial density profiles for $c_s = 0.001$ M (dashed black lines), $c_s = 0.1$ M (dash-dotted blue lines) and $c_s = 1$ M (dotted red lines) of the monomers $\rho_{\text{mono}}(r)$ and (b) fluid charge excluding the fixed charges $\rho_{\text{ch}}(r)$ for a neutral composite with $Q_{\text{col}} = -40$ e and $\lambda = 0.1$. The monomer density profiles are shifted vertically by factors of 0.35 for the sake of visibility. The solid lines represent the numerical results. (c) The numerically obtained rescaled tangential fluid flow field as a function of the radial distance from the center of the colloid perpendicular to the applied electric field $u_T(r)/E$. The reference frame is fixed on the center of the colloid, i.e., the rescaled velocity values at the surface of the colloid correspond to the reduced electrophoretic mobilities and they converge to zero far from the surface.

5.4.2 Effect of Charge on the Mobility of a Net-Neutral Soft Colloid

In Subsection 5.4.1, it was shown that the screening of the core's EOF by the grafted polyelectrolytes causes a net-neutral soft colloid to have a positive mobility at moderate to high salt concentrations. In this subsection, the effect of charge on the electrophoretic mobility of net-neutral soft colloids is investigated at fixed salt concentration $c_\mathrm{s} = 0.5$ M ($\lambda_\mathrm{D} = 1.2\sigma_\mathrm{lj}$). Specifically, the charges on the colloidal core and the grafted polyelectrolytes are varied such that the object as a whole remains charge neutral ($Q_\mathrm{col} + \lambda MN = 0$).

The simulation results are plotted in Fig. 5.10. The system is in the polyelectrolyte-dominated regime ($\lambda_\mathrm{D} < H$ at $c_\mathrm{s} = 0.5$ M), i.e. the EOF generated by the core's counterions is screened by the brush and the EOF of the polyelectrolytes' counterions dominate. It is therefore not surprising that the mobilities are all positive. They increase with increasing charge up to $Q_\mathrm{col} = -160$ e ($\lambda = 0.4$) and then decrease slightly, converging to a similar value as in the case of $Q_\mathrm{col} = -40$ e ($\lambda = 0.1$). The reason can be gleaned from the three simulation snapshots shown at the top of Fig. 5.10 for $Q_\mathrm{col} = \{-40, -160, -400\}$ e. The initial increase in the mobility is due to the increasing charge fraction on the monomers.

On increasing the charges further, the electrostatic attraction between the polyelectrolytes and the core increases and a second peak appears in the monomer density profile, as the brush becomes more compact (Fig. 5.11 (a)). As a result of the compression of the brush, the contribution of the competing EOF generated by the core's counterions increases and thus the total mobility decreases. The simulation snapshot for $Q_\mathrm{col} = -400$ e ($\lambda = 1.0$) in Fig. 5.10 shows that in this case all the chains are collapsed and there are virtually no counterions within the monomers (see also Fig. 5.11 (b)). It is only the tails of the chains which are not completely collapsed that drive the whole composite in the positive direction.

The initial linear increase of the mobility with respect to the charge in Fig. 5.10 is in line with the theoretical expression of Ohshima [43], which predicts the mobility to scale linearly with λ:

$$\mu = z_\mathrm{p} e\lambda/(6\pi\eta a_\mathrm{s}), \ \ \kappa \to \infty. \tag{5.6}$$

The agreement between our simulations and Eq. 5.6, also depicted in Fig. 5.10, worsens with increasing charge and is only acceptable for the three lowest charges. This is to be expected since this expression is only strictly valid in the limit of infinite κ. For large but finite values of κ Eq. 5.5 simplifies to an approximative expression for the mobility of a brush of uniform density with an error of the order $\mathcal{O}(1/\kappa^2)$ [43]:

$$\mu = \frac{z_\mathrm{p} e\lambda}{6\pi\eta a_\mathrm{s}} + \frac{2\sigma_\mathrm{s}}{\eta\kappa} e^{-H\sqrt{6\pi a_\mathrm{s} n_\mathrm{p}}}, \tag{5.7}$$

The second term in this equation formulates the contribution from the substrate (assumed to be a flat surface here) to the EOF and the exponential decay due to the screening by the brush. The importance of the core therefore increases with increasing σ_s and decreasing H. Comparing our results with Eq. 5.7, we see, as shown in Fig. 5.10, that the second term makes the agreement better for the three lowest charges, but does not change the overall agreement. For the parameters used here, Eq. 5.7 behaves linearly and fails to capture the nonlinearity in the mobility. The reason is that this equation is simplified for small λ and σ_s. A secondary source of disagreement between Eq. 5.7 and our results is that in the theory all particles are

considered as point particles and the ions can penetrate the brush even at very high charges where all the chains are collapsed on the core. The high charge densities at which this occurs, however, are unlikely to occur in experiment and the formula does an excellent job of predicting the mobility at low to moderate charge densities.
Interestingly, Eq. 5.5, on the other hand agrees fairly good with our simulations. The discrepancy is significant only at $Q_{\mathrm{col}} = -400$ e, where the mean-field approach of the theory breaks. The systematic underestimation of the mobility is the result of the overestimation of the core's contribution, formulated in the second term of Eq. 5.5. As mentioned above, the lack of ionic size causes the core's counterions to penetrate the brush even at very large charges, and therefore produce a larger EOF. In fact, if not for the increase in λ and the decrease in H, the agreement would not have been so good.

The numerical calculations in Fig. 5.10 show large discrepancies in comparison to the simulation data. For the two lowest charges the numerical approach slightly overestimates the mobilities, while at higher charges the mobilities are strongly underestimated. The main reason for the discrepancies is the absence of ionic size in the mean-field theory used for the electrostatic interactions in the numerical approach. This manifests itself in the numerical fluid charge density profiles shown in Fig. 5.11 (b), where due to the absence of dispersive forces, there are no layering effects as observed for the simulation results. At very high charges, all the positive ions congregate on the core's surface. In the case of $Q_{\mathrm{col}} = -400$ e ($\lambda = 1.0$), the numerical fluid charge density is as high as $30\mathrm{e}/\sigma^3$ at the surface (only shown to $\rho = 3\mathrm{e}/\sigma^3$ here for the sake of visibility) and becomes significantly negative afterward. This is accompanied by the fact that the second peak in the simulated monomer density, which is underestimated by the fit at lower charges, becomes so large that it influences the fit. The result is that the overall monomer density is now overestimated by the fit, making the brush layer effectively thicker. As a consequence the mobility increases, resulting in an overestimation of the mobility with respect to the simulation result. It needs to be emphasized here that such large charges are unrealistic and that the continuum model provides good agreement for all experimentally realizable charge densities.

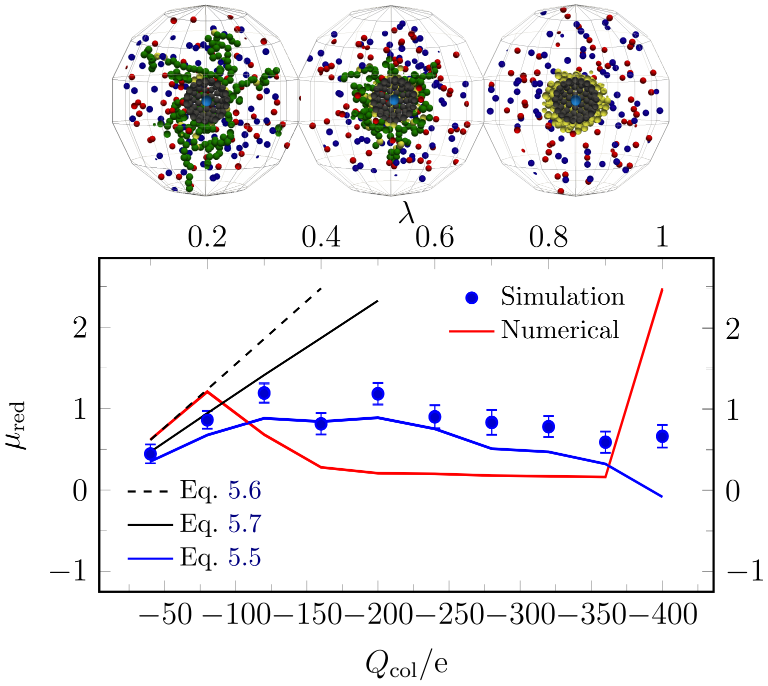

Figure 5.10: The reduced mobility $\mu_{\rm red}$ as a function of the colloid charge $Q_{\rm col}$ and the corresponding charge fraction on the polyelectrolytes λ for neutral soft colloids at fixed salt concentration $c_{\rm s} = 0.5$ M. The simulation results (blue circles) are compared with the numerical results (red solid line), Eq. 5.6 (black dashed line), Eq. 5.7 (solid black line), and Eq. 5.5 (blue solid line). At the top, three simulation snapshots are shown for $Q_{\rm col} = \{-40, -160, -400\}$ e, respectively from left to right. The snapshots show only a radius of 14σ from the center of the colloid and are cut in half, the color coding is the same as in Fig. 5.1. The applied electric field is from left to right in these pictures.

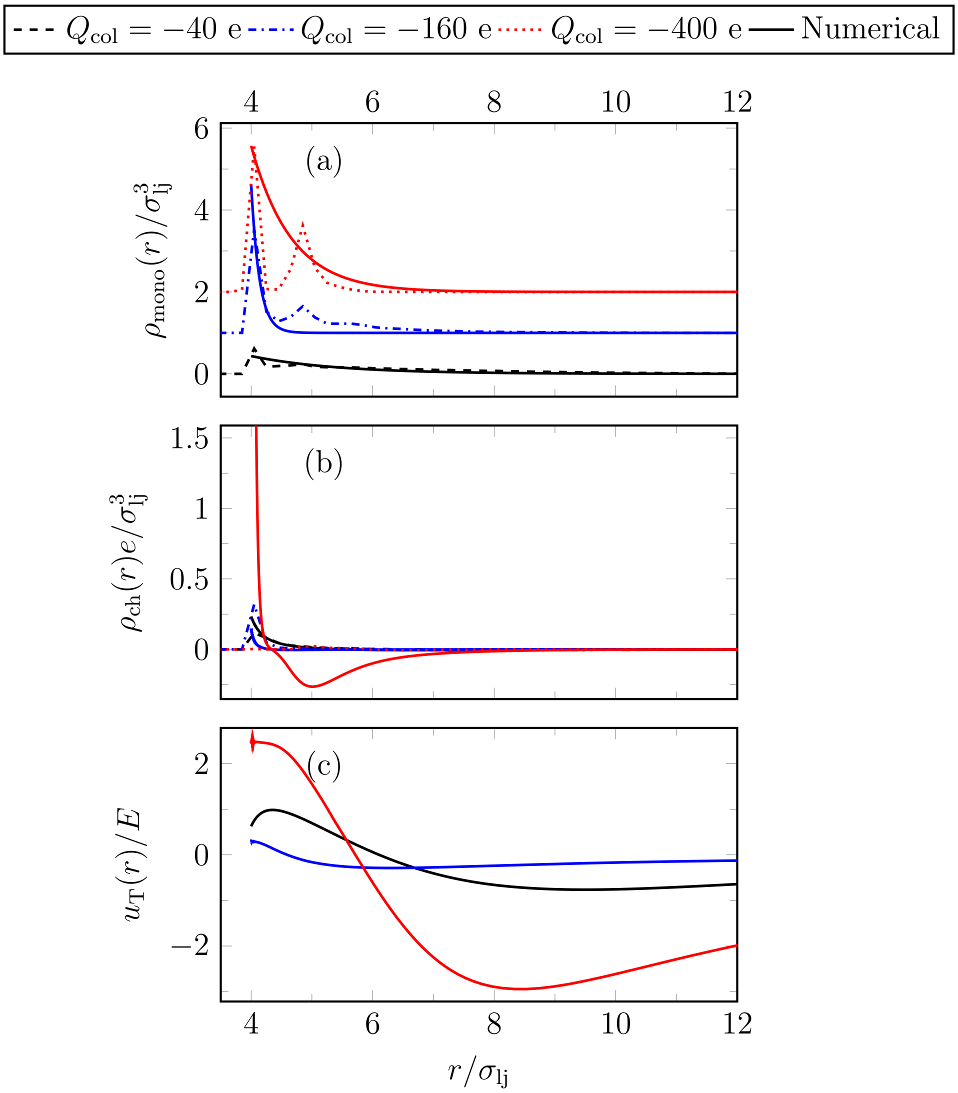

Figure 5.11: (a) Radial density profiles for $Q_{\text{col}} = -40$ e ($\lambda = 0.1$) (dashed black lines), $Q_{\text{col}} = -160$ e ($\lambda = 0.4$) (dash-dotted blue lines) and $Q_{\text{col}} = -400$ e ($\lambda = 1.0$) (dotted red lines) of the monomers $\rho_{\text{mono}}(r)$ and (b) fluid charge excluding the fixed charges $\rho_{\text{ch}}(r)$. The monomer density profiles are shifted vertically by factors of 1 for the sake of visibility. The solid lines represent the numerical results. (c) The numerically obtained rescaled tangential fluid flow field as a function of the radial distance from the center of the colloid perpendicular to the applied electric field $u_{\text{T}}(r)/E$. The reference frame is fixed on the center of the colloid, i.e., the rescaled velocity values at the surface of the colloid correspond to the reduced electrophoretic mobilities and they converge to zero far from the surface.

5.4.3 Comparison with Theoretical Predictions: Decomposition of a Net-Neutral Soft Colloid

In subsection 3.5.4, a scaling theory for the electrokinetics of soft surfaces in the thin Debye layer limit was discussed. Harden *et al.* [120], who developed this theory, decomposed the calculation of the electrokinetic response of a polyelectrolyte-grafted charged surface into two separate subproblems; *i*) a negatively charged surface and neutral grafted polymers, *ii*) a neutral surface grafted with positively charged polymers. The superposition of the two subcases is equivalent to the original system. Here, the validity of this prediction is tested by simulations of spherical soft colloids. Figure 5.12 shows the mobility of the two complementary soft colloids corresponding to the two cases mentioned above. The magnitude of both mobility curves decreases with increasing salt concentration, but have opposite signs. The absolute value of the mobility of the neutral colloid with positively charged polymers is greater than that of the negatively charged colloid with neutral polymers. This is because the EOF generated by the polyelectrolytes on a neutral colloid is less screened than the EOF generated by a charged colloid with a neutral coating. It is also notable that the mobility of the charged colloid approaches zero at hight salt concentrations whereas in the charged brush case it converges to a finite value which, as discussed in the next subsection, is related to the charge density of the grafted polyelectrolytes [7, 43, 120]. In Fig. 5.13, the result for the neutral soft colloid is compared to the superposition result. While the qualitative behavior is the same in both cases, the quantitative differences are significant even at higher salt concentrations, where the requirement of a thin Debye length should be fulfilled, and the theory predicts the two to have the same mobility. Only at $c_\mathrm{s} = 2.0$ M are the two results quantitatively similar. This is due to the fact that for the parameters used here the polyelectrolytes are deformed due to electrostatic attraction to the colloid as seen in Fig. 5.14. This source of deformation is neglected in the theory since the surface potential is considered to be low. The discrepancy decreases with increasing salt concentration as the electrostatic interactions are more strongly screened. This is why the two mobilities approach each other at higher salt concentrations, where the underlying assumption of screened electrostatic interactions is increasingly valid.

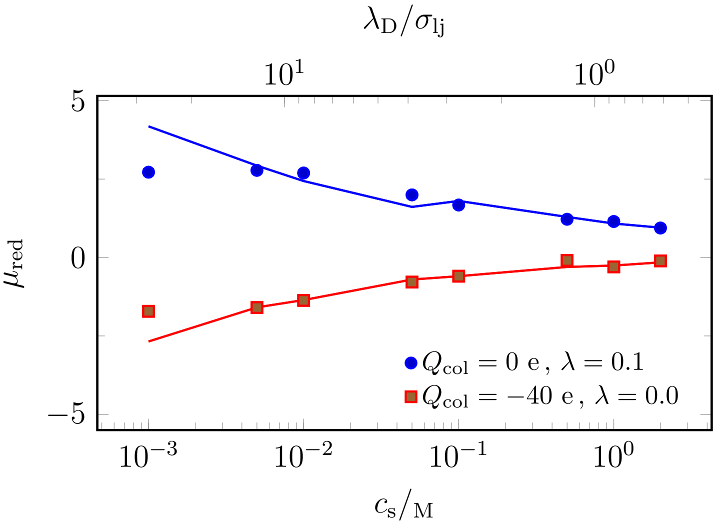

Figure 5.12: The reduced electrophoretic mobility μ_{red} as a function of salt concentration c_s and the corresponding Debye length λ_D for two different composites; one with neutral colloid and charged grafted polymers ($\lambda = 0.1$) shown via filled circles, and the other with charged colloid ($Q_{col} = -40$ e) and neutral grafted polymers depicted by the filled squares. The solid lines depict the numerical results obtained using the program provided by Hill *et al.* [7].

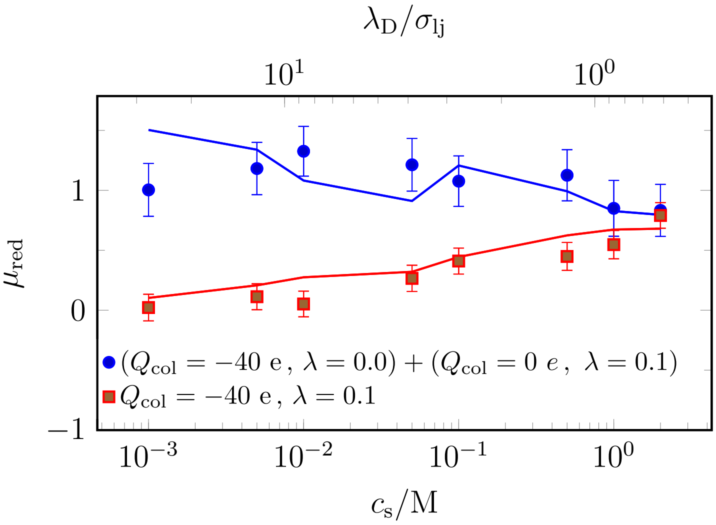

Figure 5.13: The reduced electrophoretic mobility μ_{red} as a function of salt concentration c_s and the corresponding Debye length λ_D for two cases; (i) neutral composite with $Q_{col} = -40$ e and $\lambda = 0.1$ (red squares), and (ii) the superposition of a composite with $Q_{col} = -40$ e and $\lambda = 0.0$, and another with $\lambda = 0.1$ and $Q_{col} = 0$ e (blue circles). The solid lines with the corresponding colors are the numerical results obtained via Hill's solver.

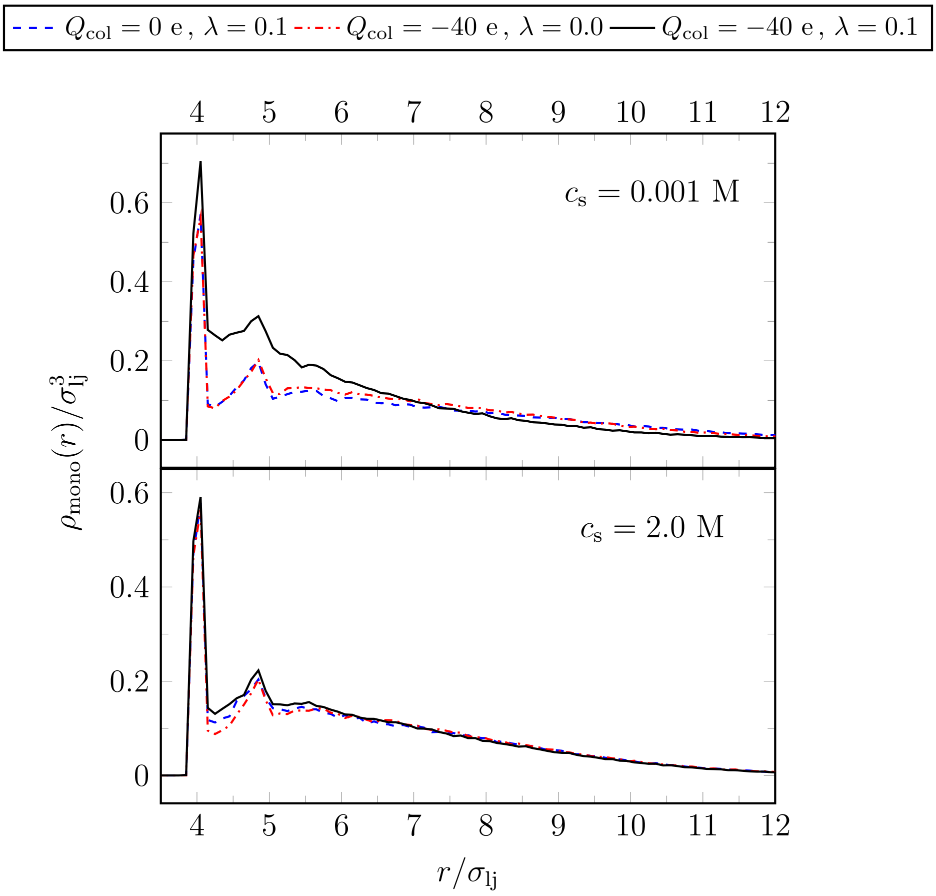

Figure 5.14: Monomer number density $\rho_{\mathrm{mono}}(r)$ as a function of the distance to the center of the colloid r at $c_{\mathrm{s}} = 10^{-3}$ M (top panel) and $c_{\mathrm{s}} = 2.0$ M (bottom panel) for three different cases; charged colloid ($Q_{\mathrm{col}} = -40$ e) grafted with neutral polymers (red dash-dotted line), neutral colloid with charged polymers ($\lambda = 0.1$) (blue dashed line), and charged colloid ($Q_{\mathrm{col}} = -40$ e) with charged polymers ($\lambda = 0.1$) (black solid line).

5.4.4 Comparison with Theoretical Predictions: Net-Neutral Soft Colloid vs. Single Free Polyelectrolyte

The mobility of a single polyelectrolyte and that of a colloid coated with a thick layer of polyelectrolytes with the same physical properties have been shown to be roughly equal at high salt concentrations through theoretical calculations [120], experiments [41], and simulations [42]. Here, we check the validity of this scaling behaviour by comparing the mobility of the neutral soft colloid to that of a single polyelectrolyte. Experimentalists have long known that the mobility of free polyelectrolytes first increases with increasing chain length up to $N \sim 20$ and then decreases slightly for longer chains, converging to its long-chain or “free-draining” limit [213, 214]. More recently, the same behavior has also been observed in computer simulations which explicitly account for hydrodynamic interactions [209, 215, 216]. Therefore, the length of the polyelectrolyte used here to determine the mobility is chosen to be $N = 50$. This result in the free-draining limit of the mobility for most of the salt concentration range, only at the lowest salt concentrations some small length dependencies might still be present.

The results in Fig. 5.15 verify that the mobility of the single polyelectrolyte chain in solution decreases with increasing salt concentration as expected for bare particles and in agreement with both experiment [213] and simulation [217]. This is in juxtaposition to the behavior of the soft colloid, which actually has an increasing mobility with increasing salt concentration. Since our system is in the brush regime as verified in Sec. 5.3, at high salt concentrations we expect the mobility of the composite to be roughly equal to the mobility of a single free polyelectrolyte having the same linear charge density based on the theory of Harden *et al.* [120].

The two mobilities in Fig. 5.15 approach each other at higher salt concentrations, but they are equal only at $c_\mathrm{s} = 2.0$ M. The reason is again the deformation of the polymer layer due to the strong electrostatic attraction to the oppositely charged colloid which decreases the height of the grafted layer. This conclusion is drawn since the mobility of the soft colloid with $Q_\mathrm{col} = 0$ e and $\lambda = 0.1$ also depicted in Fig. 5.15 does become equal to that of a single free polyelectrolyte for a larger range of salt concentration. The large discrepancy between the two mobilities at low salt concentration is because the underlying theory assumption $\lambda_\mathrm{D} < H$ is invalid in this regime.

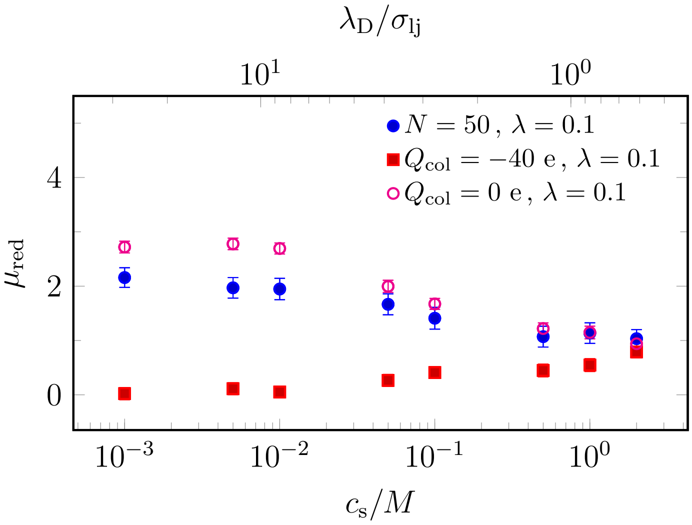

Figure 5.15: Reduced electrophoretic mobility μ_{red} as a function of salt concentration c_s and the corresponding Debye length λ_D for a single free polyelectrolyte with $N = 50$ and $\lambda = 0.1$ (blue filled circles) compared to the that of the neutral soft colloid with $Q_{col} = -40$ e and $\lambda = 0.1$ (red squares). Also shown is the result for the soft colloid with $Q_{col} = 0$ e and $\lambda = 0.1$ (magenta circles).

5.4.5 Effect of Salt Concentration on the Electrophoretic Mobility of a Net-Charged Soft Colloid

Thus far either neutral soft colloids, where the charge on the colloidal core is canceled by the charges on the grafted polyelectrolytes, or cases where only one of the two components is charged were considered. Here, a net negative soft colloid, with $Q_{col} = -90$e and $\lambda = 0.1$, is examined and the effect of monovalent salt concentration on its electrophoretic mobility is investigated.

At low salt concentrations, the Debye length is larger than the brush height and the counterions extend outside the brush where the EOF they generate is not damped, making the negatively charged composite move in the opposite direction of the applied electric field. This is confirmed by the negative low salt mobility of the net-negative soft colloid plotted in Fig. 5.16. In the salt-free Hückel limit, all the counterions “evaporate” from the particle’s surface to increase their entropy, and the mobility of a spherical particle is given by $\mu = Q_{net}/(6\pi\eta R_H)$. For the system under investigation here, $R_H \sim R_{col} + 2R_G^{\perp} \sim 7\sigma_{lj}$ should result in $\mu_{red} \sim -15$, which is much larger than the results at the lowest salt concentration $c_s = 0.001$ M. Also the approximation $\mu = Q_{net}/D_H$ derived by Ohshima [44] for the mobility of a soft colloid in the Hückel limit strongly overestimates our simulation results at low salt concentration. The reason is the high net charge of the composite and the finite size of the simulation box which prevent us from reaching the Hückel limit. As can be seen from Fig. 5.17 (b) and the left-most snapshot at the top of Fig. 5.16, there are still a significant number of counterions within the brush at $c_s = 0.001$ M, decreasing the mobility significantly compared to the Hückel limit [218].

At $c_s = 0.05$ M, $\lambda_D \sim 4\sigma_{lj}$ is the same as the height of the brush $H = 2R_G^{\perp} \sim 4\sigma_{lj}$. Increasing the salt concentration further decreases the Debye length and the counterions penetrate more and more into the brush as seen in Fig. 5.17 (b). These ions have their EOF screened and do not contribute to the total mobility of the soft colloid. The mobility undergoes a transition from a regime where the net charge dominates (low salt concentrations) to a regime where the brush charge dominates (high salt concentrations) and thus, reverses sign with respect to *monovalent* salt as observed in Fig. 5.16. The crossover occurs at about $c_{\mathrm{s}} = 0.1$ M corresponding to $\lambda_{\mathrm{D}} \sim 3\sigma_{\mathrm{lj}}$, which is slightly smaller than the height of the polymer layer. At the highest salt concentration, $c_{\mathrm{s}} = 2.0$ M, the mobility approaches the same value as in the case of the net-neutral soft colloid (see Fig. 5.8). This is a characteristic behaviour of soft surfaces that in the limit of thin Debye layers, the mobility is governed by the physical properties of grafted layer, independent of the charge of the underlying interface [7, 41, 42, 120, 212].

The type of the mobility reversal encountered here in *monovalent* salt has a very different nature from that in multivalent salt studied in chapter 4. It is purely the result of two competing EOFs and the interplay between the two relevant length scales, namely λ_{D} and H, and should not be mistaken for the well-known mobility reversal in the presence of multivalent salt at high ionic strengths. As discussed at length in the previous chapter, the mobility reversal of bare surfaces is a result of overcharging due to strong ion correlations or specific adsorption of the counterions to the surface [3, 4]. Recently, Marconi *et al.* have observed similar results for the electroosmotic flow in a polyelectrolyte-grafted capillary, using a numerical method to solve the modified electrokinetic equations based on implicit ion description and a lattice-Boltzmann method for the fluid [219]. They provide a phase diagram, showing the effect of the core's and the polyelectrolytes' charges on the sign of the electroosmotic flow at different salt concentrations.

The high-salt results are compared to Eq. 5.5, as shown in Fig. 5.16. The agreement quickly breaks down when the Debye layer increases as the equation is only valid in the high salt limit. It should also be noted, that Eq. 5.5 is for low surface charge density, which is not the case here.

The numerical results are also shown in Fig. 5.16 and their agreement with the simulations is quite good. The mobility reversal occurs at the same salt concentration as in simulations. The slight discrepancies are again due the fits to the monomers' density shown in Fig. 5.17 (a), which are used as an input to the numerical solver, and the slight overestimation of the fluid charge adjacent to the colloid as seen in Fig. 5.17 (b). This mobility reversal is also expected to occur for much larger, experimentally accessible, colloids. This is verified numerically as shown in Fig. 5.16 for $R_{\mathrm{col}} = 1\ \mu$m. To do so, the monomer density parameters are taken from the fit to the simulation data for $c_{\mathrm{s}} = 0.001$ M and the core's surface charge density as well as the net charge density are kept the same. This results in a higher charge fraction on the polyelectrolytes due to the constraint $Q_{\mathrm{net}} = Q_{\mathrm{col}} + \lambda M N$, which in turn leads to higher mobilities in the polyelectrolyte-dominated regime compared to the small colloid. In the net-charge-dominated regime, it is the larger size of the core that causes the mobility to have higher absolute values, as also observed in case of bare colloids [220]. The data show that the salt concentration at which the mobility reversal occurs remains the same since it is determined by the brush height. The fact that this phenomenon is experimentally achievable gives it the potentiality to have different applications in soft-colloid electrophoresis and microfluidics. It can be exploited to measure the salt concentration *locally* or extract information about the grafted layer.

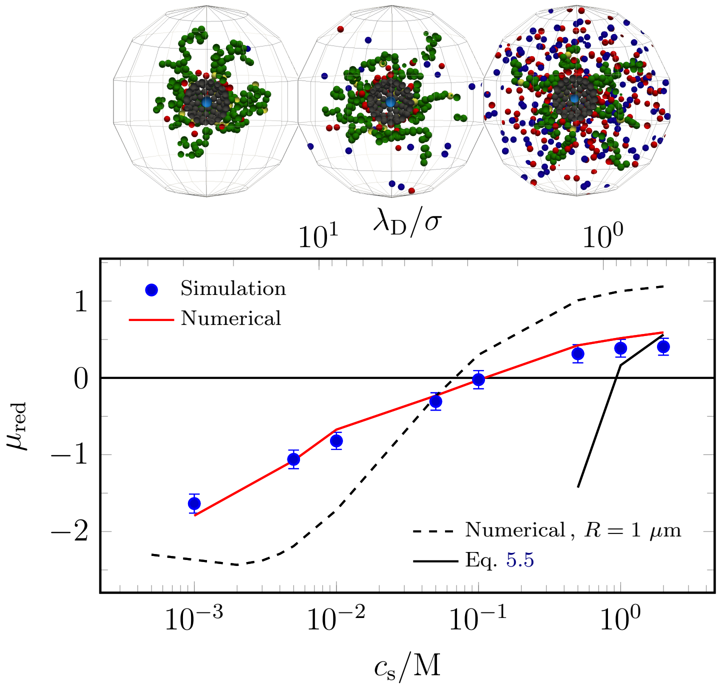

Figure 5.16: The reduced mobility μ_{red} of a colloid with $Q_{\text{col}} = -90$ e grafted with positively charged polymers with $\lambda = 0.1$ as a function of the monovalent salt concentration c_s and the corresponding Debye length λ_D. The net charge of the soft colloid is $Q_{\text{net}} = -50$ e. MD simulations (blue circles) are compared to the numerical results produced using the program provided by Hill [7] (red line) and Eq. 5.5 (black solid line). The dashed line indicates the numerical results for $R_{\text{col}} = 1\ \mu$m. At the top three simulation snapshots are shown for $c_s = 0.001$ M, $c_s = 0.1$ M, and $c_s = 1.0$ M, respectively from left to right. The snapshots show only a radius of 14σ from the center of the colloid and are cut in half, the color coding is the same as in Fig. 5.1. The applied electric field is from left to right in these pictures.

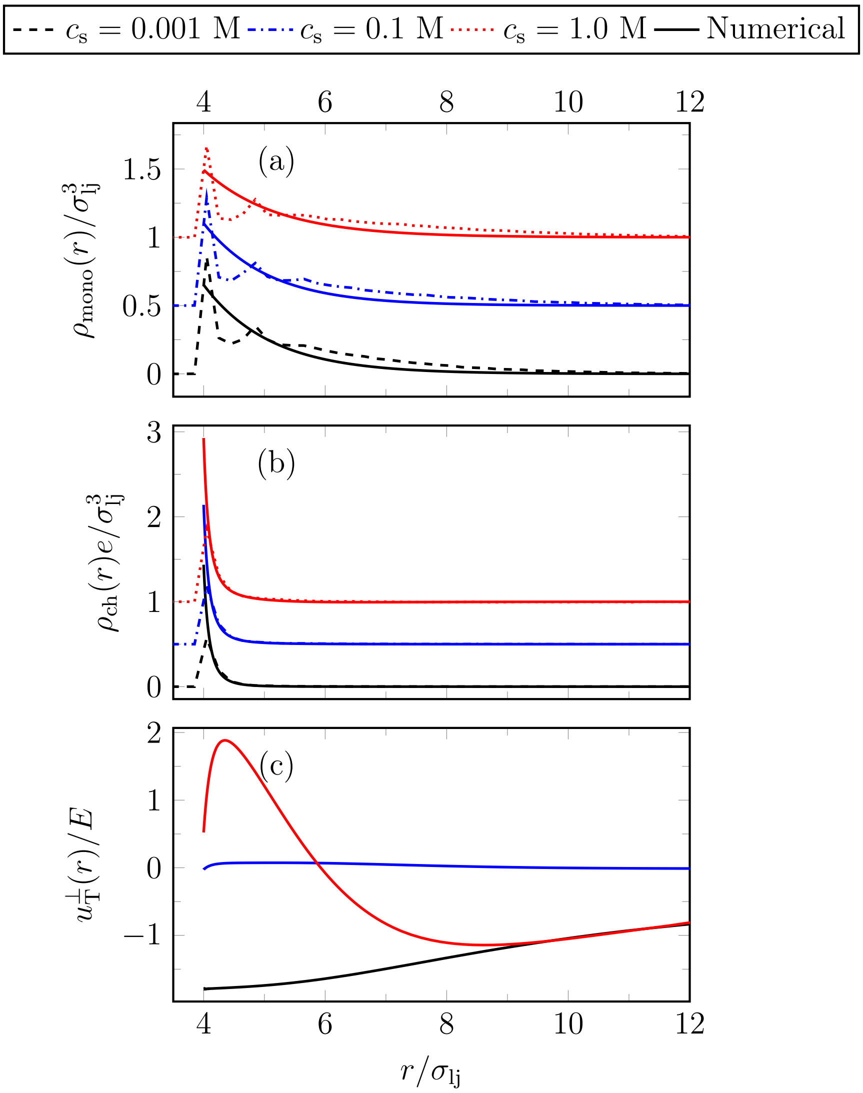

Figure 5.17: (a) Radial density profiles for $c_s = 0.001$ M (dashed black lines), $c_s = 0.1$ M (dash-dotted blue lines) and $c_s = 1$ M (dotted red lines) of the monomers $\rho_{\text{mono}}(r)$ and (b) fluid charge excluding the fixed charges $\rho_{\text{ch}}(r)$ for a composite with $Q_{\text{col}} = -90$ e and $\lambda = 0.1$ ($Q_{\text{net}} = -50$ e). Both monomer and fluid charge density profiles are shifted vertically by factors of 0.5 for the sake of visibility. The solid lines represent the numerical results. (c) The numerically obtained rescaled tangential fluid flow field as a function of the radial distance from the center of the colloid perpendicular to the applied electric field $u_{\text{T}}(r)/E$. The reference frame is fixed on the center of the colloid, i.e., the rescaled velocity values at the surface of the colloid correspond to the reduced electrophoretic mobilities and they converge to zero far from the surface.

5.4.6 Effect of Net Charge on the Electrophoretic Mobility of a Soft Colloid

In this subsection the effect of net charge on the electrophoretic mobility of a charged soft colloid is examined. The salt concentration is fixed at $c_\mathrm{s} = 0.5$ M and the charge fraction of the polyelectrolytes to $\lambda = 0.1$, while Q_col is varied. The net charge ranges from positive values where $Q_\mathrm{col} = 0$ e to extremely high negative values.

As can be seen in Fig. 5.18, the mobility changes sign long after the net charge goes from positive to negative. It is zero around $Q_\mathrm{net} = -110$ e and acquires small negative values for $Q_\mathrm{net} > -250$ e. At this salt concentration $\lambda_\mathrm{D} = 1.22\sigma_\mathrm{lj} < H$ and the system is in the polyelectrolyte-dominated regime. This is why the mobilities for low net charges are positive.

The monomer and fluid charge densities are shown in Fig. 5.19 (a) and (b), respectively. The strong electrostatic attraction at high net charges causes the positive ions to form layers at the surface and to form layers as can be seen in the snapshots at the top of Fig. 5.18. The strong layering of the counterions on the surface of the colloid makes them much less mobile. This is why the mobilities in Fig. 5.18 are very small even at extremely high net charges. This is unlikely to occur in experiments due to the impracticably high charge densities considered (tens of e/nm^2), but it nicely demonstrates the complex effects of grafted polyelectrolytes on the mobility of a charged surface.

Unlike in subsection 5.4.2, Eq. 5.5 only agrees with the simulations at low net charges and becomes largely negative when the net charge changes sign. The mean-field nature of Ohshima's theory, which neglects the finite size of the ions, causes the effect of the core to be overestimated. Whereas in the simulations the core's counterions are strongly layered and thus less mobile at high surface charges, in the theory they all accumulate at the surface and remain mobile.

The numerically calculated mobilities are also shown in Fig. 5.18 and they agree with simulation data only for the three lowest net charges. The reason is, as discussed in subsection 5.4.2, the absence of the excluded volume if ions in the underlying mean-field theory in the numerical approach. This results in the unreasonably large accumulations of positive ions right at the surface in Fig. 5.19 (b). For $Q_\mathrm{net} = -460$ e, the numerical fluid charge density gets as large as 80e/σ^3 (the y-axis only goes to 15e/σ for the sake of visibility). The EOF of the ions near the surface is, however, almost completely screened, which is why the numerical mobilities in Fig. 5.18 are independent of Q_col at high charges. It should be noted that the high charge densities, at which both the numerical results and the analytical approximations of Ohshima fail, are unrealistically high.

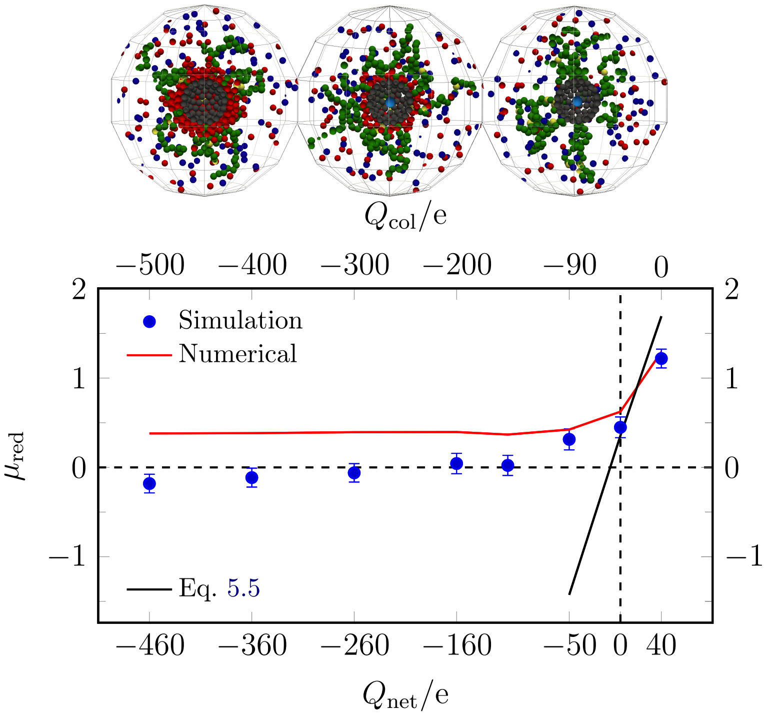

Figure 5.18: The reduced mobility μ_{red} as a function of the net charge of a soft colloid at fixed salt concentration $c_{\mathrm{s}} = 0.5$ M. The fraction of charged monomers is fixed, $\lambda = 0.1$ and the net charge is changed by changing the charge on the colloidal core. The results of the MD simulations (blue circles) are compared to the numerical results (red line), and Eq. 5.5. At the top three simulation snapshots are shown for $Q_{\mathrm{net}} = \{40, -160, -460\}$ e, respectively from left to right. The snapshots show only a radius of 14σ from the center of the colloid and are cut in half, the color coding is the same as in Fig. 5.1. The applied electric field is from left to right in these pictures.

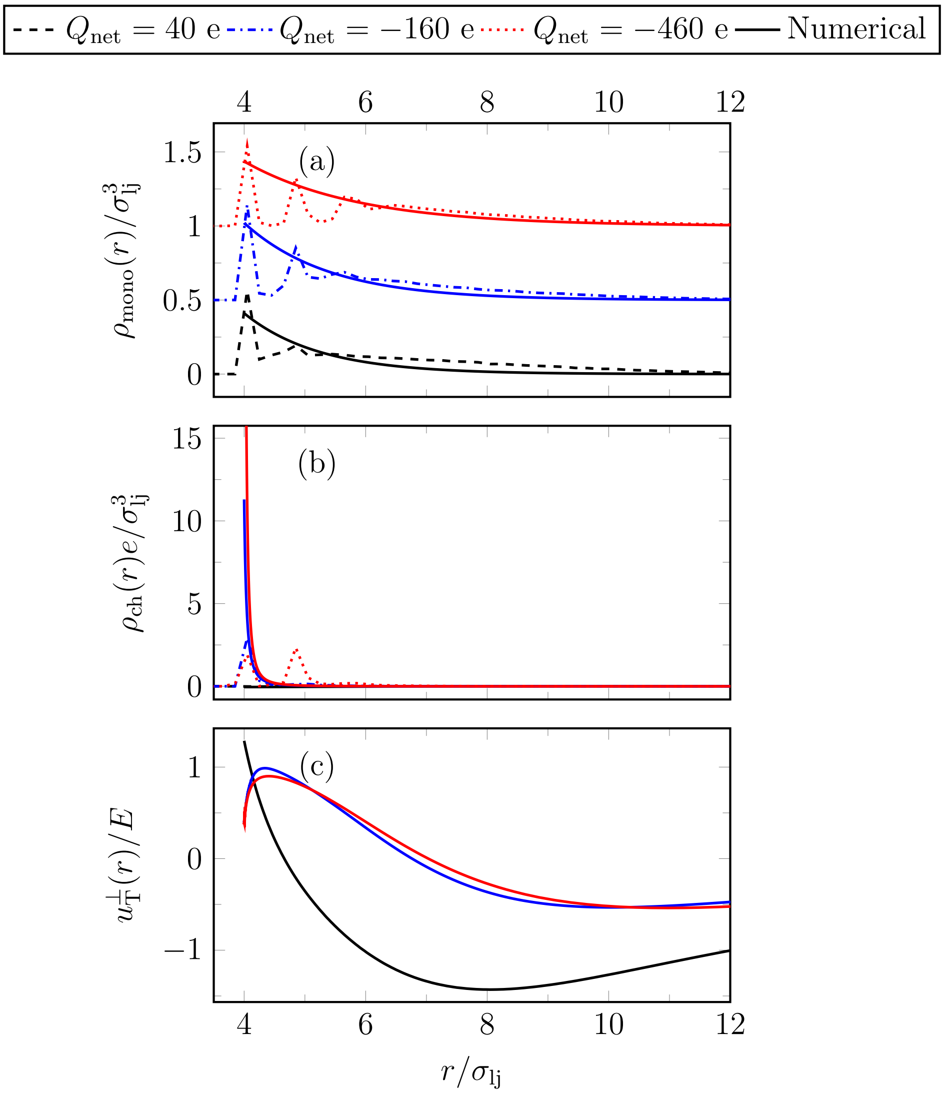

Figure 5.19: (a) Radial density profiles for $Q_{\text{net}} = 40$ e (dashed black lines), $Q_{\text{net}} = -160$ e (dash-dotted blue lines) and $Q_{\text{net}} = -460$ e (dotted red lines) of the monomers $\rho_{\text{mono}}(r)$ and (b) fluid charge excluding the fixed charges $\rho_{\text{ch}}(r)$ for $\lambda = 0.1$. The monomer density profiles are shifted vertically by factors of 0.5 for the sake of visibility. The solid lines represent the numerical results. (c) The numerically obtained rescaled tangential fluid flow field as a function of the radial distance from the center of the colloid perpendicular to the applied electric field $u_{\text{T}}(r)/E$. The reference frame is fixed on the center of the colloid, i.e., the rescaled velocity values at the surface of the colloid correspond to the reduced electrophoretic mobilities and they converge to zero far from the surface.

5.4.7 Effect of Charges on the Electrophoretic Mobility of a Soft Colloid with a Fixed Net-Charge

Finally, the effect of changing both the charge on the colloid and on the polyelectrolytes, such that the net charge of the composite remains fixed, is investigated on the mobility of a charged soft colloid. The net charge is fixed at $Q_{\text{net}} = -40$ e and the salt concentration at $c_{\text{s}} = 0.5$ M, i.e. the system is in the polyelectrolyte-dominated regime.

The results are shown in Fig. 5.20. For $Q_{\text{col}} = -40$ e the polyelectrolytes are neutral ($\lambda = 0$) and the soft colloid has a negative mobility with a small magnitude due to the screening the EOF by the brush. Increasing the charges, the mobility passes to positive values and increases with increasing the polyelectrolytes' charge up to $\lambda = 0.5$ ($Q_{\text{col}} = -240$ e). Upon further increase, the mobility decreases and becomes negative again around $Q_{\text{col}} = -280$ e ($\lambda = 0.6$). The reason can be understood from the simulation snapshots shown at the top of Fig. 5.20; the electrostatic attraction between the core and the polyelectrolytes causes the brush to compress, which in turn reduces the mobility. At $\lambda = 1.0$, all polyelectrolytes are collapsed on the core and their screening effect is negligible. The soft colloid behaves like a negatively charged bare colloid and moves in the opposite direction of the applied field.

The mobilities calculated by Ohshima's approximative expressions are also shown in Fig. 5.20. Eq. 5.6 (depicted by the dashed line) is linear in λ and does not take into account the effect of the underlying charged surface. This is true for the extreme case when λ_{D} is infinitely thin and the core's EOF is completely screened by the brush. Eq. 5.7 includes a $\mathcal{O}(1/\kappa)$ term for the contribution of the surface. The result (black solid line) agrees better with simulations, starting from small negative values and changing sign for $\lambda > 0$. Nevertheless, it fails to capture the nonlinearity of the mobility. The agreement worsen upon increasing the charges as the core's surface charge density increases and the brush thickness decreases. The more general expression is Eq. 5.5, which results in a nonlinear mobility curve but all values are negative. As mentioned in the previous subsections, this formula overestimates the contribution of the substrate. This is partly due to the absence of excluded volume in the theory; there are no layering effects and the ions penetrate the brush even at the highest charges. Besides, the ratio between the two terms in Eq. 5.5 depends on κ and is therefore affected by the fact that the apparent salt concentration is larger than 0.5 M since $Q_{\text{net}} \neq 0$ and the box size is finite. Inserting a higher salt concentration in the calculations improves the agreement at low charges, but worsens the high-charge results. It should also be kept in mind that this approximation is valid for low surface charge densities and polymer charge fractions. The reason why the shape of the mobility curve agrees with the simulation, is the increase in both Q_{col} as well as λ at the same time.

The numerical results are in good agreement with the simulations only for the three lowest charges. As discussed earlier, this is a consequence of the mean-field approach employed by the theory which neglects the finite sizes of the ions and monomers. As a results, the ions can penetrate the brush even at high charges, where the monomers are strongly layered, and aggregate at the surface. These effects can be seen in Fig. 5.21 (a and b). In the case of highest charges ($Q_{\text{col}} \leq -360$ e) the second peak in the simulated monomer densities become so large that densities are being overestimated by the fits, making the brush layer thicker in the numerical approach. On the other hand, the large accumulation of the core's counterions at it's surface causes the fluid charge density to become significantly negative at larger distances.

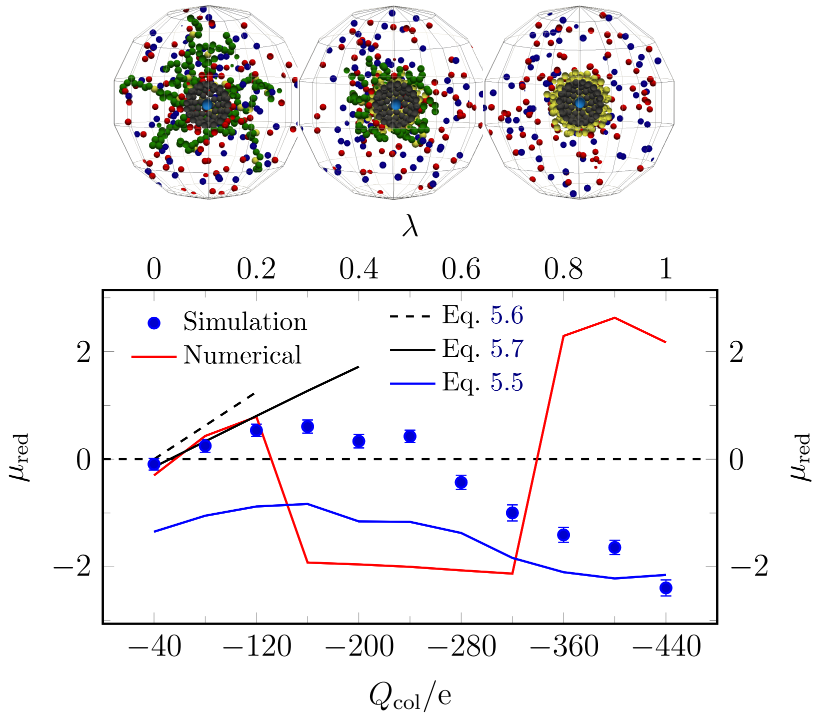

Figure 5.20: The reduced mobility μ_{red} as a function of the colloids charge Q_{col}, and the corresponding polyelectrolytes' charge fraction λ, for a soft colloid with fixed net charge $Q_{\mathrm{net}} = -40$ e at fixed salt concentration $c_{\mathrm{s}} = 0.5$ M. The results of the MD simulations (blue circles) are compared to the numerical results (red line), Eq. 5.6 (black dashed line), Eq. 5.7 (black line), and Eq. 5.5 (blue line). At the top three simulation snapshots are shown for $Q_{\mathrm{col}} = \{-80, -240, -440\}$ e, respectively from left to right. The snapshots show only a radius of $14\sigma_{\mathrm{lj}}$ from the center of the colloid and are cut in half, the color coding is the same as in Fig. 5.1. The applied electric field is from left to right in these pictures.

These combination of these two artifacts, leads to a large positive numerically calculated mobilities at high charges. The fluid flow fields shown in Fig. 5.21 (c) also reflect these effects.

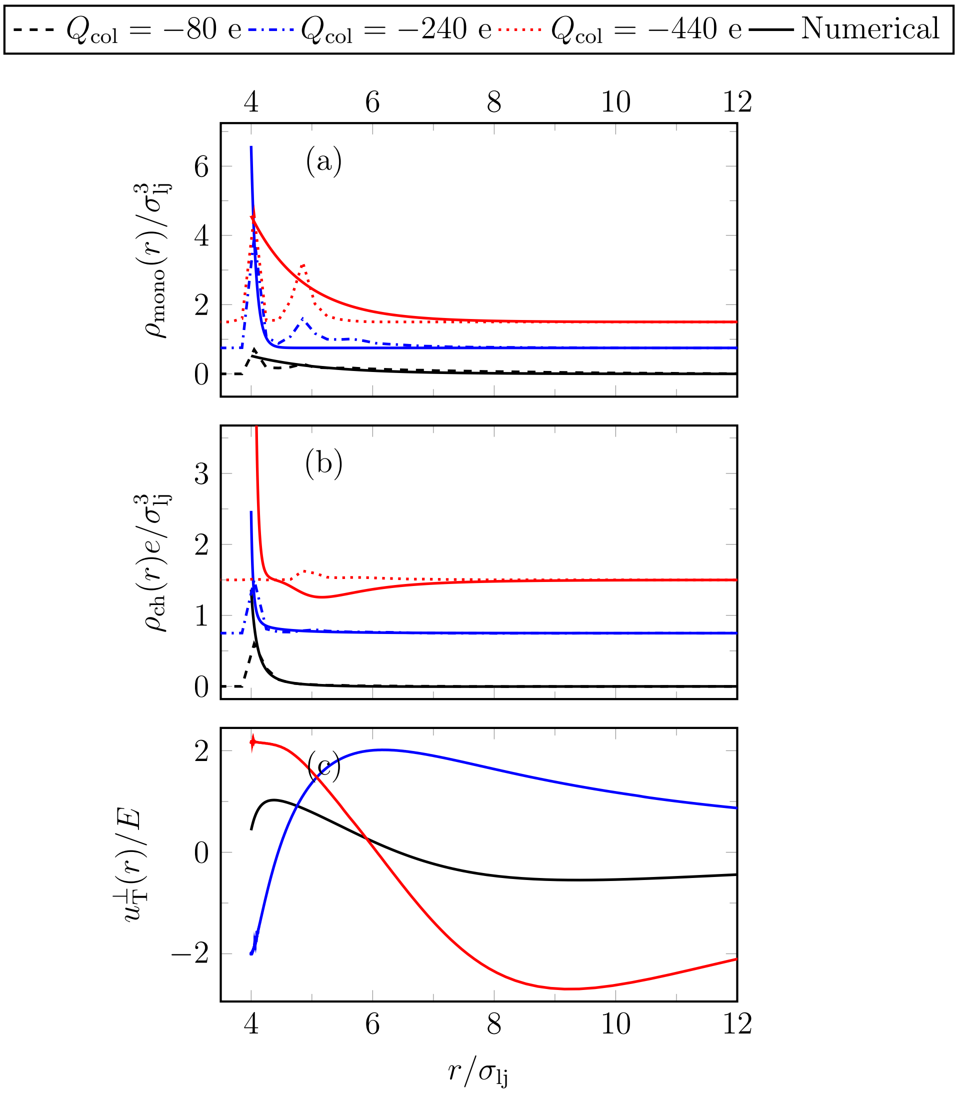

Figure 5.21: (a) Radial density profiles for $Q_{\text{col}} = -80$ e (dashed black lines), $Q_{\text{col}} = -240$ e (dash-dotted blue lines) and $Q_{\text{col}} = -440$ e (dotted red lines) of the monomers $\rho_{\text{mono}}(r)$ and (b) fluid charge excluding the fixed charges $\rho_{\text{ch}}(r)$ for a soft colloid with fixed net charge $Q_{\text{net}} = -40$ e. The density profiles are shifted vertically by factors of 0.75 for the sake of visibility. The solid lines represent the numerical results. (c) The numerically obtained rescaled tangential fluid flow field as a function of the radial distance from the center of the colloid perpendicular to the applied electric field $u_{\text{T}}(r)/E$. The reference frame is fixed on the center of the colloid, i.e., the rescaled velocity values at the surface of the colloid correspond to the reduced electrophoretic mobilities and they converge to zero far from the surface.

5.5 Summary

In this chapter ion-explicit MD simulations were used to measure the electrophoretic mobility of a polyelectrolyte-grafted colloid, referred to as a soft colloid. The results confirm that for thick coatings at high ionic strengths, the mobility is largely determined by the coating properties [41–43, 123, 125]. This is because the brush partially screens the EOF generated by the core's counterions, while its own counterions' EOF is less screened and in part reaches the bulk.

The phenomena observed in this chapter are a nice demonstration of the rather complex nature of electrokinetics in polymeric systems, namely how the behavior of such systems often runs contrary to simple intuition. These were explained by careful examination of the monomer and fluid charge density radial distributions and the ratio of the Debye length to the brush height.

It was shown here that as a consequent of the EOF screening, a neutral composite has a non-zero mobility in the presence of monovalent salt in the direction determined by the charge of the grafted polyelectrolytes. The investigation of the effect of charge on the mobility of neutral colloids at fixed salt concentration revealed that it remains polyelectrolyte-dominated even at very large charges where the electrostatic attraction causes the chains to collapse on the colloid. Furthermore, the validity of the scaling theory proposed by Harden *et al.* [120] was tested, according to which, in the limit of thick brushes and high salt concentrations, the system is equivalent to the superposition of *i*) a charged colloid coated with neutral polymers, and *ii*) a neutral colloid coated with charged polymers. This approach provided qualitatively similar results but significant quantitative deviations; only at the highest salt concentrations did the two subproblems have quantitatively similar mobilities. The reason is the electrostatic attraction of the grafted polyelectrolytes to the oppositely charged core, which changes their conformation and thereby their mobility. By increasing the salt concentration the attraction is screened and the two mobilities approach the same value.

Most importantly, it was shown that the mobility of a net-charged soft colloid changes sign with respect to *monovalent* salt concentration. The hydrodynamically driven mobility reversal is the result of a transition between two regimes and should not be mistaken for the mobility reversal of bare colloids in multivalent salt solution studied in Ch. 4. In the case of soft colloids, at low salt concentrations most counterions are outside of the brush and the mobility is determined by the net charge. In contrast, at high salt concentrations where the Debye layer is thin and most counterions accumulate close to the surface, their EOF is strongly screened and the polyelectrolytes dominate. The crossover occurs at the salt concentration for which the two important system length scales, namely the Debye layer and the brush height, are the same and the two EOFs cancel each other.

It was further shown that a net-negatively charged soft colloid in the brush regime, moves in the positive direction as determined by the positively charged grafted polymers, even at fairly large net charges. This is again due to strong screening of the EOF generated by the colloidal core's counterions, which are close to the surface. The soft colloid had only a negligible negative mobility, even at extremely high net negative charges, which is attributed to the crystallization of counterions around the colloid.

Finally, the effect of charge of the mobility of a soft colloid with *fixed* negative net charge was studied in the brush-dominated regime. The mobility increases with increasing the charges, passing from negative values in the case of neutral grafted polyelectrolytes to positive values. Upon further increase, the electrostatic attraction causes the polyelectrolytes to collapse on the core and thus the mobility to decrease. It eventually becomes negative again at high charges, acquiring large values when the polyelectrolytes are completely collapsed and the particle behaves like a bare colloid.

All simulation data were compared with approximate analytic expressions of Ohshima and the numerical results obtained from the computer program MPEK-0.02 provided by Reghan Hill. The numerical solver is based on the Darcy-Brinkman formalism and solved the modified EK equations for a spherical soft colloid [7]. The agreement between simulation and analytical expressions depended strongly on salt concentration and charge densities. On the other hand, the agreement between simulation and numerical results was very good except at unphysically large charge densities, where excluded volume plays an important role and the underlying mean-field theory breaks down. The good agreement at reasonable charge densities, confirms the validity of the Darcy-Brinkman equation combined with the Poisson-Nernst-Planck equation including a advective term to describe the electrokinetic behavior of such systems. The Darcy-Brinkman equation has previously been used in many theoretical studies that have been able to explain experimental results, however these studies still required fitting parameters. In contrast, here the necessary parameters were extracted directly from simulations. The results thus show that it does not require any additional factors in order to provide quantitatively accurate predictions.

6 Summary and Outlook

This thesis dealt with coarse-grained (CG) molecular dynamics (MD) simulations of colloidal electrophoresis where charged colloids in electrolytes move under the action of an externally applied electric field. All simulations were done using the Extensible Simulation Package for Research on Soft matter (ESPResSo) [168, 203]. In CG simulations, the less important degrees of freedom of the system are disregarded in favour of reducing the computational complexity in order to achieve larger sizes and longer times. The "coarse-grained" details are replaced by "effective" interactions, e.g. a molecule consisting of different atoms can be coarse-grained into a sphere with an effective size realized via a Lennard-Jones (LJ) potential.

Depending on the size of the colloids, which can range from nm to μm, and the detailed requirements of the study, different models can be used to simulate electrophoresis of colloids. For example, the solvent and/or the ions can be considered explicitly or implicitly, and the colloid itself might be modeled as a hard sphere, a raspberry-like particle, or even a flat charged surface. In this work, two different types of colloids are considered, namely bare and soft colloids. Electrophoresis of large bare colloids is the topic of Ch. 4, where the effect of mono-, di-, and trivalent salt concentration is investigated on the electrophoretic mobility. When the size of the colloid is orders of magnitude larger than the ions' size, as was the case for the particular colloids considered here, a simulation where all particles are explicit is computationally too expensive and not feasible. An efficient model has to necessitate extreme approximations without disregarding the important factors. In some methods a mean-field approach for the ions is used, but in case of multivalent salt, ion correlations usually play a crucial role which is not captured in implicit mean-field simulation methods. On the other hand, in the limit of a thin Debye layer, known as the Helmholtz-Smoluchowski (HS) limit, most of the excess counterions accumulate in the close vicinity of the particle, the local surface curvature can be ignored. The electrophoretic mobility becomes independent of the particle's shape and the planar geometry can be employed.

A novel method was developed here for simulating electrophoresis of large colloids in the HS limit. The colloid was modeled as a homogeneously charged flat surface, in contact with explicit ions in a "primitive model" implicit solvent. The solvent imitates a uniform dielectric medium at a specific temperature maintained via a thermostat, in our case, a Langevin thermostat. Using this method, colloids of μm size can be studied with explicit ions. The finite size of the ions is taken into account through Weeks-Chandler-Andersen (WCA) interactions with each other as well as the charged wall. Periodic boundary conditions were applied in the lateral directions. The Electrostatic Layer Correction (ELC) method[75, 92] combined with the particle-particle-particle mesh (P3M) algorithm [76, 77] were used to calculate the electrostatic interactions.

The drawback of the model is that the electrophoretic mobility cannot be measured directly by measuring the particle's velocity or equivalently the electro-osmotic flow (EOF) of the fluid in bulk. Instead, the $\zeta-$potential is calculated from simulations of the electric double layer in equilibrium, i.e. in the absence of an applied electric field and a numerical solver based on the standard electrokinetic model (SEM) [24, 25] is used to convert it into mobility. This can be done since in the limit of low applied field strength, which is usually the case in experiments, the distortion of the ionic cloud due to the field can be ignored. The SEM is based on a mean-field description of the electrolyte and solves the Stokes equation together with the Poisson-Nernst-Plank equation including a convective term in order to obtain the electrophoretic mobility. The fact that ion correlations are included in the $\zeta-$potential, compensates for the mean-field approach employed by SEM.

The proposed simulation method was applied to colloids used in two distinct sets of experiments. In the first set by Semenov et al. [4, 174, 175], *single* colloid electrophoresis is performed on latex colloids having a diameter of 2.23 μm and surface charge density $\sigma_\mathrm{s} = -0.31\ \mu\mathrm{C}/cm^2 \approx -0.02\ \mathrm{e/nm}^2$. The second set is performed by Elimelech et al. [5] using latex colloids of diameter 0.753 μm and surface charge density $\sigma_\mathrm{s} = -5.64\ \mu\mathrm{C}/cm^2 \approx -0.35\ \mathrm{e/nm}^2$. The validity of the planar geometry was verified for each by comparing the $\zeta-$potentials obtained from numerical solutions to the nonlinear Poisson-Boltzmann (PB) equation in planar and spherical geometries, using the experimental surface charge density and radius (in the spherical case) of the colloid in monovalent salt. In both cases, the results in the two geometries agreed extremely good and ensured the precision of the planar approximation. It was also found that for higher surface charge densities, this approximation can be used for smaller particles.

In the experiments considered, the electrophoretic mobility of latex colloids were measured in the presence of mono- (KCl), di- ($\mathrm{CaCl_2}$), and trivalent ($\mathrm{LaCl_3}$) salt of varying concentration. The main subject of interest in this part of this thesis was the mobility reversal observed in these experiments in the presence of trivalent salt. While the agreement between simulation and experiment was good in both cases for mono-, and divalent salt, the experimentally observed mobility reversal in trivalent salt could not be reproduced without further assumptions and the agreement was not even qualitative. Interestingly, the simulations revealed that in the cases under study, the electrostatic interactions *alone* are not strong enough and an *additional* specific adsorption is required for the mobility reversal to occur at the observed ionic strength. This indicated that La^{+3} ions experience a specific adsorption of strength of about $4\ k_\mathrm{B}T$ which we can be due to hydrolysis effects. Comparison of the ion density and potential profiles obtained from simulations and numerical solutions to the nonlinear PB for all three salt valencies showed that the correlations can be neglected in Semenov *et al.*'s system. For Elimelech *et al.*'s system which has a much higher surface charge density, the PB results deviate significantly from simulations for multivalent salt. The electrostatic coupling was found to be strong enough to cause charge inversion, nevertheless not strong enough to drive the observed mobility reversal without the specific adsorption. This shows that charge inversion is a *necessary but not sufficient* condition for mobility reversal.

In the second part of this thesis, the electrophoresis of polyelectrolyte-grafted colloids, referred to as soft colloids, in monovalent salt was investigated by means of CG MD simulations. The colloid as well as the ions are simulated explicitly, and full hydrodynamic interactions were taken into account using the lattice-Boltzmann (LB) algorithm [208] for the solvent.

The raspberry model [160, 205] was used for the colloid in order to insert its size in the hydrodynamic interactions and also for the purpose of grafting the polyelectrolytes on its surface. The raspberry model consists of a central particle, to which charge is assigned when needed, wrapped by a number of surface beads at a distance equal to the radius of the colloid. The point-particle coupling of each particle with the underlying LB fluid results in the finite size of the colloid. A fixed number of polymers all having the same degree of polymerization are grafted to randomly-chosen surface beads such that their distribution can be considered to be uniform. The connectivity of the monomers as well as the monomer-surface bead is maintained via Finitely Extensible Nonlinear Elastic (FENE) bonds. In cases were the polymers are charged, a fraction of the monomers are randomly chosen and given a unit positive charge. Periodic boundary conditions are applied in all directions and the P3M algorithm is used for the electrostatic interactions. The mobility is obtained directly by applying an external electric field and measuring the drift velocity.

The effect of salt concentration and charge on the mobility of both net-neutral and net-charged soft colloids was investigated. All the results were explained by careful examination of monomer and fluid charge density profiles. Simulations of a net-neutral soft colloid where the magnitude of the magnitude of the negative charge on the core is equal to the total charge on the polyelectrolytes, showed a non-zero mobility at higher salt concentrations. The grafted polymers partially screen the EOF generated by the ions in the Debye layer by exerting an extra drag force on them. This effects is stronger closer to the surface where the monomer number density is larger. At higher salt concentrations where the Debye length is smaller than the height of the brush, the contribution of the core to the total EOF is strongly screened, the polyelectrolytes' EOF dominates and the net-neutral particle acquires a positive mobility. This high salt regime is referred to as the polyelectrolyte-dominated regime in this work. Changing the charges on both the core and the polyelectrolytes at a fixed salt concentration in the polyelectrolyte-dominated regime showed that the mobility remains positive even at very high charges when all the chains are collapsed on the core because of the strong Coulomb attraction.

The most important finding of the second part of this thesis was the mobility reversal of a net-negative soft colloid with respect to *monovalent* salt concentration. At low salt concentrations, referred to as the net-charge-dominated regime in this work, the Debye length is larger than the brush height and most of the ions are outside the polymer layer where their EOF is not screened. The soft colloid behaves similar to a bare particle in this regime and its mobility is determined by its net charge. The transition from this regime to the polyelectrolyte-dominated regime upon increasing the salt concentration results in a mobility reversal. The origins of this mobility reversal differs fundamentally from the one studied in the first part and should not be mistaken for it. The effect of charge on the mobility was also investigated in the case of net-charged soft colloids in the polyelectrolyte-dominated regime. The results showed that the mobility becomes negative only at very high charges where the chains collapse due to the strong Coulomb attraction to the oppositely charged core.

All simulation results were compared to Ohshima's approximate analytical expressions [43, 44] as well as to results obtained from numerical solutions to the modified SEM for soft particles developed by Hill et al. [7]. In the modified SEM, Stokes equation is replaced by Darcy-Brinkman equation and the set of electrokinetic equations is solved in a manner similar to the SEM. The agreement between simulation and numerical results is very good, except when the charges are very large and the mean-field approach of the theory breaks down. The good agreement at reasonable charge densities, confirms the validity of the Darcy-Brinkman equation combined with the Poisson-Nernst-Planck equation including a advective term to describe the electrokinetic behavior of such systems. The agreement between Ohshima's analytical expressions and the simulations is restricted to salt concentrations for which the underlying assumptions of theory are met and to charge values where the finite size of the ions can be neglected.

Bibliography

[1] D. Frenkel and B. Smit, *Understanding Molecular Simulation*, Academic Press, San Diego, 2nd edn., 2002.

[2] M. Hecht and J. Harting, *Journal of Statistical Mechanics: Theory and Experiment*, 2010, **2010**, P01018.

[3] S. Raafatnia, O. A. Hickey, M. Sega and C. Holm, *Langmuir*, 2014, **30**, 1758–1767.

[4] I. Semenov, S. Raafatnia, M. Sega, V. Lobaskin, C. Holm and F. Kremer, *Phys. Rev. E*, 2013, **87**, 022302.

[5] M. Elimelech and C. R. O'Melia, *Colloids and Surfaces*, 1990, **44**, 165–178.

[6] F. Tessier and G. W. Slater, *Macromolecules*, 2006, **39**, 1250–1260.

[7] R. Hill, D. Saville and W. Russel, *Journal of Colloid and Interface Science*, 2003, **258**, 56–74.

[8] *Bakelite: The World's First Synthetic Plastic*, 2012, `http://www.acs.org/content/acs/en/education/whatischemistry/landmarks/bakelite.html`.

[9] A. Yethiraj and A. van Blaaderen, *Nature*, 2003, **421**, 513–517.

[10] A. Van Blaaderen, R. Ruel and P. Wiltzius, *Nature*, 1997, **385**, 321–324.

[11] K. Zahn, R. Lenke and G. Maret, *Phys. Rev. Lett.*, 1999, **82**, 2721–2724.

[12] A. E. Larsen and D. G. Grier, *Phys. Rev. Lett.*, 1996, **76**, 3862–3865.

[13] H. Löwen, *Physics Reports*, 1994, **237**, 249 – 324.

[14] P. Pusey and W. Van Megen, *Nature*, 1986, **320**, 340–342.

[15] M. Dijkstra, J. M. Brader and R. Evans, *Journal of Physics: Condensed Matter*, 1999, **11**, 10079.

[16] L. E. Sánchez-Díaz, C.-Y. Shew, X. Li, B. Wu, G. S. Smith and W.-R. Chen, *The Journal of Physical Chemistry B*, 2014, **118**, 6963–6971.

[17] P. L. Farber, B. Hochman, F. Furtado and L. M. Ferreira, *Medical Hypotheses*, 2014, **82**, 199 – 204.

[18] K. C. Grass, *Ph.D. thesis*, Goethe-Universität Frankfurt am Main, 2008.

[19] J. D. McPherson, M. Marra, L. Hillier, R. H. Waterston, A. Chinwalla, J. Wallis, M. Sekhon, K. Wylie, E. R. Mardis, R. K. Wilson, R. Fulton, T. A. Kucaba, C. Wagner-McPherson, W. B. Barbazuk, S. G. Gregory, S. J. Humphray, L. French, R. S. Evans, G. Bethel, A. Whittaker, J. L. Holden, O. T. McCann, A. Dunham, C. Soderlund, C. E. Scott, D. R. Bentley, G. Schuler, H. C. Chen, W. H. Jang, E. D. Green, J. R. Idol, V. V. B. Maduro, K. T. Montgomery, E. Lee, A. Miller, S. Emerling, R. Kucherlapati, R. Gibbs, S. Scherer, J. H. Gorrell, E. Sodergren, K. Clerc-Blankenburg, P. Tabor, S. Naylor, D. Garcia, P. J. de Jong, J. J. Catanese, N. Nowak, K. Osoegawa, S. Z. Qin, L. Rowen, A. Madan, M. Dors, L. Hood, B. Trask, C. Friedman, H. Massa, V. G. Cheung, I. R. Kirsch, T. Reid, R. Yonescu, J. Weissenbach, T. Bruls, R. Heilig, E. Branscomb, A. Olsen, N. Doggett, J. F. Cheng, T. Hawkins, R. M. Myers, J. Shang, L. Ramirez, J. Schmutz, O. Velasquez, K. Dixon, N. E. Stone, D. R. Cox, D. Haussler, W. J. Kent, T. Furey, S. Rogic, S. Kennedy, S. Jones, A. Rosenthal, G. P. Wen, M. Schilhabel, G. Gloeckner, G. Nyakatura, R. Siebert, B. Schlegelberger, J. Korenburg, X. N. Chen, A. Fujiyama, M. Hattori, A. Toyoda, T. Yada, H. S. Park, Y. Sakaki, N. Shimizu, S. Asakawa, K. Kawasaki, T. Sasaki, A. Shintani, A. Shimizu, K. Shibuya, J. Kudoh, S. Minoshima, J. Ramser, P. Seranski, C. Hoff, A. Poustka, R. Reinhardt and H. Lehrach, *Nature*, 2001, **409**, 934–941.

[20] R. Ottewill and J. Shaw, *Journal of Colloid and Interface Science*, 1968, **26**, 110–119.

[21] C. Labbez, A. Nonat, I. Pochard and B. Jonsson, *Journal of Colloid and Interface Science*, 2007, **309**, 303–307.

[22] A. Martin-Molina, J. A. Maroto-Centeno, R. Hidalgo-Alvarez and M. Quesada-Perez, *Colloids Surf. A*, 2008, **319**, 103–108.

[23] C. Schneider, M. Hanisch, B. Wedel, A. Jusufi and M. Ballauff, *Journal of Colloid and Interface Science*, 2011, **358**, 62–67.

[24] P. H. Wiersema, A. L. Loeb and J. T. Overbeek, *Journal of Colloid and Interface Science*, 1966, **22**, 78.

[25] R. W. O'Brien and L. R. White, *J. Chem. Soc. Faraday Trans.*, 1978, **74**, 1607.

[26] M. A. Swartz and M. E. Fleury, *Annual Review of Biomedical Engineering*, 2007, **9**, 229–256.

[27] S. Levine, M. Levine, K. Sharp and D. Brooks, *Biophysical Journal*, 1983, **42**, 127 – 135.

[28] J. F. Duval and F. Gaboriaud, *Current Opinion in Colloid & Interface Science*, 2010, **15**, 184–195.

[29] A. J. de Kerchove and M. Elimelech, *Langmuir*, 2005, **21**, 6462–6472.

[30] R. J. Emerson and T. A. Camesano, *Applied and environmental microbiology*, 2004, **70**, 6012–6022.

[31] I. S. Lee, M. S. Cho and H. J. Choi, *Polymer*, 2005, **46**, 1317 – 1321.

[32] Y. D. Kim and D. H. Park, *Synthetic Metals*, 2004, **142**, 147 – 151.

[33] T. L. Doane, C.-H. Chuang, R. J. Hill and C. Burda, *Accounts of Chemical Research*, 2012, **45**, 317–326.

[34] M. Yamato, C. Konno, M. Utsumi, A. Kikuchi and T. Okano, *Biomaterials*, 2002, **23**, 561 – 567.

[35] Y. Akiyama, A. Kikuchi, M. Yamato and T. Okano, *Langmuir*, 2004, **20**, 5506–5511.

[36] J. F. L. Duval, K. J. Wilkinson, H. P. van Leeuwen and J. Buffle, *Environmental Science & Technology*, 2005, **39**, 6435–6445.

[37] V. P. Torchilin, *The AAPS Journal*, 2007, **9**, E128–E147.

[38] K. Y. Win and S.-S. Feng, *Biomaterials*, 2005, **26**, 2713 – 2722.

[39] V. Toncheva, M. A. Wolfert, P. R. Dash, D. Oupicky, K. Ulbrich, L. W. Seymour and E. H. Schacht, *Biochimica et Biophysica Acta (BBA) - General Subjects*, 1998, **1380**, 354 – 368.

[40] H. J. Kaper, H. J. Busscher and W. Norde, *Journal of Biomaterials Science, Polymer Edition*, 2003, **14**, 313–324.

[41] G. Danger, M. Ramonda and H. Cottet, *Electrophoresis*, 2007, **28**, 925–931.

[42] O. A. Hickey, C. Holm, J. L. Harden and G. W. Slater, *Macromolecules*, 2011, **44**, 9455–9463.

[43] H. Ohshima, M. Nakamura and T. Kondo, *Colloid and Polymer Science*, 1992, **270**, 873–877.

[44] H. Ohshima, *Colloid and Polymer Science*, 2007, **285**, 1411–1421.

[45] M. P. Allen and D. J. Tildesley, *Computer Simulation of Liquids*, Clarendon Press, Oxford, 1st edn., 1987.

[46] R. Pathria, *Statistical Mechanics*, Elsevier Science, 2nd edn., 1996.

[47] L. Verlet, *Physical Review*, 1967, **159**, 98.

[48] R. W. Hockney and J. W. Eastwood, *Computer Simulations using Particles*, McGraw-Hill, New York, 1981.

[49] P. Gonnet, *Journal of Computational Chemistry*, 2012, **33**, 76–81.

[50] J. D. Weeks, D. Chandler and H. C. Andersen, *Journal of Chemical Physics*, 1971, **54**, 5237.

[51] T. Soddemann, B. Dünweg and K. Kremer, *European Physical Journal E: Soft Matter*, 2001, **6**, 409.

[52] G. S. Grest and K. Kremer, *Phys. Rev. A*, 1986, **33**, 3628–31.

[53] R. A. L. Jones, *Soft Condensed Matter*, Oxford University Press, Great Clarendon Street, Oxford OX2 6DP, 2002.

[54] A. S. Almgren, J. B. Bell, C. A. Rendleman and M. Zingale, *The Astrophysical Journal*, 2006, **637**, 922.

[55] P. J. Hoogerbrugge and J. M. V. A. Koelman, *Europhysics Letters*, 1992, **19**, 155–160.

[56] A. Malevanets and R. Kapral, *Journal of Chemical Physics*, 1999, **110**, 8605–8613.

[57] A. J. C. Ladd, *Phys. Fluids A*, 1993, **5**, 299–310.

[58] P. Ahlrichs and B. Dünweg, *Journal of Chemical Physics*, 1999, **111**, 8225–8239.

[59] B. Dünweg and A. J. C. Ladd, in *Advanced Computer Simulation Approaches for Soft Matter Sciences III*, Springer-Verlag Berlin, Berlin, Germany, 2009, vol. 221, pp. 89–166.

[60] B. J. Alder and T. E. Wainwright, *Phys. Rev. A*, 1970, **1**, 18–21.

[61] I. Pagonabarraga, B. Rotenberg and D. Frenkel, *Physical Chemistry Chemical Physics*, 2010, **12**, 9566–9580.

[62] J.-F. Dufrêche, O. Bernard, S. Durand-Vidal and P. Turq, *The Journal of Physical Chemistry B*, 2005, **109**, 9873–9884.

[63] R. Benzi, S. Succi and M. Vergassola, *Physics Reports*, 1992, **222**, 145–197.

[64] S. Chen and G. D. Doolen, *Annual review of fluid mechanics*, 1998, **30**, 329–364.

[65] P. L. Bhatnagar, E. P. Gross and M. Krook, *Physical Review*, 1954, **94**, 511.

[66] D. d'Humieres, *Philosophical Transactions of the Royal Society of London. Series A: Mathematical, Physical and Engineering Sciences*, 2002, **360**, 437–451.

[67] L. D. Landau and E. M. Lifshitz, *Fluid Mechanics: Landau and Lifshitz: Course of Theoretical Physics*, Elsevier, 2013, vol. 6.

[68] M. Feig and C. L. B. III, *Current Opinion in Structural Biology*, 2004, **14**, 217 – 224.

[69] N. A. Baker, *Current Opinion in Structural Biology*, 2005, **15**, 137 – 143.

[70] A. Einstein, *Annalen der physik*, 1905, **322**, 549–560.

[71] A. Einstein, *Annalen der Physik*, 1906, **19**, 371–381.

[72] R. W. Hockney and J. W. Eastwood, *Computer Simulation Using Particles*, IOP, London, 1988.

[73] A. Arnold and C. Holm, in *Advanced Computer Simulation Approaches for Soft Matter Sciences II*, ed. C. Holm and K. Kremer, Springer, Berlin, 2005, vol. II, pp. 59–109.

[74] V. Ballenegger, J. J. Cerdà and C. Holm, *Computer Physics Communications*, 2011, **182**, 1919–1923.

[75] A. Arnold, J. de Joannis and C. Holm, *Journal of Chemical Physics*, 2002, **117**, 2496–2502.

[76] M. Deserno and C. Holm, *Journal of Chemical Physics*, 1998, **109**, 7678.

[77] M. Deserno and C. Holm, *Journal of Chemical Physics*, 1998, **109**, 7694.

[78] P. P. Ewald, *Annales de Physique*, 1921, **369**, 253–287.

[79] D. M. Heyes and F. van Swol, *Journal of Chemical Physics*, 1981, **75**, 5051.

[80] P. H. Huenenberger, *Journal of Chemical Physics*, 2000, **113**, 10464–10476.

[81] H. J. C. Berendsen, Computer Simulation of Biomolecular Systems, The Netherlands, 1993, pp. 161–81.

[82] J. W. Perram, H. G. Petersen and S. W. de Leeuw, *J. Mol. Phys.*, 1988, **65**, 875–893.

[83] F. Dommert and C. Holm, *Physical Chemistry Chemical Physics*, 2013, **15**, 2037–2049.

[84] T. Darden, D. York and L. Pedersen, *Journal of Chemical Physics*, 1993, **98**, 10089–10092.

[85] U. Essmann, L. Perera, M. L. Berkowitz, T. Darden, H. Lee and L. Pedersen, *Journal of Chemical Physics*, 1995, **103**, 8577.

[86] B. A. Luty, I. G. Tironi and W. F. van Gunsteren, *J. Chem. Phys*, 1995, **103**, 3014–21.

[87] I. J. Schoenberg, *Cardinal Spline Interpolation*, Society for Industrial and Applied Mathematics, Philadelphia, 1973.

[88] R. Strebel, *Dissertation*, ETH Zürich, 1999.

[89] R. Strebel and R. Sperb, *Molecular Simulation*, 2001, **27**, 61–74.

[90] A. Arnold and C. Holm, *Journal of Chemical Physics*, 2005, **123**, 144103.

[91] A. Arnold and C. Holm, *Computer Physics Communications*, 2002, **148**, 327–348.

[92] J. de Joannis, A. Arnold and C. Holm, *Journal of Chemical Physics*, 2002, **117**, 2503–2512.

[93] A. Arnold and C. Holm, *Chemical Physics Letters*, 2002, **354**, 324–330.

[94] I.-C. Yeh and M. L. Berkowitz, *Journal of Chemical Physics*, 1999, **111**, 3155–3162.

[95] S. W. de Leeuw, J. W. Perram and E. R. Smith, *Proceedings of the Royal Society of London. Series A: Mathematics and Physical Sciences*, 1980, **373**, 27–56.

[96] S. W. de Leeuw, J. W. Perram and E. R. Smith, *Proceedings of the Royal Society of London. Series A: Mathematics and Physical Sciences*, 1980, **373**, 57–66.

[97] J.-M. Caillol, *Journal of Chemical Physics*, 1994, **101**, 6080–6090.

[98] E. R. Smith, *Proc. R. Soc. Lond. A*, 1981, **375**, 475–505.

[99] A. Delgado, F. González-Caballero, R. Hunter, L. Koopal and J. Lyklema, *Journal of Colloid and Interface Science*, 2007, **309**, 194 – 224.

[100] A. Delgado, F. González-Caballero, R. Hunter, L. Koopal and J. Lyklema, *Pure and Applied Chemistry*, 2005, **77**, 1753–1805.

[101] *Solid-Liquid Interfaces*, ed. J. J. Lyklema, A. de Keizer, B. Bijsterbosch, G. Fleer and M. C. Stuart, Academic Press, 1995, vol. 2, ch. 3, 4.

[102] P. Debye and E. Hückel, *Physikalische Zeitschrift*, 1923, **24**, 185.

[103] G. L. Gouy, *J. de Phys.*, 1910, **9**, 457.

[104] D. L. Chapman, *Philosophical Magazine*, 1913, **25**, 475.

[105] H. Butt, K. Graf and M. Kappl, *Physics and Chemistry of Interfaces*, Wiley, 2006.

[106] D. Haydon, *Biochimica et Biophysica Acta*, 1961, **50**, 450 – 457.

[107] D. Haydon, *Biochimica et Biophysica Acta*, 1961, **50**, 457 – 462.

[108] L. Weiss, *The Journal of Cell Biology*, 1965, **26**, 735–739.

[109] J. Lyklema, S. Rovillard and J. De Coninck, *Langmuir*, 1998, **14**, 5659–5663.

[110] L. Lizana and A. Y. Grosberg, *EPL (Europhysics Letters)*, 2013, **104**, 68004.

[111] B. Dünweg, V. Lobaskin, K. Seethalakshmy-Hariharan and C. Holm, *Journal of Physics: Condensed Matter*, 2008, **20**, 404214.

[112] W. B. Russel, D. A. Saville and W. R. Schowalter, *Colloidal Dispersions*, Cambridge University Press, Cambridge, UK, 1989.

[113] E. Hückel, *Phys. Z.*, 1924, **25**, 204.

[114] F. Morrison, Jr., *Journal of Colloid and Interface Science*, 1970, **34**, 210–214.

[115] R. W. O'Brien and R. J. Hunter, *Canadian Journal of Chemistry*, 1981, **59**, 1878–1887.

[116] S. Dukhin and B. Derjaguin, in *Electrokinetic Phenomena*, ed. E. Matijević, John Wiley, New York, 1974, vol. 7, ch. 2.

[117] D. C. Henry, *Proceedings of the Royal Society of London. Series A*, 1931, **133**, 106–129.

[118] M. Evers, N. Garbow, D. Hessinger and T. Palberg, *Phys. Rev. E*, 1998, **57**, 6774–6784.

[119] H. Brinkman, *Applied Scientific Research*, 1949, **1**, 27–34.

[120] J. L. Harden, D. Long and A. Ajdari, *Langmuir*, 2001, **17**, 705–715.

[121] R. J. Hill, D. Saville and W. Russel, *Journal of Colloid and Interface Science*, 2003, **263**, 478 – 497.

[122] H. Ohshima, *Colloids and Surfaces A: Physicochemical and Engineering Aspects*, 1995, **103**, 249 – 255.

[123] H. Ohshima, *ELECTROPHORESIS*, 2006, **27**, 526–533.

[124] A. Ajdari, *Phys. Rev. Lett.*, 1995, **75**, 755–758.

[125] R. J. Hill and D. A. Saville, *Colloids Surf. A*, 2005, **267**, 31–49.

[126] S. Bhattacharyya, S. Dhinakaran and A. Khalili, *Chemical Engineering Science*, 2006, **61**, 4451 – 4461.

[127] S. Bhattacharyya and P. P. Gopmandal, *Soft Matter*, 2013, **9**, 1871–1884.

[128] M. Rubinstein and R. Colby, *Polymer Physics*, OUP Oxford, 2003.

[129] P. G. de Gennes, *Scaling Concepts in Polymer Physics*, Cornell University Press, Ithaca, NY, 1979.

[130] I. Teraoka, *Polymer Solutions: An Introduction to Physical Properties*, Wiley, 2002.

[131] L. J. Fetters, N. Hadjichristidis, J. S. Lindner and J. W. Mays, *Journal of Physical and Chemical Reference Data*, 1994, **23**, 619–640.

[132] J. C. Le Guillou and J. Zinn-Justin, *Phys. Rev. Lett.*, 1977, **39**, 95–98.

[133] J. Cloizeaux and G. Jannink, *Polymers in solution: their modelling and structure*, Clarendon Press, 1990.

[134] J. F. L. Duval and H. P. van Leeuwen, *Langmuir*, 2004, **20**, 10324–10336.

[135] J. F. L. Duval, *Langmuir*, 2005, **21**, 3247–3258.

[136] J. F. L. Duval and H. Ohshima, *Langmuir*, 2006, **22**, 3533–3546.

[137] O. Vesterberg, *ELECTROPHORESIS*, 1993, **14**, 1243–1249.

[138] A. Tiselius, *Trans. Faraday Soc.*, 1937, **33**, 524–531.

[139] D. Kim and E. Darve, *Phys. Rev. E*, 2006, **73**, 051203.

[140] H. Ohshima, T. W. Healy and L. R. White, *J. Chem. Soc., Faraday Trans. 2*, 1983, **79**, 1613–1628.

[141] A. Martin-Molina, C. Calero, J. Faraudo, M. Quesada-Perez, A. Travesset and R. Hidalgo-Alvarez, *Soft Matter*, 2009, **5**, 1350–1353.

[142] J. Lyklema, *Fundamentals of Interface and Colloid Science*, Acamdemic Press, USA, 1st edn., 1991, vol. 2.

[143] M. Lozada-Cassou, E. González-Tovar and W. Olivares, *Phys. Rev. E*, 1999, **60**, R17–R20.

[144] A. G. Moreira and R. R. Netz, *Europhysics Letters*, 2000, **52**, 705–711.

[145] M. Deserno, F. Jiménez-Ángeles, C. Holm and M. Lozada-Cassou, *Journal Phys. Chem. B*, 2001, **105**, 10983–10991.

[146] M. Tanaka and A. Y. Grosberg, *Euro. Phys. J. E*, 2002, **7**, 371–379.

[147] A. Naji and R. R. Netz, *Physical Review Letters*, 2005, **95**, 185703.

[148] A. Naji, S. Jungblut, A. G. Moreira and R. R. Netz, *Physica A: Statistical Mechanics and its Applications*, 2005, **352**, 131 – 170.

[149] M. Quesada-Perez, A. Martin-Molina and R. Hidalgo-Alvarez, *Langmuir*, 2005, **21**, 9231–9237.

[150] P.-Y. Hsiao and E. Luijten, *Physical Review Letters*, 2006, **97**, 148301.

[151] A. Diehl and Y. Levin, *Journal of Chemical Physics*, 2006, **125**, 054902.

[152] A. Kubíčková, T. Křížek, P. Coufal, M. Vazdar, E. Wernersson, J. Heyda and P. Jungwirth, *Physical Review Letters*, 2012, **108**, 186101.

[153] J. Lyklema, *Colloids and Surfaces A: Physicochemical and Engineering Aspects*, 2006, **291**, 3 – 12.

[154] Y. Levin, *Rep. Prog. Phys.*, 2002, **65**, 1577–1632.

[155] A. Y. Grosberg, T. T. Nguyen and B. I. Shklovskii, *Rev. Mod. Phys*, 2002, **74**, 329.

[156] J. Lyklema and T. Golub, *Croatica Chemica Acta*, 2007, **80**, 303–311.

[157] D. Bastos and F. Nieves, *Colloid and Polymer Science*, 1993, **271**, 860–867.

[158] M. L. Jiménez, Á. V. Delgado and J. Lyklema, *Langmuir*, 2012, **28**, 6786–6793.

[159] J. Zhou and F. Schmid, *The European Physical Journal E*, 2013, **36**, 33.

[160] V. Lobaskin, B. Dünweg and C. Holm, *Journal of Physics: Condensed Matter*, 2004, **16**, S4063–S4073.

[161] V. Lobaskin, B. Dünweg, M. Medebach, T. Palberg and C. Holm, *Physical Review Letters*, 2007, **98**, 176105.

[162] A. Chatterji and J. Horbach, *Journal of Chemical Physics*, 2007, **126**, 064907.

[163] F. Capuani, I. Pagonabarraga and D. Frenkel, *The Journal of chemical physics*, 2004, **121**, 973.

[164] K. Kim, Y. Nakayama and R. Yamamoto, *Physical Review Letters*, 2006, **96**, 208302.

[165] G. Giupponi and I. Pagonabarraga, *Physical Review Letters*, 2011, **106**, 248304.

[166] R. Schmitz and B. Dünweg, *Journal of Physics: Condensed Matter*, 2012, **24**, 464111.

[167] B. I. Shklovskii, *Phys. Rev. E*, 1999, **60**, 5802–5811.

[168] H. J. Limbach, A. Arnold, B. A. Mann and C. Holm, *Comp. Phys. Comm.*, 2006, **174**, 704–727.

[169] L. Bocquet and J.-L. Barrat, *Soft Matter*, 2007, **3**, 685–693.

[170] J. Huang, R. R. Koepsel, H. Murata, W. Wu, S. B. Lee, T. Kowalewski, A. J. Russell and K. Matyjaszewski, *Langmuir*, 2008, **24**, 6785–6795.

[171] O. Bäumchen and K. Jacobs, *Soft Matter*, 2010, **6**, 6028–6035.

[172] M. Sega, M. Sbragaglia, L. Biferale and S. Succi, *Soft Matter*, 2013, **9**, 8526–8531.

[173] L. Joly, C. Ybert, E. Trizac and L. Bocquet, *J. Chem. Phys.*, 2006, **125**, 204716.

[174] I. Semenov, O. Otto, G. Stober, P. Papadopoulos, U. F. Keyser and F. Kremer, *Journal of Colloid and Interface Science*, 2009, **337**, 260–264.

[175] I. Semenov, P. Papadopoulos, G. Stober and F. Kremer, *J. Phys. : Condensed Matter*, 2010, **22**, 494109.

[176] R. R. Netz and H. Orland, *Europhysics Letters*, 1999, **45**, 726–732.

[177] R. Messina, C. Holm and K. Kremer, *Euro. Phys. J. E.*, 2001, **4**, 363–370.

[178] A. G. Moreira and R. R. Netz, *Europhysics Letters*, 2002, **57**, 911–917.

[179] D. B. Lukatsky, S. A. Safran, A. W. C. Lau and P. Pincus, *EPL (Europhysics Letters)*, 2002, **58**, 785.

[180] R. Messina, *Physica A*, 2002, **308**, 59–79.

[181] M. Löbbus, H. P. van Leeuwen and J. Lyklema, *Colloids and Surfaces, A: Physicochemical and Engineering Aspects*, 2000, **161**, 103–113.

[182] C. Li and P. Somasundaran, *Colloids and Surfaces A: Physicochemical and Engineering Aspects*, 1993, **81**, 13–15.

[183] D. Wagman, W. Evans, V. Parker and R. Schumm, *Journal of Physical Chemistry Reference Data*, 1982, **11**, .

[184] M. Antonietti and L. Vorwerg, *Colloid and Polymer Science*, 1997, **275**, 883–887.

[185] H. Boroudjerdi, Y.-W. Kim, A. Naji, R. R. Netz, X. Schlagberger and A. Serr, *Physics Reports*, 2005, **416**, 129–199.

[186] O. Punkkinen, A. Naji, R. Podgornik, I. Vattulainen and P.-L. Hansen, *EPL (Europhysics Letters)*, 2008, **82**, 48001.

[187] J. de Graaf, N. Boon, M. Dijkstra and R. van Roij, *Journal of Chemical Physics*, 2012, **137**, 104910–12.

[188] A. S. Khair and T. M. Squires, *Physics of Fluids (1994-present)*, 2009, **21**, 042001.

[189] B. Luan and A. Aksimentiev, *Soft Matter*, 2010, **6**, 243–246.

[190] S. Raafatnia, O. A. Hickey and C. Holm, *Phys. Rev. Lett.*, 2014, **113**, 238301.

[191] Q. Cao, C. Zuo, L. Li, Y. Zhang and G. Yan, *Journal of Polymer Science Part B: Polymer Physics*, 2012, **50**, 805–811.

[192] R. Qiao, *Langmuir*, 2006, **22**, 7096–7100.

[193] Y. Zuo, G. Wang, Y. Yu, C. Zuo, Z. Liu, D. Hu and Y. Wang, *Microfluidics and Nanofluidics*, 2014, 1–9.

[194] S. Gangwal, O. J. Cayre, M. Z. Bazant and O. D. Velev, *Physical Review Letters*, 2008, **100**, 058302.

[195] M. Z. Bazant, M. S. Kilic, B. D. Storey and A. Ajdari, *Advances in Colloid and Interface Science*, 2009, **152**, 48–88.

[196] A. Ajdari, *Physical Review E*, 2000, **61**, R45–R48.

[197] D. Long, A. V. Dobrynin, M. Rubinstein and A. Ajdari, *Journal of Chemical Physics*, 1998, **108**, 1234–1244.

[198] M. Z. Bazant and Y. Ben, *Lab on a Chip*, 2006, **6**, 1455–1461.

[199] D. Belder, H. Husmann and J. Warnke, *Electrophoresis*, 2001, **22**, 666–672.

[200] C. Legido-Quigley, N. D. Marlin, V. Melin, A. Manz and N. W. Smith, *Electrophoresis*, 2003, **24**, 917–944.

[201] B. A. Buchholz, W. Shi and A. E. Barron, *Electrophoresis*, 2002, **23**, 1398–1409.

[202] S. Raafatnia, O. A. Hickey and C. Holm, *Macromolecules*, 2015.

[203] A. Arnold, O. Lenz, S. Kesselheim, R. Weeber, F. Fahrenberger, D. Röhm, P. Košovan and C. Holm, Meshfree Methods for Partial Differential Equations VI, 2013, pp. 1–23.

[204] D. Long and A. Ajdari, *European Physical Journal E*, 2001, **4**, 29–32.

[205] V. Lobaskin and B. Dünweg, *New Journal of Physics*, 2004, **6**, 54.

[206] J. Zhou and F. Schmid, *The European Physical Journal Special Topics*, 2013, **222**, 2911–2922.

[207] P. Ahlrichs and B. Dünweg, *International Journal of Modern Physics C*, 1998, **9**, 1429–1438.

[208] D. Röhm and A. Arnold, *The European Physical Journal Special Topics*, 2012, **210**, 89–100.

[209] K. Grass, U. Böhme, U. Scheler, H. Cottet and C. Holm, *Physical Review Letters*, 2008, **100**, 096104.

[210] O. A. Hickey, C. Holm, J. L. Harden and G. W. Slater, *Physical Review Letters*, 2010, **105**, 148301.

[211] F. Farahpour, A. Maleknejad, F. Varnik and M. R. Ejtehadi, *Soft Matter*, 2013, **9**, 2750–2759.

[212] H. Ohshima, *Current Opinion in Colloid & Interface Science*, 2013, **18**, 73 – 82.

[213] D. A. Hoagland, E. Arvanitidou and C. Welch, *Macromolecules*, 1999, **32**, 6180–6190.

[214] J. L. Viovy, *Reviews of Modern Physics*, 2000, **72**, 813–872.

[215] S. Frank and R. G. Winkler, *Europhysics Letters*, 2008, **83**, 38004.

[216] O. A. Hickey, T. N. Shendruk, J. L. Harden and G. W. Slater, *Physical Review Letters*, 2012, **109**, 098302.

[217] K. Grass and C. Holm, *Soft Matter*, 2009, **5**, 2079–2092.

[218] H. Ohshima, *Journal of Colloid and Interface Science*, 2002, **248**, 499–503.

[219] U. Marini Bettolo Marconi, M. Monteferrante and S. Melchionna, *Phys. Chem. Chem. Phys.*, 2014, **16**, 25473–25482.

[220] L. Vorwerg, M. Antonietti and K. Tauer, *Colloids and Surfaces A: Physicochemical and Engineering Aspects*, 1999, **150**, 129 – 135.

Erklärung

Hiermit erkläre ich, dass ich diese Arbeit selbstständig verfasst habe und keine anderen als die angegebenen Quellen und Hilfsmittel benutzt habe.

Stuttgart, 17.12.2014 Shervin Raafatnia